

Multiscale Design and Synthesis of Bioinspired Protein/Mineral Systems

A dissertation submitted by

Jin Guo

in partial fulfillment of the requirements for the degree of

Doctor of Philosophy

in

Chemical Engineering

Tufts University

February 2018

Adviser:

David L. Kaplan, Ph.D.

Abstract

Natural systems often outperform synthetic materials for their heterogeneous hierarchical architectures. These biological composites are usually comprised of soft and hard phases in complex pattern and structures, with dimension ranging from nanoscale to macroscale, although built in ambient environments from limited components. The resulting systems enable distinct integration of strength and toughness, leading to elegant structures with tissue-specific functions. For example, continuous macroscale gradients present at the osteochondral tissue interface with nano-/micro-scale patterns, reflect complex biological functions and involve changes in extracellular matrix (ECM) composition, cell types and mechanical properties.

To mimic these natural gradient hierarchical architectures, this dissertation provides bioinspired mineralization strategies to create novel protein/mineral composite systems via hierarchical assembly of nano-building blocks onto polymeric templates. Silk protein-based composites, coupled with selective peptides R5 with mineralization domains, were created to mimic the soft-to-hard transition in osteochondral interfaces. The gradient composites supported continuous transition in composition and structural and mechanical properties corresponding to the spatial concentration gradient of the mineralization domains. The biocompatible and biodegradable gradient silicified silk/R5 composites promoted and regulated osteogenic and chondrogenic differentiation of human mesenchymal stem cells in an osteoinductive and chondroinductive environment *in vitro*, respectively, in a manner consistent with the cellularity and ECM gradients at osteochondral interfaces.

In addition, natural composites are usually complex and anisotropic at the microscopic scale. Well-designed micropatterns present in native tissues and organs involve changes in

ECM compositions, cell types and mechanical properties to reflect complex biological functions. However, the design and fabrication of these micropatterns *in vitro* to meet task-specific biomedical applications remains a challenge. In this dissertation, I also present a *de novo* design strategy to code bio-functional micropatterns to engineer cell alignment through integration of aqueous-peptide inkjet printing and site-specific biomineralization. Inkjet printing allows for the direct writing of macroscopic R5 peptide patterns with microscale resolution on the surface of silk hydrogels. This is combined with *in situ* biomineralization of the R5 peptide for site-specific growth of silica nanoparticles on the micropatterns, while avoiding the use of harsh chemicals or complex processing. The resulting mineralized micropatterned systems were used to align human mesenchymal stem cells and bovine serum albumin *in vitro*.

In conclusion, this dissertation explored the feasibility of using silk as a template to combine selective mineralization domains to mimic the hierarchical architecture in biological systems from the molecular level to microscale and ultimately macroscale. The bioinspired multiscale design of mineral assembles on polymeric templates offers a useful approach to develop complex heterogeneous organic/inorganic composites for a wide range of applications in tissue engineering and regenerative medicine, especially osteochondral tissue engineering.

Acknowledgments

First and foremost, I would like to express my deep appreciation to my advisor, Prof. David Kaplan, for offering me the opportunity to engage in this lab and sharing his insights in biomaterials. I sincerely appreciate his encouragement on all my research ideas and constructive suggestions along my way. I highly cherish his guidance and advice that would always serve as inspiration for the personal and professional development in my life.

Additionally, I would like to thank my committee members, Prof. Gordana Vunjak-Novakovic, Prof. Ayse Asatekin and Prof. Qiaobing Xu. Specifically, Prof. Gordana Vunjak-Novakovic, for helping me to better understand osteochondral tissue engineering and her advice throughout my committee and TERC meetings. Prof. Ayse Asatekin, for keeping me rooted in chemical engineering fundamentals and all her efforts to accommodate my meeting schedules. Prof. Qiaobing Xu, for his guidance on my research, life and career development ever since I joined Tufts. I would also like to thank Prof. Fiorenzo Omenetto for his instruction and discussions on the inkjet printing work and for training me to think and write critically.

I would further like to thank my lab mentor Dr. Chunmei Li, who has always been there to provide guidance in labwork and research planning throughout my PhD life. I was so touched by the time she spent with me in cell culture labs and by her training me to think critically and independently. I would also like to thank Dr. Shengjie Ling, for his help in research and experimental design which may be the essential portions in PhD study. His input helped me avoid extra miles on the way, and discussion with him was always insightful and exciting. I would also like to thank Wenyi Li. Without her joining my research, the inkjet printing work won't be possible.

In addition, a thank you to all the fellow labmates in the Kaplan lab, Dr. Jeannine Coburn

Dr. Wenwen Huang, Dr. Siwei Zhao, Dr. Xiaoqin Wang, Dr. Ying Chen, Siran Wang, Dr. Whitney Stoppel, Dr. Benjamin Partlow, Dr. Wenda Zhou, Dr. Tom Dixon, Maria Rodriguez, Nicole Raia, Craig Hanna, Disha Sood, and my officemates in 200 Boston Ave. Your joyful company has made these years I spent in Tufts memorable for me.

Many thanks to my undergraduate students, Kathleen Coogan, Prakalya Chandrasekar, Javier Rincon, Anna Deck, Jenna Fromer. It is such a pleasure to be your mentor. Great appreciation to Milva Ricci, Laura Saurez, Carmen Preda, Martin Hunter, and Keleigh Sanford whose tireless behind the scenes effort kept my research going.

Last, but for most I want to thank my family and my in-laws. Thank you for being my support through the process and the cheerleader when I felt difficult to carry on. I would like to thank my husband, Jilei Liu who has been a constant source of encouragement and support during all the challenges of life and study. A thank you to my daughter, Grace Liu, for always bringing a big smile to my life. I love you all.

Thank you all and to anyone I missed!

Table of contents

1. Chapter 1: Introduction and background	1
1.1 Introduction.....	1
1.2 Purpose and organization	3
1.2.1 Goal.....	3
1.2.2 Research strategy	3
1.2.3 Overall approaches.....	4
1.2.4 Future directions	6
1.3 Background.....	8
1.3.1 Hierarchical architecture in natural systems	8
1.3.2 Biomineralization in natural organisms	12
2. Chapter 2. Gradient silk/silica composite system with tunable chemical, mechanical and structural properties.....	28
2.1 Abstract.....	28
2.2 Introduction.....	28
2.3 Materials and Methods.....	30
2.3.1 Materials	30
2.3.2 Preparation of aqueous silk solution	30
2.3.3 Preparation of the gradient silk/R5 hydrogels.....	31
2.3.4 Biosilicification.....	31
2.3.5 Fluorescence imaging of the FITC-labelled GSSR5 composites.....	32
2.3.6 Quantification of encapsulation efficiency	32
2.3.7 Quantification of silicification	33
2.3.8 Scanning Electron Microscopy (SEM) and Energy-dispersive X-ray Spectroscopy (EDS).....	33
2.3.9 Fourier Transform Infrared Spectroscopy (FTIR)	33
2.3.10 Mechanical tests.....	34
2.3.11 Characterization of hydration properties.....	34
2.3.12 Statistical analysis	35
2.4 Results and Discussion	35
2.4.1 The strategy of designing and synthesizing gradient protein/biosilica composites.....	35
2.4.2 Structural and mechanical properties of the GSSR5 composites.	39

2.5 Conclusions.....	48
3. Chapter 3. Directing <i>in vitro</i> cell differentiation towards osteochondral lineages in the gradient systems for osteochondral tissue engineering	49
3.1 Abstract.....	49
3.2 Introduction.....	49
3.3 Materials and Methods.....	50
3.3.1 hMSCs culture in gradient systems.....	50
3.3.3 Immunohistochemistry	51
3.3.4 Gene expression.....	52
3.3.5 Statistical analysis.....	52
3.4 Results and Discussion	52
3.4.1 Cytocompatibility evaluation of the GSSR5 composites.....	52
3.4.2 The GSSR5 composites offered tunable osteogenic differentiation and calcium deposition in 3D cell culture.....	54
3.4.3 The GSSR5 composites offered tunable chondrogenic differentiation and cartilage-like ECM deposition in 3D cell culture.....	59
3.4.4 Conclusions.....	64
4. Chapter 4. Coding cell micropatterns through peptide inkjet printing for arbitrary biomineralized architectures	66
4.1 Abstract.....	66
4.2 Introduction.....	66
4.3 Materials and Methods.....	69
4.3.1 Materials	69
4.3.2 Preparation of aqueous silk fibroin solution	70
4.3.3 Inkjet printing of the R5 peptide on the silk protein substrate	70
4.3.4 <i>In vitro</i> silicification.....	71
4.3.5 Morphology and structural characterization	71
4.3.6 Fluorescence microscopy of the fluorescent-labeled peptide micropatterns ...	72
4.3.7 hMSC cell culture	72
4.3.8 Microscopy and analysis.....	73
4.3.9 Protein alignment on the micropatterned hydrogels	73
4.3.10 Statistical analysis.....	73
4.4 Results and discussion	74
4.4.1 <i>De novo</i> design strategy to code mineral micropatterns	74
4.4.2 Fourier transform infrared (FTIR) mapping elucidated the structural details of the mineral micropatterns	78

4.4.3 Cell alignment on mineral micropatterns.....	80
4.4.4 Protein alignment on mineral micropatterns.....	83
4.5 Conclusion.....	84
5. Chapter 5. Overview and Future directions.....	87
5.1 Conclusions.....	87
5.2 Future directions and associated projects.....	87
5.2.1 Multiscale design and synthesis of biomimetic gradient protein/biosilica composites for osteochondral regeneration.....	87
5.2.2 Coding cell micropatterns through peptide inkjet printing for arbitrary biomineralized architectures.....	89
5.2.3 3D printing silk-based calcium phosphate scaffolds.....	90
References:.....	101

List of figures

Figure 1-1. Schematic representation of osteochondral interface tissue with illustration of gradient types [4]. Adapted by permission from Luca et al., 2015.	9
Figure 1-2. Various cell micropatterns in native tissues. (A) Alignment of endothelial cells and vascular smooth muscle cells in blood vessels; (B) Alignment of muscle cells in striated muscle tissues; (C) Alignment of Schwann cells in neurons [35]. Adapted from <i>Biotechnology Advances</i> , 32/2, Li et al., Engineering cell alignment in vitro, 347-365, Copyright (2014), with permission from Elsevier.	11
Figure 1-3. Examples of highly organized mineralized tissues in nature. (A, B) Complex silica nanopatterns in diatom. (C) Spicules of the deep-sea sponge exhibit well-organized silica architecture. (D) Periodic extinctions concentric to human compact bone osteon canal. (E) Biocalcification in sea shells [66]. Adapted by permission from Sumper et al., 2002; Sanchez et al., 2005.	13
Figure 1-4. Schematic representation of the spicule formation in sponge <i>S. domuncula</i> .16	
Figure 1-5. Schematic representation of the templating mechanism of the phase separation model (A-D) and SEM images of diatom <i>Cylindrotheca wailesii</i> valves at different stages (E-H). (A) monolayer of polyamine-containing droplets in close-packed arrangement within the SDV guides silica deposition. (B, C) Subsequent segregation into smaller (300 nm) droplets offers new spaces for silica deposition. (D) Final dispersion into 50 nm droplets. Silicification take place within the white areas (water phase). (E-H) SEM images of the development of diatom valves correspondingly. Adapted by permission from Sumper et al., 2002 [66].	18
Figure 1-6. Proposed mechanism for polycondensation of silicic acid mediated by R5 peptide [96]. Adapted by permission from Lechner et al., 2013.....	19
Figure 1-7. Hierarchical architecture of bone. Bone is composed of spongy bone in the interior and compact bone at the surface. Compact bone mainly consists of osteon and Haversian canals surrounded by blood vessels. Individual lamella which is comprised of patterned fibres oriented to form osteons with a lamellar structure. The fibres are composed of tropocollagen molecules and nanocrystals of hydroxyapatite linked by an organic phase [29]. Adapted by permission from Wegst et al., 2014.	20
Figure 1-8. Proposed 2-D schematic of silk heavy chain and light chain. The 3-D structure is most likely lamellar [124]. Adapted by permission from Ha et al., Copyright (2005) American Chemical Society.....	23
Figure 2-1. Biomimetic design of the GSSR5 composites. Silicatein mediates the formation of biosilica particles within the siliceous spicules which is organized by collagen in sponge (A). Biomimetic self-assembly of biosilica particles on the silk templates catalyzed by the biosilica selective peptide R5 (B). Schematic representation of the biomimetic GSSR5 composites and fluorescence microscopy image showing the gradient of FITC-labeled R5 peptide along the longitudinal direction of the composites (C). The high region contains a high content of the R5 peptide and biosilica particles in contrast to the transition to the medium and low regions where the contents diminish. Gross appearance of the GSSR5 composites (D). Molar ratio of R5/silk in the GSSR5 composites (E), showing gradually increasing concentration of the R5 peptide from the low to the high R5 peptide loading regions in the gradient composites. Scale bar, 2 mm.	37

Figure 2-2. SEM images of the GSSR5 composites with low (A, D), medium (B, E) and high (C, F) loadings of the R5 peptide, respectively. EDS spectra (the inserted images) of the GSSR5 composites with low (D), medium (E) and high (F) loading of the R5 peptide. Scale bars are 50 μm (top), 5 μm (bottom). SEM, scanning electron microscopy; EDS, energy-dispersive X-ray spectroscopy. The final GSSR5 composites exhibited uniform porous structure in three regions, while the pore sizes gradually decreased from the low region to the high region in the GSSR5 composites. The increasing distribution of biosilica particles was observed from low to high regions in the composites, which was further confirmed by EDS tests..... 40

Figure 2-3. Characterization of pore sizes in the gradient composites. (Significantly difference: *, $p < 0.05$; **, $p < 0.01$) 41

Figure 2-4. Characterization of silica density in the gradient composites. (*Significantly difference ($p < 0.05$)) 41

Figure 2-5. Extent of mineralization (measured as the molar percentage of silicon) in the GSSR5 composites with different loadings using silicon test colorimetric assay. Increased silicon content from the low to the high region in the GSSR5 composites demonstrated the gradient mineralization in the composites..... 42

Figure 2-6. (A) Optical image of the GSSR5 composites. (B) Fluorescence image of the FITC-GSSR5 composites. (C) Fluorescence intensity along the gradient trend of FITC-R5 in the GSSR5 composites. (D) Si distribution along the gradient composites generated by EDS mapping. Scale bar: 1 mm (A, B), 10 μm (D)..... 43

Figure 2-7. Representative stress-strain curves (A) and compressive moduli (B) of the low, medium and high regions in the GSSR5 composites. An approximately 6-fold increase in the compressive Young's modulus from low to high regions were achieved in the GSSR5 composites. (* $p < 0.01$, ** $p < 0.05$)..... 44

Figure 2-8. Representative Fourier self-deconvolution of amide I spectra for the silk/R5 composite before (A) and after (B) silicification. Percentage of the secondary structural elements in the composites (C). Key: open circles, measured data; wide solid line, summation of Gaussian peaks; thin solid lines, individual amorphous Gaussian peaks. The assignment of amide I bands was taken from the literature [156,158]. The content of non-crystalline structures including random coil and α -helix simultaneously diminished after silicification (α -helix: from $12 \pm 2\%$ to $10 \pm 1\%$; random coil: from $22 \pm 2\%$ to $18 \pm 2\%$), while the percentage of β -sheet crystalline structure increased after silicification (from $36 \pm 3\%$ to $48 \pm 4\%$)..... 45

Figure 2-9. Characterization of swelling ratio in the gradient composites. 47

Figure 2-10. Characterization of water uptake percentage in the gradient composites. ... 47

Figure 3-1. Fluorescence staining of actin (green) and nuclei (blue) of hMSCs in the GSSR5 composites in growth medium at day 19 (A). hMSCs spread out actin filaments, aligned with the pores and evenly distributed in the GSSR5 composites after 19-day culture. Live/dead staining of hMSCs cultured in the GSSR5 composites in growth medium at day 3 (B), day 11 (C) and day 19 (D). Strong green fluorescence with minimal visible red fluorescence demonstrated the cytocompatibility of the material. Alamar blue assay (E) showed the proliferation of hMSCs in the gradient (square), uniform (circle) and unsilicified plain silk control (triangular) composites over a 19-day period ($n > 3$). Uniform silicified silk/R5 composites had a silk/R5 molar ratio of 1/125. Unsilicified

plain silk composites served as controls. Scale bar, 200 μm . (*Significantly different from day 3 ($p < 0.01$)) 53

Figure 3-2. Histological sections taken from the unsilicified plain silk controls (A, E, I), and the GSSR5 composites with low (B, F, J), medium (C, G, K) and high (D, H, L) loadings of the R5 peptide after 6-week culture of hMSCs in osteogenic medium. H&E staining (A, B, C, D), von Kossa staining (E, F, G, H) and Sirius red staining (I, J, K, L). Schematic representation of cell differentiation along the GSSR5 composites (M). Scale bar, 50 μm (A-D); 200 μm (E-L). Unsilicified plain silk composites served as controls. Arrows indicate calcification; asterisks indicate composites. O, osteoblast-like cells; C, collagen-like bundles; F, fibroblast-like cells. 55

Figure 3-3. Characterization of the area ratio of calcium staining by von Kossa in the gradient composites. (**Significantly difference ($p < 0.01$)) 56

Figure 3-4. Immunostaining of collagen type I taken from the unsilicified plain silk controls (A), and the GSSR5 composites with low (B), medium (C) and high (D) loadings of the R5 peptide after 6-week culture of hMSCs in osteogenic medium. Scale bar, 50 μm 56

Figure 3-5. Transcript levels from hMSCs cultured in the GSSR5 composites under osteogenic conditions after 6 weeks. Expression of Runx2 (A), collagen type I (B), alkaline phosphatase (ALP, C) and bone sialoprotein (BSP, D). Data are shown relative to the expression of the respective genes in hMSCs cultured in unsilicified plain silk controls. Uniform silicified silk/R5 composites had a silk to R5 molar ratio of 1 to 125. The solid grey line represents the average of control and standard deviation is represented by dashed grey line. (*Significantly different from unsilicified silk controls ($p < 0.05$)) 58

Figure 3-6. Alcian blued (A-D) and collagen type II (E-H) staining of histological sections taken from the GSSR5 composites with control (A, E), low (B, F), medium (C, G) and high (D, H) loadings of the R5 peptide after 4-week culture of hMSCs in chondrogenic medium. The formation of the proteoglycan-rich matrix in the gradient composites indicated that these composites supported the formation of cartilaginous-like tissue. Scale bar, 50 μm 59

Figure 4-1. Design strategy and processing diagram of coding micropatterns. (a) *De novo* design to create silica bio-micropatterns on protein substrates by *in situ* mineralization of silica-binding peptides and inkjet printing. (b) Silk fibroin hydrogelation mechanism. (c) Biom mineralization of biosilica particles catalyzed by the biosilica selective peptide R5.. 74

Figure 4-2. Arrays of biosynthesized silica micropatterns on the hydrogel substrates. (a) Visual image shows freshly printed peptide logo with 1.2 cm width on the transparent silk hydrogel. (b) Fluorescence images of FITC-labeled R5 patterns on the silk hydrogels. (c) Visual image shows mineralized peptide logo with 1.2 cm width on the transparent silk hydrogel. (d) The whole free-standing protein system can be easily removed from the container used for gelation. (e) Schematic representation (left) and SEM images (right) show the linear array of mineralized micropatterns printed with different gap spacing between lines on the silk hydrogels. (f) AFM topography image of the silica particles on the mineralized micropatterns scanned over a 2 $\mu\text{m} \times 2 \mu\text{m}$ area. (g) The corresponding graph of the nanoparticle diameter distribution appears a sharp Gaussian distribution with a center value of $\sim 100 \text{ nm}$, in a range of 50-200 nm. (h, i) SEM images show the spatial resolution of the gap spacing between two lines decreased to 20 μm and the linewidth reached 1 μm 76

Figure 4-3. EDS map of Si and corresponding SEM image (inserted) confirmed the presence of Si on biosilica micropatterns. Scale bar, 5 μm 77

Figure 4-4. FTIR mapping showed the structural details of the biosilica micropatterns on the silk hydrogels. (a) Microscopic image of a $1032 \times 397 \mu\text{m}$ rectangle micropattern. (b) The contour map with the red/green and blue represent the strong and weak absorption of silica nanoparticles. (c) The single pixel spectra extracted from the white dashed line range in FTIR images. Compared to the blue spectra from the blue region of the silk substrate, the red/green spectra from the red/green region of silica micropattern present significant weaker absorption in amide I and II bands. (d) The red/green spectra dominate a sharp peak at 1647 cm^{-1} , which contributed to the random coil and/or helix structure. (e) The blue spectra show the strongest absorption at 1624 cm^{-1} and a shoulder at 1695 cm^{-1} , which were assigned to β -sheets and β -turns, respectively. FTIR, Fourier transform infrared spectroscopy. 79

Figure 4-5. hMSC alignment on the biosilica micropatterned and control hydrogels. (a, b, c) hMSCs aligned to the biosilica micropatterns on the silk hydrogels; (d, e, f) hMSCs on the unpatterned control silk hydrogels demonstrated typical morphology. Confocal micrographs of hMSCs on the silk hydrogels stained for F-actin (green, a, d), counterstained for nuclei and silk (blue, b, e) and overlay images (c, f). (g) Fluorescence images of hMSCs stained for F-actin (green) on the micropatterned “Tufts” logo. (h) Partial enlargement of Figure (g). (i) Zoomed view (left) and SEM (right) of hMSCs on the biosilica micropatterns. (j) Graphical representation of cellular alignment quantified via ImageJ software and an OrientationJ plug-in. (k) Coherency coefficients indicating cellular distribution on the micropatterned and control hydrogels. Scale bars, a-f, $200 \mu\text{m}$; g, 2 mm ; h, $700 \mu\text{m}$; i, $50 \mu\text{m}$ (left), $10 \mu\text{m}$ (right). 81

Figure 5-1. (A) Schematic of 3D printing silk-calcium phosphate scaffolds. (B) Photograph of 3D printer. (C, D) Photographs of 3D printing process of silk-mineral ink. (E, F, G, H) Photographs of 3D printed silk-calcium phosphate scaffolds with different pore sizes and patterns. Scale bar: 1 cm 94

Figure 5-2. Schematic representation of ink formation and extrusion. 95

Figure 5-3. Phase diagram of ink formulation with respect to silk, calcium phosphate and water. 96

Figure 5-4. SEM images of printed silk/mineral filaments intersecting between filament layers. 97

Figure 5-5. Optical images of the silk/calcium phosphate scaffold before and after sintering. 97

Figure 5-6. SEM images of silk/mineral scaffold (a, c) before sintering and (b, d) after sintering. (c, d), higher magnification view of the silk/mineral filament surface. Scale bars: a, b, $100 \mu\text{m}$; c, d, $4 \mu\text{m}$ 98

Figure 5-7. Wet spinning of silk/mineral filaments. (a) Optical image of silk/mineral fibers prepared by wet spinning in methanol bath. (b) Optical image of the fibers after sintering at $1000 \text{ }^\circ\text{C}$ in air. 99

1. Chapter 1: Introduction and background

1.1 Introduction

Natural biological systems are usually composed of soft and hard phases integrated in complex hierarchical architectures with dimension ranging from nanoscale to macroscale, although built at ambient temperature from limited components [1,2]. The resulting materials often obtain distinct integration of strength and toughness, leading to elegant and complex structure with tissue specific functions. For example, continuous macroscale gradients present at osteochondral tissue interfaces, reflect complex tissue functions and involve changes in extracellular matrix compositions, cell types and mechanical properties. Osteochondral interface presents a combination of structural, mechanical, compositional and cellularity gradients. The integration of these gradients ultimately lead to smooth transition [3,4] between two mechanically mismatched tissues, facilitating load transmission as well as reducing or eliminating delamination at the junctions [2,4–6].

To mimic these natural gradient hierarchical architectures, a variety of biphasic [7–11], multiphasic [12–15], and gradient [4,16–18] composites have been developed. However, unlike natural mineralization using non-collagenous components to regulate mineral formation on collagenous matrix [19], most strategies directly blended inorganic phase with substrate polymers [9,12,15,20–22], usually resulting in weakened structural uniformity and mechanical performance [23,24]. To address these problems, several *in vitro* biomineralization approaches have been reported [6,25] where deposition of hydroxyapatite was directly regulated on self-assembled collagen templates [25]. However, these strategies lack non-collagenous proteins as mediators to control mineralization on the polymer templates. Thus hierarchical materials were difficult to achieve in order to mimic

the complex architecture of natural tissues [26]. Moreover, the use of caustic chemicals during scaffold preparation limits the incorporation of bioactive molecules during material fabrication [6]. Thus, new and versatile biomaterial strategies are needed to create suitable biomimetic engineered grafts for interfacial tissue engineering [27].

In addition, natural composites are usually complex and anisotropic at microscopic scale. Micropatterns are widely found in native tissues and organs including diatoms, plant cell walls, arthropod exoskeletons and bones [28,29]. These micropatterns facilitate mechanical performance of tissues and organs, and also support biological functions, including structural support, defense and prey capture, yet formed from limited components (e.g., proteins, polysaccharides, minerals) [28,30–35]. For example, the spatial oriented micropatterns of collagen are found as parallel fiber bundles in tendons, concentric waves in bone and oriented fibrils in cartilage, which always contribute to mechanical properties and support cellular functions to these tissues and organs [36–38].

A variety of biomineralization strategies have been applied to mimic the components, structure and function of natural micropatterned tissues, including photolithography, microcontact printing and laser patterning, among others [31,35,39–42]. In particular, silica-based micropatterns play a critical role in many biomedical fields, including tissue engineering, drug delivery, cell transplantation, optics and *in vitro* tissue models, due to the biocompatibility, versatility and osteoinductive properties of silica [39,42–45]. However, most silica patterns were created in harsh conditions through complex processing. Moreover, such silica patterns exhibit weak substrate bonding to rigid substrates, thus can be damaged easily due to the inherent brittleness of silica [42]. These limitations reduce the broader utility of these composites due to costs or material weak points, and certainly limit direct processing and integration with biological components such as cell or bioactive therapeutics. Thus, novel design and fabrication of micropatterns *in vitro* are needed to

recreate the hierarchical architecture at microscale in nature to meet task-specific biomedical applications.

1.2 Purpose and organization

1.2.1 Goal

The goal of this dissertation is to explore the feasibility of using silk as a template to combine selective mineralization domains to mimic the hierarchical architecture in biological systems from the molecular level to microscale and ultimately macroscale. It is hypothesized that through bioinspired mineralization design to control the assembly of nano-building blocks on macroscale polymeric templates, these functional protein/mineral composite systems will achieve multiscale hierarchical architectures with tunable structural, compositional and mechanical properties for applications in tissue engineering, especially osteochondral tissue engineering.

1.2.2 Research strategy

The research strategy is composed of three steps: first, *developing a three-dimensional (3D) gradient composite system with tunable control over compositional, mechanical and structural properties that captures the soft to hard transition at osteochondral interfaces (Aim 1)*; second, *directing localized cellular differentiation towards osteochondral lineages in vitro, in consistency with the cellular and ECM gradients in osteochondral interfaces (Aim 2)*; third, *coding cell micropattern and alignment through in situ biomineralization of peptide micropatterns on protein substrates to achieve arbitrary mineral architectures that can meet task-specific biomedical applications (Aim 3)*.

It is hypothesized that the gradient hydrogel systems coupled with spatial concentration variation of silica-selective peptides R5 will achieve versatile and controllable transitions of mineralization domains in biomaterial substrates, and ultimately achieve tunable

chemical, structural and mechanical properties. The biomimetic environments provided by the composite systems will direct human mesenchymal stem cells (hMSCs) towards osteochondral lineages in a manner consistent with the trends in osteochondral tissues. In addition, we hypothesize that macroscopic mineralized peptide patterns with microscale resolution can be used to align cells and protein on silk protein substrates *in vitro*.

1.2.3 Overall approaches

Silk-based biomimetic hydrogel composites were enzymatically crosslinked with silica-selective peptides R5. The compositional, mechanical and structural properties of the protein/mineral composites were modulated through concentration gradients of R5 peptides. Gradient hydrogel systems were used to guide human mesenchymal stem cells (hMSCs) to form cellularity gradients that mimic the intrinsic features of osteochondral interfaces. Inkjet printing of macroscopic R5 peptide patterns with microscale resolution on silk hydrogels followed by site-specific mineralization will lead to well-designed mineralized micropattern systems for cell and protein alignment.

Aim 1: development of silk-based gradient composites

The **goal** is to achieve silk-based gradient composites with tunable chemical, mechanical and structural properties that capture the soft to hard transition in osteochondral interfaces (Chapter 2). The research approaches are composed of three steps: 1) introducing spatial variation of silica-selective peptide R5 to silk protein substrates via enzymatic crosslinking; 2) regulating mineralization extent and mechanical properties through varying concentration gradients of the R5 peptide in the silk hydrogels; 3) achieving gradient structural architecture with interconnected pore networks to facilitate cell infiltration and osteo-/chondral- genesis. The hydrogel system coupled with spatial concentration gradients of the R5 peptide will achieve versatile and tunable gradients of mineralization

domains in protein substrates, and ultimately provide tunable chemical, structural and mechanical properties. These findings should offer promise in elucidating structure-function relationships that govern cell behaviors in Aim 2 and ultimately improving the safety and efficacy of clinically translatable biomaterial systems.

Aim 2: assessment of *in vitro* cell differentiation

The **goal** was to direct *in vitro* stem cell differentiation towards osteogenic and chondrogenic lineage within the gradient system in consistency with the cellularity gradients and pericellular environments in osteochondral interfaces (Chapter 3). The research approaches are composed of three steps: 1) investigating cell proliferation and cytocompatibility of the gradient composites; 2) achieving tunable osteogenic and chondrogenic differentiation of hMSCs in the gradient systems *in vitro*, in a manner consistent with the trends in osteochondral interfaces; 3) demonstrating the formation and distribution of pericellular bone-like/cartilage-like ECM in the gradient system consistent with the trends in osteochondral interfaces. The chemical, mechanical and structural properties of the 3D composites will interact with cellular behaviors and generate a cellularity gradient in cell distribution, morphology, and pericellular ECM deposition *in vitro*. These findings will give us unique insights into the progression of osteochondral interfacial tissue development. Investigation of bone-like and cartilage-like tissue development with molecular, morphological, and structural end-point assays will provide feedbacks for material design (Aim 1), and guide tissue development *in vivo* ultimately.

Aim 3: development of micropatterned system

The **goal** was to provide a design strategy to code and synthesize functional micropatterns to engineer cell alignment through peptide inkjet printing for arbitrary biomineralized architectures (Chapter 4). The research approaches are composed of three steps: 1) inkjet

printing of arbitrary peptide micropatterns on silk hydrogel substrates; 2) introducing site-specific mineralization on peptide micropatterns and assessing the spatial resolution of the mineralized micropatterns; 3) investigating cell and protein alignment on the mineralized micropatterns in vitro. The combination of peptide inkjet printing and site-specific biomineralization will result in well-organized mineralized micropatterns, with control over the organization of human mesenchymal stem cells (hMSCs) and BSA on the silk hydrogels *in vitro*.

1.2.4 Future directions

Multiscale design and synthesis of biomimetic gradient protein/biosilica composites for osteochondral tissue regeneration

The *goal* is to engineer gradient protein/biosilica grafts that mimic the intricate features of osteochondral tissues and have capacity to enhance osteochondral regeneration *in vivo*. We propose to: develop silk composites with the desirable features: structural (gradient porosity), mechanical (controllable silk polymorphism and mineralization degree) and compositional (tunable silk and mineral contents) (Aim 1); investigate the effects of gradient systems on osteochondral coculture in vitro (Aim 2); evaluate the survival and function of the engineered gradient grafts in animal models for osteochondral reconstruction (Aim 3). It is **hypothesized** that the gradient composite system will direct cells to form highly specialized osteochondral interface tissues with capacity for survival and function in a rat model.

Coding cell micropatterns through peptide inkjet printing for arbitrary biomineralized architectures

The *goal* is to code and synthesize multifunctional biomineralized micropatterns with capacity to engineer the alignment of various cells types and functionality in different

tissues including nerve tissues *in vivo*. We propose to: encapsulate a library of bioactive molecules and substances (e.g., nerve growth factor (NGF)) in the silica particles to allow for sustained release of functional biofactors from arbitrary silica micropatterns (Aim 1); direct neural cell growth on functionalized silica micropatterns for neuron growth (Aim 2); investigate the efficiency of axonal alignment on flexible and implantable protein substrates in order to efficiently repair the injured sites of the nervous systems (Aim 3). It is **hypothesized** that the functional biominerlized micropatterns comprised of various factors will have broadened applications in tissue engineering and regenerative medicine including nerve tissue regeneration.

3D printing silk-based calcium phosphate scaffolds

The **goal** is to design a simple, green and versatile process to directly write the assembly of silk protein and calcium phosphate nanoparticles and build up biomimetic ceramic-hard tissue parts for bone and osteochondral tissue engineering. We **propose** to: 3D print silk-calcium phosphate scaffolds with gradient structure and interconnecting porous network (Aim 1); incorporate functional biomolecules and substances in this system to screen for optimal doses and combinations in 3D environment and create patient-customized tissue engineered grafts (Aim 2); evaluate the cytocompatibility and osteoconductivity of 3D printed scaffolds in vitro for treatments of osteochondral defects and osteonecrosis (Aim 3). The biocompatible 3D printed silk-based scaffold can be used to promote vascularization and osteogenesis as a potential therapy for osteochondral defects and osteonecrosis.

1.3 Background

1.3.1 Hierarchical architecture in natural systems

1.3.1.1 Gradients in osteochondral interface

Impact on public health. With a rapidly aging population and increasing obesity rates, osteoarthritis represents a worldwide common degenerative disease, often leading to severe pain and functional loss of articular joints. Due to the avascular nature of these tissues, adult human cartilage has a limited regenerative capacity. Novel therapies for cartilage and subchondral degeneration are urgently needed. Current clinical treatments for osteochondral defects such as autografts and prosthetic implants have achieved limited success due to donor site morbidity, insufficient tissue availability and the risk of infections [46]. Tissue engineering approaches offer to revolutionize the way we currently treat osteochondral defects, enabling full repair and restoration of the structure, composition and function of osteochondral interface tissue.

Osteochondral interface design. An attractive feature of natural tissue interfaces is their unique gradient structure[1,47]. Osteochondral interfaces, for example, consist of spatial variation in composition, architecture and mechanics from subchondral bone to cartilage [4,48,49]. Bone mineral hydroxyapatite (HA) gradually diminishes from subchondral bone to calcified cartilage and completely disappears in hyaline cartilage, which contributes to a continuous change of mechanics along the trend [50]. The structural gradients consist of spatial variation in ECM composition and orientation from subchondral bone to cartilage [4,48,49]. Subchondral bone mainly is comprised of osteoblasts, osteoclasts and osteocytes, while chondrocytes is the major cell type in cartilage region [51].

The natural osteochondral interface enables the smooth transition from hard bone to viscoelastic articular cartilage covering the joint surface [51]. Continuous gradient

osteocondral interface connects mechanically mismatched tissues, facilitates the transmission of complex mechanical loads and minimizes stress concentration at the junctions [52–54].

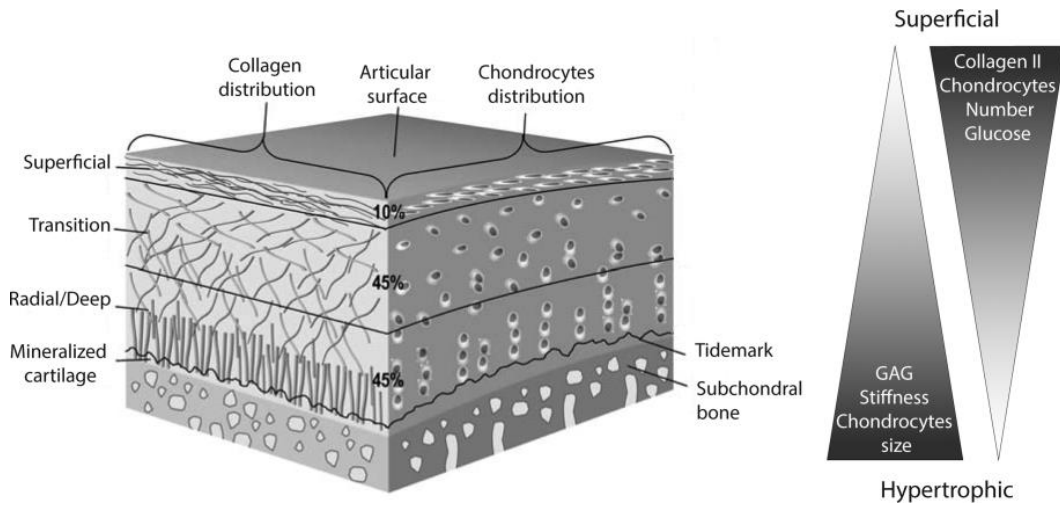


Figure 1-1. Schematic representation of osteochondral interface tissue with illustration of gradient types. Adapted by permission from Luca et al., 2015 [4].

These gradients of minerals and ECM lead to a continuous change of mechanics along the trend [3,4], and also play an important role in connecting mechanically mismatched tissues, facilitating load transmission as well as reducing or eliminating delamination at the junctions [4–6,47]. The repair and regeneration of osteochondral interface tissue present a significant challenge in terms of representing the compositional and structural gradients with varying mechanical properties to eliminate the stress concentration [55].

State of the art. In recent years, a variety of biomaterial designs have been proposed to generate biphasic[7–9,12,18], triphasic [11,14], and multilayered scaffolds [12,13,37,56,57] to mimic the natural osteochondral interface tissue or features [4]. Upon discovering the continuous gradient transition from subchondral bone to articular cartilage, gradient-based

biomaterials presenting continuous variation of physical[12,18], biochemical signals[58] and growth factor concentration[16,59] resembled the native tissue more closely. Thus these systems have provided promising strategies for the regeneration of osteochondral tissues *in vitro* and *in vivo* [2,4]. Detamore's group have proposed and tested an effective method to generate microsphere-based gradient scaffolds incorporated with multiple different biological signals in a scaffold to mimic the gradient behavior of the osteochondral tissue.[2,17]

However, each design strategy holds limitations, such as failing to match the biocompatibility and degradability of natural tissues, while also being resilient and elastic, and allowing for incorporation of bioactive substances during the biological remodeling process. More importantly, the persistent incidence of delamination between different layers in composite materials present as a significant reduction in utility for the treatments of osteochondral injuries *in vivo* and thus needs to be further addressed to reduce the biomechanical instability.[7,9] Therefore, new designs are needed to recreate the continuous gradation of the suite of features, such as structural, mechanical, physicochemical, and biological that occur at osteochondral interfaces.

1.3.1.2 Micropattern in human tissues and organs

Cell micropatterns exert significant effects in regulating cell behaviors via reorganizing cytoskeleton, relocating membrane proteins, control nucleus gene expression, remodeling ECM etc. Cell alignment to patterns plays a key role in tissue regeneration and contribute to mechanical properties of tissues such as tendon, cardiac muscle and skeleton. *In vitro* engineering of cell alignment offers applications in biomechanics, cell biology, tissue engineering and regenerative medicine. A variety of engineering approaches have been developed to regulate cell alignment *in vitro*, such as mechanical loading, topographical patterning, and surface chemical treatment [35].

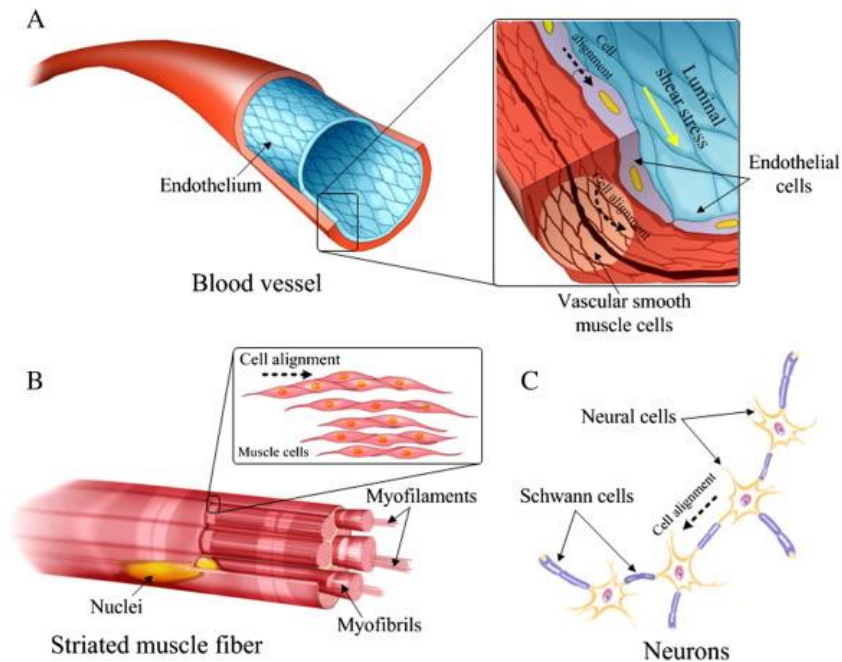


Figure 1-2. Various cell micropatterns in native tissues. (A) Alignment of endothelial cells and vascular smooth muscle cells in blood vessels; (B) Alignment of muscle cells in striated muscle tissues; (C) Alignment of Schwann cells in neurons. Adapted from *Biotechnology Advances*, 32/2, Li et al., *Engineering cell alignment in vitro*, 347-365, Copyright (2014), with permission from Elsevier [35].

Blood vessels are circumferentially arranged in fibrous helix within vascular media, collagen fibers, stacked between bands of elastin, and discontinuous sheets of endothelial basement membrane, leading to a unique structural organization with both resilience and tensile properties [6] (**Figure 1-2**). Striated muscles actively generate sufficient contractile forces for various body movements, such as heart beating, muscle stretching and contraction. At cell level, this is attributed to the matured rod-like shaped muscle cells consisting of highly organized intracellular myofilaments (e.g., actin-filaments, myosin filaments) (**Figure 1-2B**) [60,61]. Cell alignment also exists in nerve tissues. In axonal

regeneration, neural cells spontaneously orient parallel to aligned Schwann cells (SCs) in injured peripheral and central nerve *in vivo* (**Figure 1-2C**) [62–64].

State of the art. A variety of biomineralization strategies have been developed to mimic the components, structure and function of natural micropatterned tissues, including photolithography, microcontact printing and laser patterning, among others [31,35,39–41]. The resultant micropatterns provide promising applications in regenerative medicine, microelectronics, drug screening, and optical and biomedical sensors [35,42]. In particular, silica-based micropatterns play a critical role in many biomedical fields, including tissue engineering, controlled drug delivery, cell transplantation, optics, electronics as well as *in vitro* tissue models, due to the biocompatibility, versatility and osteoinductive properties of silica [39,42–45]. However, most of these silica patterns are created in harsh conditions, such as extremely high temperature and/or pressures, strongly acidic solutions, or complicated and energy-intensive processing techniques. Moreover, the silica patterns generated by these methods usually exhibit weak substrate bonding to rigid substrates, thus can be damaged easily due to the inherent brittleness of silica [42]. These features reduce the broader utility of these systems due to costs or material weak points, and certainly limit direct processing and integration with biological components such as cell or bioactive therapeutics.

1.3.2 Biomineralization in natural organisms

Natural mineralized composites provide morphogenetic and biological blueprints for novel biomaterial designs. Diatoms, which are known for its highly ordered periodic hexagonal. construct silica micro-/nano- patterns with precise control through bottom-up growth under physiological and ambient conditions [65]. The plywood-like micropatterns in arthropod exoskeletons enhances toughness thousands of times greater than the pristine minerals, and

iridescence derived from these features (known as structural color) provides adaptive biological functions such as mating, signaling and camouflage[28,32–34]. (**Figure 1-3**)

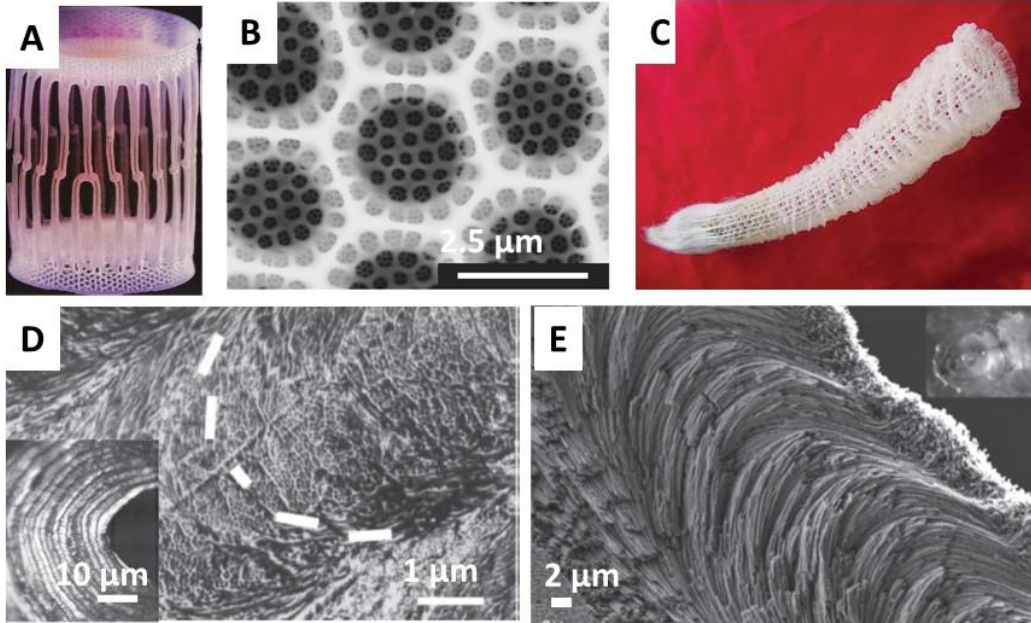


Figure 1-3. Examples of highly organized mineralized tissues in nature. (A, B) Complex silica nanopatterns in diatom. (C) Spicules of the deep-sea sponge exhibit well-organized silica architecture. (D) Periodic extinctions concentric to human compact bone osteon canal. (E) Biocalcification in sea shells. Adapted by permission from Sumper et al., 2002; Sanchez et al., 2005 [66].

When designing materials for biomedical applications, three factors are critical: chemical composition, nano/microstructure and architecture. **Table 1-1** summarized the major inorganic components in biological systems. Silicon, for example, is an essential trace element that makes up 0.440 ± 0.446 % of bone in human, improves bone strength and stimulates collagen synthesis [67,68]. Biosilica is osteoinductive and can bind to calcium crystals [69–73]. However, crystalline silica materials alone are hard and brittle, which

makes them less favorable unless formed into composites, as in native bone (silica, hydroxyapatite and collagen) to improve toughness.

Table 1-1. Major inorganic solids in biological systems [74]

Mineral	Formula example	Organisms
Calcium carbonate	CaCO_3	Molluscs/Algae/exoskeletons/plants/fish
Calcium phosphate	$\text{Ca}_{10}(\text{PO}_4)_6(\text{OH})_2$	Vertebrate/bone/teeth/mussels
Calcium oxalate	$\text{CaC}_2\text{O}_4 \cdot \text{H}_2\text{O}$	plants
Silicon dioxide	$\text{SiO}_2 \cdot n\text{H}_2\text{O}$	Exoskeletons/algae
Iron oxide	Fe_3O_4	Bacteria/teeth

A variety of substitute calcium formula are also formed in natural systems.

1.3.2.1 Mechanism of biomineralization

Natural materials are hybrid composites of ceramic building blocks (i.e., calcium salts and silica) arranged by polymeric frameworks (i.e., proteins and polysaccharides) [75–79]. For example, seashells, bone and teeth are highly mineralized hybrid materials that provide protection in nature [80]. Biomineralization provides insights to fabricate functional materials through construction of architectures from molecular to macroscopic scales. The basic constructional processes of biomineralization involves the following steps [74,81].

1) Supramolecular pre-organization: The beginning step involves construction and organization of reaction environments before the initiation of mineralization. The preorganization of supramolecules adopts two approaches during the intra- and inter-molecular mineralization: self-assembly of protein cages and lipid vesicles during intracellular biomineralization; facilitated construction of extended protein-polysaccharide networks during extracellular biomineralization [82].

2) Interfacial molecular recognition (templating): The second step is associated with controlled nucleation of inorganic phase from aqueous solution. The pre-organized supramolecular constructions provide a network for the assembly and growth of mineral nuclei. The functionalized surfaces of these frameworks serve as templates to guide the nucleation of the inorganics. The assembly of inorganic clusters is usually controlled by three complementarities: electrostatic, structure and stereochemical complementarities at the interface of organic templates and inorganic components [83,84].

3) Cellular processing: The last step in fabrication of biological minerals involves multi constructional cellular activity at larger scale. Without the control of cellular intervention, mineral clusters continue to grow within the confinement of organic frameworks, resulting in biomineral particles with constrained size, crystallographic structure and morphologies [85]. More strikingly, biomineral assemblies in natural materials often acquire elaborate ultra-/micro-scale structures with delicate texture and architectures. The cellular processing of mineral particles is often accompanied with a compromise between constrained crystallization and genetic control of morphology.

1.3.2.2 Biosilicification in sponge

Biological mineralization is a process by which natural organisms deposit minerals in an organized manner on the organic templates, leading to functional materials with desired

hierarchical structures [83,86]. Biosilica deposition in nature is controlled by silicatein and guided by collagen to form a highly organized pattern in sponges [87–89]. During the formation of siliceous spicules in sponges (also known as *in vivo* silicification, as sketched in **Figure 1-4A**), central protein filaments consisting of silicatein and scaffold protein first self-assemble in the extracellular space. Silicatein then triggers and mediates the deposition of biosilica particles on a fibrous network of collagen, which subsequently form concentric lamellar layers around the filament [90].

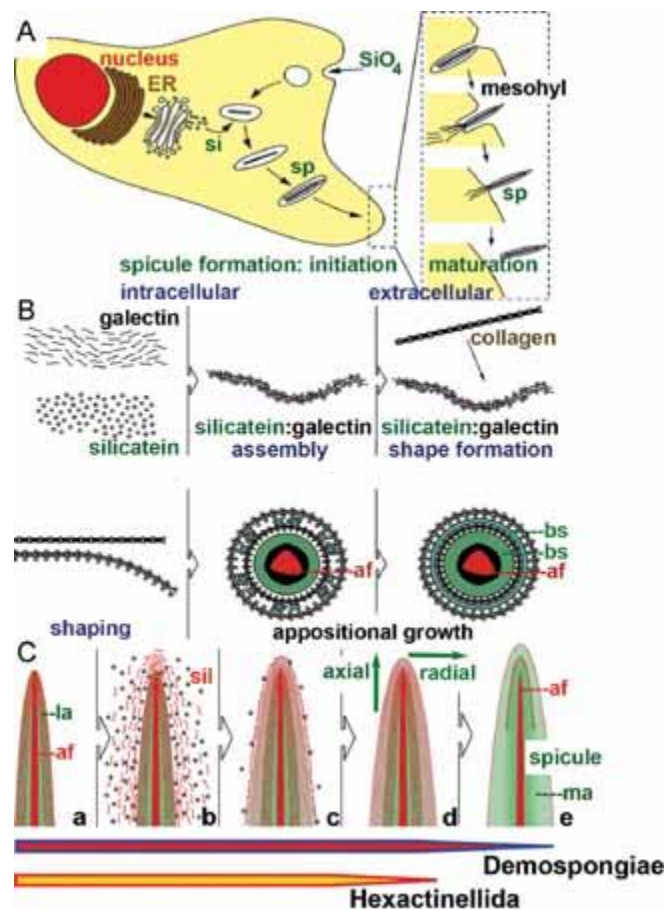


Figure 1-4. Schematic representation of the spicule formation in sponge *S. domuncula*.

a) the initial intracellular stage of spicule synthesis. b) appositional growth of the spicules extracellularly. c) maturation of spicules in the axial direction by appositional silica deposition. Adapted by permission from Wang et al., 2010 [91].

Spiculogenesis mainly consists of three stages:

- 1) Intracellular phase (initial growth): During the first step, silicatein is synthesized and transported into vesicles for the formation of axial filaments [92]. Silica formation takes place in two directions on the filaments: centrifugal and centripetal. Finally, spicules are released extracellularly for further growth.
- 2) Extracellular phase (appositional growth): Silicatein is arranged to larger clusters along strings and organized in parallel to the surface of the spicules. The silicatein molecules associate with galectin to allow for appositional growth of the spicules [93].
- 3) Extracellular phase (shaping): The organization of the galectin-silicatein complexes is mediated by collagen fibers to form a net-like structure. While collagen provides the organized framework for the morphogenesis of the spicules, the silicatein/galectin strings induce the deposition of silica particles during growth of the axial filaments.

1.3.2.3 Biosilicification in diatom.

Organisms such as diatoms, which are known for their complex and intricate silica architectures, construct silica micro-/nano- patterns with precise control through bottom-up growth under physiological and ambient conditions without additional chemical treatments or post-processing steps. A phase separation model reveals the molecular mechanism that controls the nanofabrication process. During wall biogenesis, repeated phase separation events take place to produce similar silica nanopatterns in smaller scales [66].

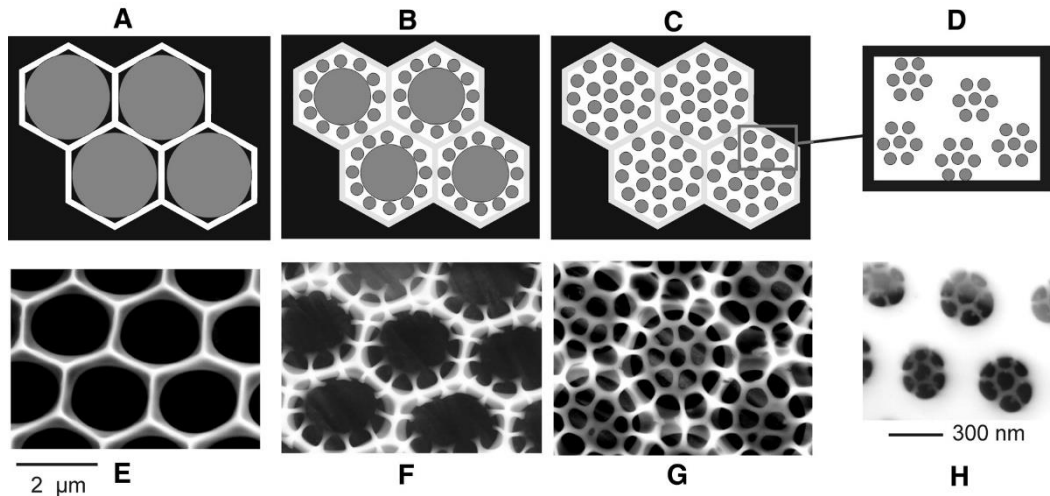


Figure 1-5. Schematic representation of the templating mechanism of the phase separation model (A-D) and SEM images of diatom *Cylindrotheca wailesii* valves at different stages (E-H). (A) monolayer of polyamine-containing droplets in close-packed arrangement within the SDV guides silica deposition. (B, C) Subsequent segregation into smaller (300 nm) droplets offers new spaces for silica deposition. (D) Final dispersion into 50 nm droplets. Silicification take place within the white areas (water phase). (E-H) SEM images of the development of diatom valves correspondingly. Adapted by permission from Sumper et al., 2002 [66].

At molecular level, biosilica morphogenesis in the diatom cell wall consists of a matrix of organic macromolecules, i.e., native silaffin-1A (natSil-1A) protein for silica formation and native silaffin-2 (natSil-2) protein for biosilica template organization. During *in vivo* silicification, natSil-1A triggers and mediates the formation of the silica particles, while natSil-2 moderates the activities of natSil-1A to form organized patterns through molecular self-assembly and phase-separation processes [65,94].

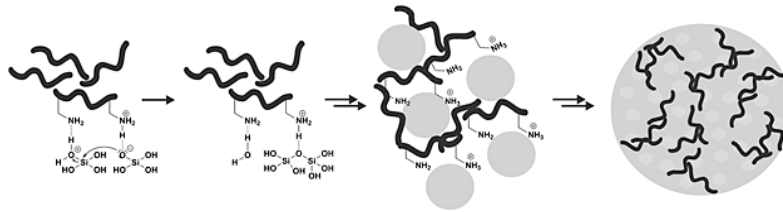


Figure 1-6. Proposed mechanism for polycondensation of silicic acid mediated by R5 peptide. Adapted by permission from Lechner et al., 2013 [96].

The R5 peptide (H-SSKKSGSYSGSKGSKRRIL-OH), as a repeating peptide sequence in silaffin protein of the diatom *Cylindrotheca fusiformis*, involves silica precipitation *in vitro* from a phosphate buffered solution of silicic acid at neutral pH and room temperature [87–89,95]. During precipitation of silica particles by the R5 peptide, positive charged lysine residues on the peptide mediate formation of siloxane bonds, followed by self-assembly of these peptides [88,96].

1.3.2.4 Biocalcification in bone

Natural bone has a highly hierarchical structure with organized mineralized collagen fibrils [97]. Bone mainly consists of three components: inorganic materials (65–70%, hydroxyapatite, HA) for hardness, organic mass (20–25%, collagen type I, osteonectin and osteoclastin) as basic building blocks, and water (10%) associated with collagen [98–100].

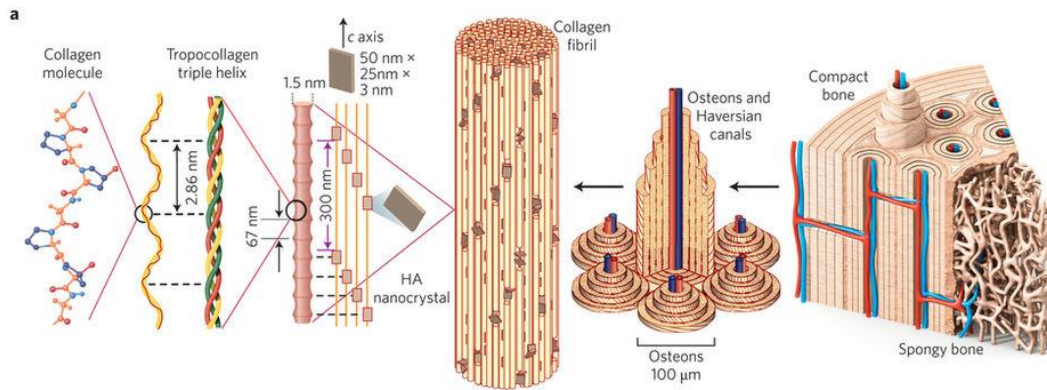


Figure 1-7. Hierarchical architecture of bone. Bone is composed of spongy bone in the interior and compact bone at the surface. Compact bone mainly consists of osteon and Haversian canals surrounded by blood vessels. Individual lamella which is comprised of patterned fibres oriented to form osteons with a lamellar structure. The fibres are composed of tropocollagen molecules and nanocrystals of hydroxyapatite linked by an organic phase. Adapted by permission from Wegst et al., 2014 [29].

In bone, macroscale arrangements involve both compact/cortical bone at the outside area and spongy/trabecular bone (foam-like material with $\sim 100 \mu\text{m}$ thickness) in the interior. Compact bone is composed of osteons and Haversian canals, which surround blood vessels. Osteons have a lamellar structure, with individual lamella consisting of fibres arranged in geometrical patterns. The fibres are comprised of several mineralized collagen fibrils, with tropocollagen formed from three chains of amino acids and nanocrystals of hydroxyapatite, and linked by an organic phase to form fibril arrays (**Figure 1-7**).

Mineralization of bone involves two types of proteins, collagen type I and a family of non-collagenous proteins. Collagen type I serves as templates for apatite nucleation [101], while non-collagenous proteins such as osteonectin and osteocalcin act as nanoprecursors to stabilize amorphous calcium phosphate phases [102,103], and initiate of nucleation and

hierarchical assembly of apatite within the collagen framework [104]. Specifically, osteopontin and bone sialoprotein are responsible for the initiation of bone mineralization. Bone sialoprotein act as a crystal nucleator, while osteopontin is related to the formation of crystals. Osteocalcin and osteonectin, as found in fully mineralized matrix, mainly contribute to regulating the size and speed of crystallization. During bone resorption, osteocalcin act as a chemoattractant for osteoclast, while osteopontin and bone sialoprotein assist the association to osteoclasts [105]. Stupp et al. proposed a bottom-up approach where peptide amphiphiles self-assembled to direct mineralization of HA. The crystallographic c axes of HA were aligned with the long axes of the fibers, which is similar to the alignment of hydroxyapatite crystals on collagen fibrils in bone [106,107].

1.3.2.5 Biocalcification in sea shells

Biocalcification by silk-like proteins in sea shells. Mollusca shell mainly consist of 95-99 wt% calcium carbonate CaCO_3 boned with 1-5% organic supramolecules. Silk-like protein were isolated from these shells (i.e., *Pinctada fucata*), which obtained an antiparallel β -pleated sheet secondary structure with polypeptide chains of large amounts of glycine and alanine[108]. The mineralized shell structure resulted from the combination of silk-like and solution proteins, where silk-like protein establish the self-assembled sheet-like architecture, while soluble proteins direct the nucleation process [109,110]. When preadsored on the substrates of β -chitin and silk fibroin, macromolecules extracted from the aragonitic or calcitic shell layers in mollusks induced aragonite or calcite formation *in vitro*, suggesting that these macromolecules played a key role in the deposition of aragonite or calcite *in vivo* [111].

1.3.2.6 Bioinspired material synthesis through biomimetic mineralization

To mimic these natural gradient structures, a variety of biomimetic material designs [112] have been developed. For example, R5 peptide has been either genetically [73,113] or

chemically [114] fused to the silk protein to control the assembly and deposition of silica particles in 2D silk films for osteogenesis. The combination of silk and silica upregulated bone sialoprotein (BSP) and collagen type I osteogenic markers, and promoted mineral depositions [72,81].

1.3.2.7 Silk

Silks are spun by a number of different insects including silkworms, spiders, bees and caddisflies among other arthropods [115]. Spider silk are stronger than silkworms, however, their cannibalistics in nature prevent their large scaling. Cocoons from *Bombyx mori* silkworm, which the primary commercial source of silk fibers, contains two proteins, fibroin and sericin. Fibroin provides strength while sericin act as glue to maintain the shape of cocoons. Owing to its excellent mechanical and optical properties, biocompatibility, biodegradability and implant ability, silk fibroin (hereafter referred to as silk) is finding various applications in tissue engineering, biomedical therapeutics, photonics, electronics [116,117].

1.3.2.8 Silk structure

The silk fibroin mainly consists of a heavy chain (H) with 5263 amino acids (Mw ~390 kDa) and a light chain (L) with 266 amino acids (Mw ~26 kDa) [118]. The fibroin is a semi-crystalline protein with highly repetitive pattern of amino acid sequences [119], rich in hydrophobic β -sheet-forming domains (94% of the chain length) linked by small hydrophilic amorphous segments [120]. The crystalline domain is comprised of 12 ordered Gly-X repeats, where “X” represents alanine in 65%, serine in 23% and tyrosine in 9%, self-assemble into anti-parallel β -sheets. In comparison, the hydrophilic subdomains consist of 11 hydrophilic linkers between the crystalline domains and are rich in glycine, alanine, serine and tyrosine [118,121,122]. The result β -sheet-forming regimes within the

fibroin structure self assembles to form strong and resilient materials [123]. From here on, silk fibroin is referred to as silk throughout the rest of the review unless otherwise specified.

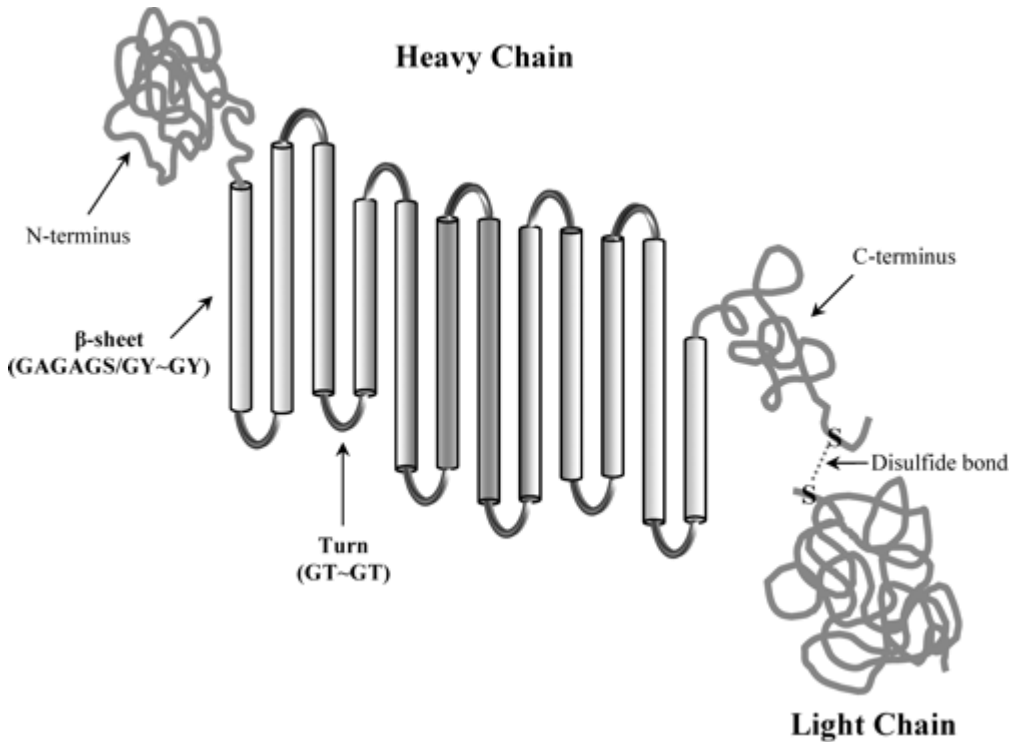


Figure 1-8. Proposed 2-D schematic of silk heavy chain and light chain. The 3-D structure is most likely lamellar [124]. Adapted by permission from Ha et al., Copyright (2005) American Chemical Society.

While the structure and function of crystalline domains are widely reported, the role of amorphous domain and their interaction with the crystalline segments are still poorly understood. The crystalline domains are punctuated tyrosine rich motifs, where the serine residues are substituted by tyrosine residues and eleven irregular linker regions [124]. Simulations and NMR studies of native fibroin suggested that the tyrosine residues in *B. mori* silk fibroin have multiple functions, including enhancing the solubility, destabilizing

the local semi-crystalline regions during the intermolecular chain arrangement [126]. One study on poly(AG) model peptides also suggested that the phenolic side chains may be susceptible to π - π interactions as shown in **Figure 1-9** [125].

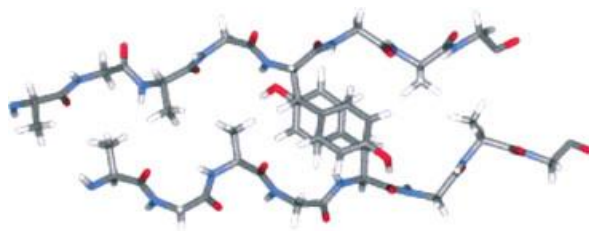


Figure 1-9. Illustration of the local environment surrounding two Tyr residues in poly(AG) model peptides, calculated by MM from an initial silk II structure. The two Tyr are able to interact with one another by aromatic π -stacking, if the peptides are in-register. Adapted by permission from Asakura et al., 2004 [125].

1.3.2.9 The role of silk in biomineralization

Nature provides blueprints to assembly structure to synthesis novel functional inorganic-organic hybrid systems. With the unique recognition (amino acid residue) and self-assembly properties site, silk from different sources can assist the synthesis of novel inorganic-organic composites for various applications including biomedical applications, optics, electronics etc.

Nanocomposites from bioengineered spider silk-silica fusion proteins

Spider silk protein has strong mechanical properties with self-assembled fibrous structures. Foo et al. combined the features of biosilica with silk through creating a family of chimeric proteins of domains from the major ampullate spidroin 1 (MaSp1) protein of *Nephila clavipes* spider dragline silk and the R5 peptide from the silaffin protein of diatom

Cylindrotheca fusiformis [127]. The MaSp1 protein can self-assemble into films and fibers through different post-processing procedures and thus provide control over the structure and morphology of the composites. The R5 peptide plays a role in catalyzing and regulating silica deposition under mild reaction conditions. The resulting mineralized composites showed silica distribution of 0.5-2 μm in diameter. Furthermore, through regulating processing methods, different morphology and structure of the composites were achieved to produce mineralized fibers and films [128–130].

To further understand the interaction between organic and inorganic components in the hybrid system, three major domains of the chimeric proteins were systematically investigated to study their effects on protein folding and mineralization: 1) a core silk domain for material self-assembly, 2) a mineralization domain for silicification, and 3) a histidine tag for purification [131]. Computational modeling revealed that the presence of silica and histidine domains increased the accessible surface area to positive charged amino acids in solvents and reduced the formation of β -sheet structure, thus resulting in higher degree of silicification. Besides, the location of the silica domains has minimal effect on the β -sheet formation and exposure to the silicon ions in the solvents. Furthermore, processing conditions including reaction agents, types of crystallization induction and temperature impact the secondary structure of the chimeric proteins and thus silicification. Combination of modeling and experimental approached allows for identification of the key factors in materials design and thus can provide control over the function of the bioengineered functional materials [132–134].

The bioengineered spider-silica composite systems demonstrated osteoinductivity *in vitro* with potential applications in bone tissue engineering [127,128,135,136]. The presence of silica particles on the silk films promoted hMSCs proliferation, upregulate their osteogenic markers and facilitated apatite formation. Furthermore, biodegradable silica particles in the

hybrid systems lead to control over the degradation/remodeling rates of the organic/inorganic composites [72,137].

Chemically-synthesized silk-silica fusion proteins

Silica binding peptide were chemically coupled into silk substrates to form silk-silica chimera composites. The tyrosine groups on natural *Bombyx mori* silk were modified by diazonium coupling and EDC/NHS activation of all acid groups in preparation for chemical conjugating the silica binding peptide to the silk templates [138]. Upon silicification under mild conditions, silica spheres formed on the biomolecule templates of the chimeric silk-silica composites. Higher degree of silicification was observed on chemical chimeras, probably owing to the higher amount of silica binding sites after surface modification as compared to genetic chimeras. Conjugation variables include peptide sequence, silk source and synthesis approach can be varied to control the silica formation on the composites.

In summary, these silk/R5/biosilica composites showed osteoinductive properties in the form of two-dimensional (2D) films, with biocompatibility and low inflammatory response [139–141]. In these systems, the R5 peptide has been either genetically [127] or chemically fused [138] to the silk to control the assembly and deposition of the silica particles for osteogenesis. However, several limitations still exist, as 2D systems fail to mimic the complex cellular environments *in vivo* [142]. Moreover, constructs with uniform physical and chemical properties lack the spatially and structurally defined hierarchical architecture that exists in native tissues and fail to recreate the natural graded interface [143].

Silk-hydroxyapatite nanocomposites

Silk was also used as templates to direct the deposition of nano-HA particles [144–146]. The morphology and crystallization of nano-HA can be tuned through variation of silk

content during biomineralization process. Nevertheless, these composite materials showed limitations in mimicking the complex cellular environments in three dimensions to present more representative response to the biological/physical stimuli in the surroundings.

In this dissertation, inspired by biomineralization strategies, silk-based mineral composites coupled with silica selective peptide with mineralization domains were created to achieve tunable structural, mechanical and chemical properties to mimic hierarchical architectures that occur in natural systems.

2. Chapter 2. Gradient silk/silica composite system with tunable chemical, mechanical and structural properties

2.1 Abstract

Continuous gradients present at tissue interfaces such as osteochondral systems, reflect complex tissue functions and involve changes in extracellular matrix compositions, cell types and mechanical properties. New and versatile biomaterial strategies are needed to create suitable biomimetic engineered grafts for interfacial tissue engineering. Silk protein-based composites, coupled with selective peptides with mineralization domains, were utilized to mimic the soft-to-hard transition in the osteochondral interface. The gradient composites supported tunable mineralization and mechanical properties corresponding to the spatial concentration gradient of the mineralization domains (R5 peptide). The composite system exhibited continuous transitions in terms of composition, structure and mechanical properties.

2.2 Introduction

An attractive feature of natural tissue interfaces is their unique gradient structure [1,2]. Osteochondral interfaces, for example, consist of spatial variation in the extracellular matrix (ECM) composition and orientation from subchondral bone to cartilage [4,48,49]. Hydroxyapatite (HA) also gradually diminishes from subchondral bone to calcified cartilage and completely disappears in hyaline cartilage [51]. These gradients of minerals and ECM lead to a continuous change of mechanics along the trend [3,4], and also play an important role in connecting mechanically mismatched tissues, facilitating load transmission as well as reducing or eliminating delamination at the junctions [2,4–6].

To mimic these natural gradient structures, a variety of biphasic [7–11], multiphasic [12–15], and gradient [4,16–18] composites have been developed. However, unlike natural

mineralization during which non-collagenous proteins initiate and regulate mineral formation on the collagenous matrix [19], most of these materials were prepared through mixing inorganic bioactive phase (e.g., chemosynthetic HA crystallites) with additional substrate materials (e.g., collagen) [9,12,15,20–22]. These approaches generally result in weakened structural uniformity and mechanical performance of the resultant composite materials [23,24]. To address these problems, several *in vitro* biomineralization approaches have been reported [6,25] where the nucleation and growth of inorganic mineral phase was regulated directly on well-organized polymer templates. For instance, a three-layer scaffold composed of HA nanocrystals nucleating on self-assembled collagen fibers was developed to support cartilage and bone formation [25]. The gradient mineralization was achieved via changing the ratio of HA/collagen in different layers. However, HA crystallization on self-assembled collagen fibers lacks non-collagenous proteins as mediators of the mineralization process, thus well-controlled mineral deposition on the polymer template is difficult to achieve for the synthesis of advanced materials that mimics the complicated hierarchical natural tissues [26]. Moreover, the use of caustic chemicals during scaffold preparation limits the incorporation of bioactive molecules during material fabrication [6]. Therefore, new strategies are needed to design and synthesize continuous gradient materials using biomimetic mineralization [27].

In this work, inspired by the growth of natural sponge spicules, we designed a novel route to fabricate gradient protein/biosilica composites via site-specific *in vitro* biomineralization. The biosilica selective peptide-R5, a bioinspired analog derived from the silaffin peptides that are used for silica synthesis in *Cylindrotheca fusiformis* [88], was introduced into the silk fibroin (thereafter referred to silk) hydrogel composites through enzymatic crosslinking. A well-controlled gradient distribution of the R5 peptide was achieved by regulating the peptide concentration along the longitudinal direction of the

composites. The final gradient silicified silk/R5 (GSSR5) composites presented a structure with varied pore sizes and a gradient distribution of biosilica particles, similar to the structural features of the natural osteochondral interface. More remarkably, these continuous gradient structures endowed the composites with gradient mechanical properties. In addition, unlike chemical synthetic methods which use caustic chemicals [147–150], this simple and versatile approach allows for surface modification of biosilica particles to encapsulate biomolecules and drugs [151]. This novel gradient biomaterial design offers a useful approach to meet a broad range of needs in regenerative medicine involving osteochondral tissue engineering.

2.3 Materials and Methods

2.3.1 Materials

All chemical reagents used for making the GSSR5 composites were purchased from Sigma-Aldrich (St. Louis, MO, USA) unless otherwise specified. All materials and reagents used for cell culture and analysis were purchased from Thermo Fisher Scientific (Waltham, MA, USA) unless otherwise specified.

2.3.2 Preparation of aqueous silk solution

Silk solutions were prepared using our previously established procedures [152]. Briefly, ten grams of silk cocoons were cut into pieces and boiled in 4 L of 0.02 M sodium carbonate solution for 30 minutes to remove the coating of sericin protein. Degummed fibers were rinsed with deionized water three times and dried in air overnight. Five grams of dried fibers were dissolved in 20 ml of 9.3 M lithium bromide solution at 60°C for 4 hours. The silk fibroin solution was then dialyzed against deionized water using a dialysis cassette (Pierce 3.5 kDa MWCO; Fisher Scientific, PA) for 2 days. The solubilized silk solution was then centrifuged twice at 9,000 RPM, 4°C for 20 min to remove insoluble particulates.

Protein concentration was determined by drying a known mass of the silk solution at 60°C for 12 hours and measuring the mass of the remaining solid.

2.3.3 Preparation of the gradient silk/R5 hydrogels

The biosilica selective peptide R5 (H-SSKKSGSYSGSKGSKRRIL-OH) with a purity of 95% was synthesized by GenScript (Piscataway, NJ, USA). Lyophilized horseradish peroxidase (HRP, type VI) powder and the R5 peptide powder were dissolved in deionized water to form a stock solution of 1,000 U/mL and 0.7 mg/μL, respectively. To generate the gradient silk/R5 hydrogels with high, medium and low loadings of the R5 peptide (thereafter referred to high, medium and low regions, respectively), the R5 peptide solution was first mixed with the silk solution in a R5/silk molar ratio of 250/1, 125/1 and 62.5/1, respectively. The mixture was then loaded sequentially into a cylindrical container layer by layer. First, the high region was loaded and gelation were initiated by adding the HRP and hydrogen peroxide (H₂O₂, 165 mM) solution at a ratio of 40 units and 40 μL per 1 mL of silk solution, respectively. Before the complete gelation in high region, the medium region was added on top of the high region followed by the addition of HRP and H₂O₂ with the same concentration as in the high region. Then the low region was added on top of the previous medium region followed by the addition of HRP and H₂O₂. The mixture was then incubated at 37°C overnight to ensure complete gelation. Unsilicified plain silk control hydrogels were prepared by crosslinking silk solution using HRP and H₂O₂ with the same ratio as in the gradient silk/R5 hydrogels.

2.3.4 Biosilicification

Biosilica deposition was introduced into the gradient silk/R5 hydrogels post gelation. Pre-hydrolyzed tetraethoxysilane (TEOS) solution was prepared by mixing 2.23 ml of TEOS solution with 7.76 ml of 50% ethanol/water solution, 10 μl of 1 M hydrogen chloride (HCl)

and left at room temperature for 15 min. A 50 μ l aliquot of the silk/R5 hydrogel was immersed in 200 μ l silicifying medium consisting of 40 μ l prehydrolyzed TEOS solution and 160 μ l buffer solution (10.4 μ l 1M bis-tris propane, 5.6 μ l 1M citric acid solution and 144 μ l deionized water) to allow for silicification at room temperature overnight. The silicifying medium was changed twice every 4 hours during the silicification process.

2.3.5 Fluorescence imaging of the FITC-labelled GSSR5 composites

The fluorescein isothiocyanate (FITC)-labelled R5 peptide (FITC-SSKKSGSYSGSKGSKRRIL-OH, GenScript, NJ, USA) was added into the R5 peptide solution in a molar ratio of 1 to 4,000. The resultant peptide mixture was used to create the FITC-labelled GSSR5 composites following the same gelation and silicification process as described earlier. The FITC-labelled composites were imaged using with the Olympus mvx10 macroscope and captured by cellSens Dimension (ver 1.8.1) program (Olympus, Tokyo, Japan).

2.3.6 Quantification of encapsulation efficiency

Quantification using FITC-labeled R5 peptide was performed to determine the encapsulation efficiencies of the R5 peptide in the GSSR5 composites. The FITC-R5 peptide was added into the R5 peptide solution in a molar ratio of 1 to 4,000 following the preparation process as described earlier. The silicifying medium was collected after silicification of the silk/R5 hydrogels. The amount of the FITC-R5 peptide in the supernatants was quantified by recording the emission signal using a SpectraMax M2e multimode microplate reader (Molecular Devices, CA, USA). All conjugation reactions were repeated in triplicate. The reaction efficiency was calculated as follows:

Encapsulation efficiency

$$= \frac{\text{Peptide amount added} - \text{Peptide amount in supernatant}}{\text{Peptide amount added}} \times 100\%$$

2.3.7 Quantification of silicification

The amount of silica in the composite materials was determined using the silicon test colorimetric assay kit (Merck, NJ, USA) according to the manufacturer's instructions [153–155]. The GSSR5 composites were evenly cut to three sections along the longitude direction of the sample, as referred to the low, medium and high regions. The sections were then washed three times with ethanol to remove unreacted TEOS and hydrolyzed with 1 M NaOH overnight. The samples were diluted to quantify the released silicic acid.

2.3.8 Scanning Electron Microscopy (SEM) and Energy-dispersive X-ray Spectroscopy (EDS)

The gradient silicified silk/R5 hydrogel composites were frozen at -20°C and lyophilized. The samples were then quenched in liquid nitrogen, sputter coated with gold and imaged with a Carl Zeiss Ultra 55 field emission scanning electron microscope (Carl Zeiss SMT, Germany). Measurements of silica particle size were characterized by SEM. Energy dispersive X-ray analysis was used to determine the local composition of the samples (spectra of Si) over a depth of a few micrometers at different regions of the samples.

2.3.9 Fourier Transform Infrared Spectroscopy (FTIR)

Infrared spectroscopy of the lyophilized silicified silk/R5 hydrogel composites was performed with a Jasco FT/IR-6200 Spectrometer (Jasco, OK, USA), equipped with a deuterated triglycine sulfate detector (Pike Technologies, WI, USA). Unsilicified and silicified silk/R5 hydrogels with a silk/R5 molar ratio of 1/62.5 were prepared based on process described earlier and then frozen at -20°C and freeze dried for FTIR analysis. Each measurement incorporated 32 scans from 600 to 4000 cm^{-1} to yield spectra with a nominal resolution of 4 cm^{-1} . Fourier self-deconvolution (FSD) of the infrared spectra covering the Amide I region was performed with Opus 5.0 software (Bruker Optics Corp., MA, USA),

as described previously [156,157]. The deconvoluted amide I bands were fitted with Gaussian peaks, and the ratio of the peak area of each secondary structure component to the total amide I band area were used to determine the fraction of each secondary structural element in the composites. Absorption bands in the range from 1590 to 1610 cm^{-1} relate to the side chain of amide I; bands from 1610 to 1637 cm^{-1} and from 1697 to 1703 cm^{-1} correlate to β -sheet structure; bands in the range from 1638 to 1652 cm^{-1} represent random coil, bands ranging from 1652 to 1660 cm^{-1} were ascribed to α -helices, and peaks in the range from 1660 to 1696 cm^{-1} were assigned to β -turn structures [156,158].

2.3.10 Mechanical tests

Unconfined compression tests were performed on the gradient silicified silk/R5 hydrogels between two impermeable plates using an Instron 3366 machine (Instron, MA, USA). The GSSR5 hydrogels were evenly cut to three sections along the longitude direction of the composites and tested separately as the low, medium and high regions of the hydrogels. The samples were subjected to a compressive ramp up to 15% strain at a strain rate 0.001 strain/s to obtain the stress-strain curves [159]. The 15% strain chosen here is within the physiological range for articular cartilage [3]. Compressive modulus was calculated as the slope of the curve from 5% to 10% strain. Five independent cylindrical samples (5 mm in height and 4 mm in diameter) were tested for each condition.

2.3.11 Characterization of hydration properties

The lyophilized GSSR5 composites were evenly cut to three sections along the longitude direction of the composites and tested separately as the low, medium and high regions. Samples were immersed in distilled water at room temperature for 24 h followed by removal of excess water. The wet weight of the hydrated sample (W_h) were determined individually. Samples were then dried in an oven at 60°C for 24 h and the dry weight of

samples (W_d) was determined. The swelling ratios and the water uptake percentage were calculated as follows [160]:

$$\text{Swelling ratio} = \frac{W_h - W_d}{W_d}$$

$$\text{Water uptake (\%)} = \frac{W_h - W_d}{W_h} \times 100$$

2.3.12 Statistical analysis

Paired or unpaired Student t-tests, as appropriate, were used to determine statistical differences between groups. One-way ANOVA was used when comparing features between groups. In all cases, $n > 3$ were used for data sets ($p < 0.05$ or 0.01). GraphPad software (GraphPad Prism software, CA) was utilized.

2.4 Results and Discussion

2.4.1 The strategy of designing and synthesizing gradient protein/biosilica composites.

Biomimetic mineralization is a process by which natural organisms deposit minerals in an organized manner on the organic templates, leading to functional materials with desired hierarchical structures [83,86]. During the formation of siliceous spicules in sponges (also well-known as *in vivo* silicification, as sketched in **Figure 2-1A**), central protein filaments consisting of silicatein and scaffold protein first self-assemble in the extracellular space. Silicatein then triggers and mediates the deposition of biosilica particles on a fibrous network of collagen, which subsequently form concentric lamellar layers around the filament [90]. To mimic this natural biomineralization process, silk protein was chosen to construct the 3D continuous porous structure due to its biocompatibility, degradability and tunable mechanical properties [161]. The silk protein was enzymatically crosslinked via

HRP and H₂O₂ to form a hydrogel [161], acting as templates to mimic the function of collagen and other scaffold protein in nature [19,90]. The R5 peptides were simultaneously crosslinked into the silk templates to trigger and mediate the *in situ* biomineralization in the GSSR5 composites (**Figure 2-1B**). The spatial variation of silicification was achieved by varying the molar ratio of the R5/silk along the longitudinal direction of the composites (**Figure 2-1C**). The mixture of the high, medium and low regions of the GSSR5 composites were loaded sequentially into a cylindrical mold layer by layer, followed by the addition of HRP and H₂O₂ to initiate gelation. The gradient distribution of the mineralization domains allows for tunable control over the morphology, self-assembly and distribution of biosilica particles and ultimately regulation of the mechanical and structural properties and architecture of the gradient composites.

The final hydrogels appeared free-standing and uniform without any cracks (**Figure 2-1D**). Their gradient structures were confirmed by fluorescence imaging of the GSSR5 composites containing immobilized FITC-labeled R5 peptides and encapsulation efficiency measurements. The GSSR5 composites displayed an increasing fluorescence signal of FITC-R5 along the longitudinal direction of the composites (**Figure 2-1C**), indicating the increasing content of the R5 peptide along the trend. The fluorescence intensity along the gradient trend of the FITC-R5 in the GSSR5 composites were measured (**Figure 2-1C**), indicating the continuous gradient evidence in the composites. **Figure 2-1E** shows the quantification of the R5 peptide in different regions of the GSSR5 composites.

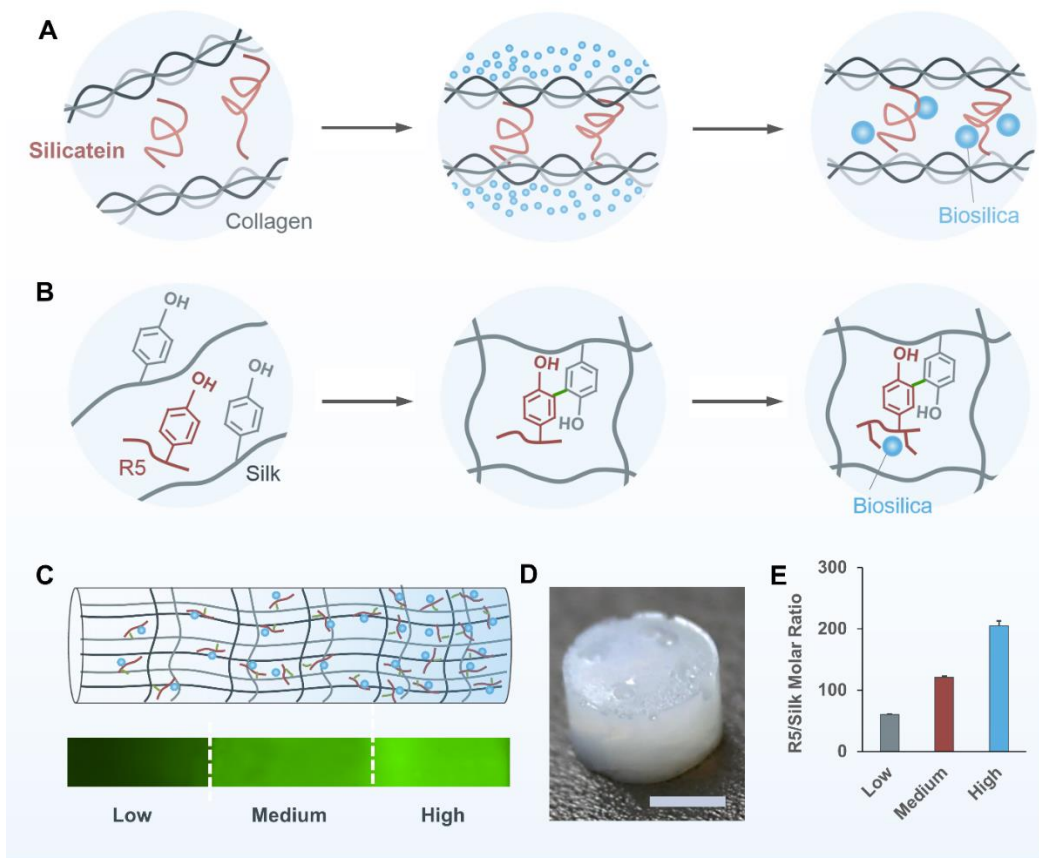


Figure 2-1. Biomimetic design of the GSSR5 composites. Silicatein mediates the formation of biosilica particles within the siliceous spicules which is organized by collagen in sponge (A). Biomimetic self-assembly of biosilica particles on the silk templates catalyzed by the biosilica selective peptide R5 (B). Schematic representation of the biomimetic GSSR5 composites and fluorescence microscopy image showing the gradient of FITC-labeled R5 peptide along the longitudinal direction of the composites (C). The high region contains a high content of the R5 peptide and biosilica particles in contrast to the transition to the medium and low regions where the contents diminish. Gross appearance of the GSSR5 composites (D). Molar ratio of R5/silk in the GSSR5 composites (E), showing gradually increasing concentration of the R5 peptide from the low to the high R5 peptide loading regions in the gradient composites. Scale bar, 2 mm.

The R5 peptide were loaded into the low, medium and high regions of the GSSR5 composites with a synthesis silk/R5 molar ratio of 1/62.5, 1/125 and 1/250, respectively, whereas the R5 peptide encapsulated in the low, medium and high regions of the composites after silicification had a final silk/R5 molar ratio of 1/60, 1/121, 1/205, respectively. The slight difference is because some weakly attached R5 peptides were released into the silicifying medium during *in vitro* silicification. According to the encapsulation efficiency assay, the percentage of the released peptides in the low, medium and high regions were 3.8±2.0%, 3.2±1.4% and 7.9±3.3%, respectively, while the encapsulation efficiencies of the low, medium and high regions in the GSSR5 composites were 96.2±2.0%, 96.8±1.4%, and 92.1±3.3%, respectively (**Table 2-1**).

Table 2-1. Quantification of the R5 peptide in the GSSR5 composites using FITC labeling technique.

R5 loading	Low	Medium	High
Silk/R5 synthesis ratio ^a	1/62.5	1/125	1/250
R5 released (%) ^b	3.8±2.0	3.2±1.4	7.9±3.3
Silk/R5 final ratio ^c	1/60	1/121	1/205
Encapsulation efficiency (%) ^d	96.2±2.0	96.8±1.4	92.1±3.3

^a Silk/R5 molar ratio in the GSSR5 composites, determined by the amount of silk and R5 loaded to the composites. ^bThe release of the R5 peptide through the process of silicification, determined by quantifying the amount of the FITC-R5 peptide released to the

silicifying media. ^c Silk/R5 molar ratio after silicification. ^dEncapsulation efficiencies of the GSSR5 composites

2.4.2 Structural and mechanical properties of the GSSR5 composites.

To examine the mesoscopic structures of the GSSR5 composites, SEM measurements were performed on the freeze-dried GSSR5 composites (**Figure 2-2 A-F**). Freeze-drying process was performed on the materials to create a favorable heterogeneous matrix of pore structure for cell culture. The final GSSR5 composites exhibited uniform porous structure in three regions, while with different pore sizes. The pore sizes gradually decreased from the low region to the high region in the GSSR5 composites. The pore sizes in the low regions were significantly larger than those in the medium regions ($p < 0.01$), which were larger than those in the high regions in the gradient composites (**Figure 2-3**, $p < 0.05$). In addition, the gradient distribution of biosilica particles was observed (**Figure 2-2 D-F**). Spherical silica particles (760 ± 130 nm in diameter, **Figure 2-2F**) were embedded in the silk/R5 network giving rise to a rough granular appearance superimposed on the bio-template network, indicating the silicification function of the R5 peptide was maintained upon grafting to the silk templates. More importantly, the amount of biosilica significantly increased by increasing of the loading of the R5 peptide, which was further confirmed by EDS tests (the insert images in **Figure 2-2 D-F**). The silica densities in the low regions were significantly lower than those in the medium regions, which were lower than those in the high regions in the gradient composites (**Figure 2-4**, $p < 0.05$). The molar percentage of silicon increased from low to high R5 peptide loading region, with values of 1.1%, 1.5% and 2.3% of low, medium and high regions, respectively, as determined by silicon test colorimetric assay (**Figure 2-5**). The Si distribution along the gradient composites were generated using EDS

mapping (**Figure 2-6**), which further confirmed the continuous gradient silicification in the composites.

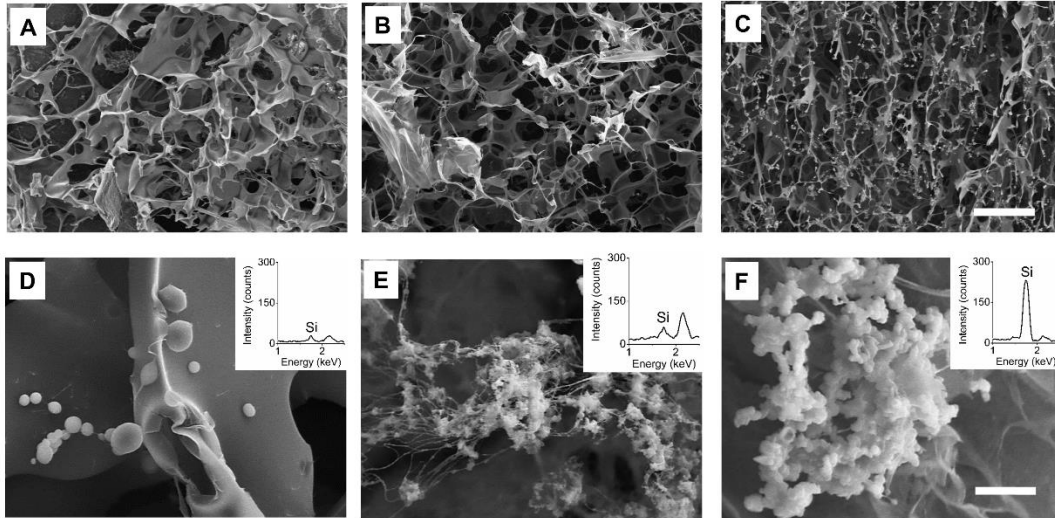


Figure 2-2. SEM images of the GSSR5 composites with low (A, D), medium (B, E) and high (C, F) loadings of the R5 peptide, respectively. EDS spectra (the inserted images) of the GSSR5 composites with low (D), medium (E) and high (F) loading of the R5 peptide. Scale bars are 50 μm (top), 5 μm (bottom). SEM, scanning electron microscopy; EDS, energy-dispersive X-ray spectroscopy. The final GSSR5 composites exhibited uniform porous structure in three regions, while the pore sizes gradually decreased from the low region to the high region in the GSSR5 composites. The increasing distribution of biosilica particles was observed from low to high regions in the composites, which was further confirmed by EDS tests.

The pores of the gradient composites appeared highly interconnected without clearly defined pore boundaries, the distance between adjacent lamellae appeared to be $\sim 50\text{--}150$ μm in SEM images (**Figure 2-3**).

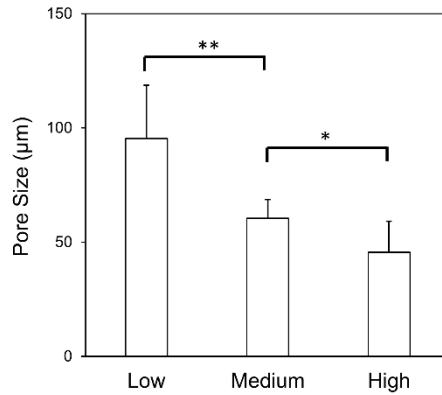


Figure 2-3. Characterization of pore sizes in the gradient composites. (Significantly difference: *, $p < 0.05$; **, $p < 0.01$)

The gradient distribution of biosilica particles has been quantified and statistically analyzed in **Figure 2-4**. The silica densities of low, medium and high regions in the gradient composites were significantly different from each other.

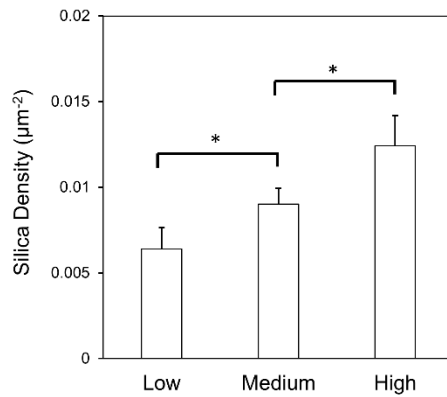


Figure 2-4. Characterization of silica density in the gradient composites. (*Significantly difference ($p < 0.05$))

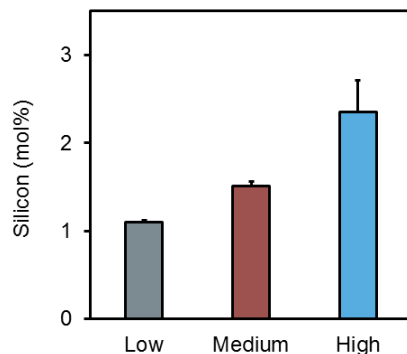


Figure 2-5. Extent of mineralization (measured as the molar percentage of silicon) in the GSSR5 composites with different loadings using silicon test colorimetric assay. Increased silicon content from the low to the high region in the GSSR5 composites demonstrated the gradient mineralization in the composites.

To demonstrate continuous gradients in the materials, fluorescence microscopy was performed to characterize the green fluorescence intensity of FITC-R5 along the increasing trend of R5 in the FITC-GSSR5 composites. In addition, the gradient distribution of Si was confirmed along the longitude direction of the composites by EDS mapping. The continuous gradient of the materials was evidenced by fluorescence intensity characterization of the FITC-labelled GSSR5 composites and EDS mapping of Si in the GSSR5 composites.

The fluorescence intensity along the gradient trend of the FITC-R5 in the GSSR5 composites were measured (**Figure 2-6**), indicating the continuous gradient evidence in the composites. The Si distribution along the gradient composites were generated using EDS mapping (**Figure 2-6**), which further confirmed the continuous gradient silicification in the composites.

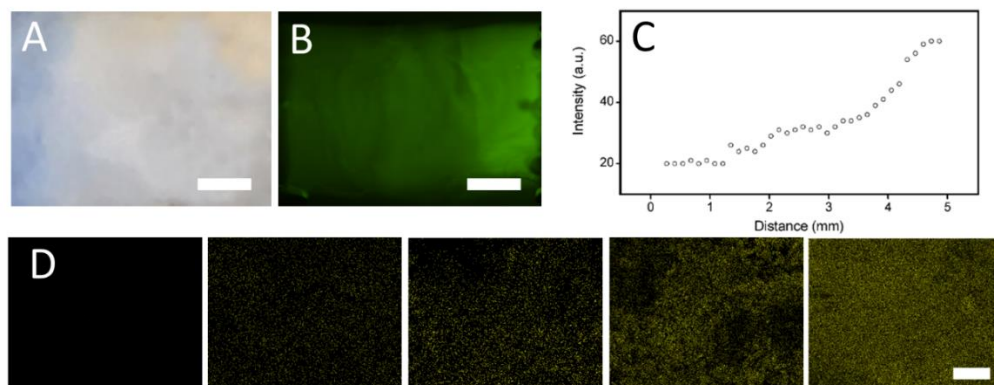


Figure 2-6. (A) Optical image of the GSSR5 composites. (B) Fluorescence image of the FITC-GSSR5 composites. (C) Fluorescence intensity along the gradient trend of FITC-R5 in the GSSR5 composites. (D) Si distribution along the gradient composites generated by EDS mapping. Scale bar: 1 mm (A, B), 10 μm (D).

Compression tests were carried out to assess the mechanical performance of the GSSR5 composites, as shown in **Figure 2-7**, the gradient biosilica content in the protein network endowed gradient mechanical behaviors. The GSSR5 composites with low, medium and high loadings of the R5 peptide were evenly sectioned into three regions along the longitude direction of the composites, whose representative stress-strain curves were shown in **Figure 2-7A**. The calculated compressive Young's moduli of the low, medium and high regions in the GSSR5 composites were 20.7 ± 5.0 kPa, 49.5 ± 10.6 kPa and 128.5 ± 16.4 kPa, respectively (**Figure 2-7B**). The results showed that a 2-fold increase of biosilica content from low to high regions led to an approximately 6-fold increase in the compressive Young's moduli, indicating that the stiffening effect of biosilica was achieved. The compressive modulus of the low region was significantly lower than that of the medium region ($p < 0.05$), which was again significantly lower than that of the high region in the GSSR5 composites ($p < 0.01$).

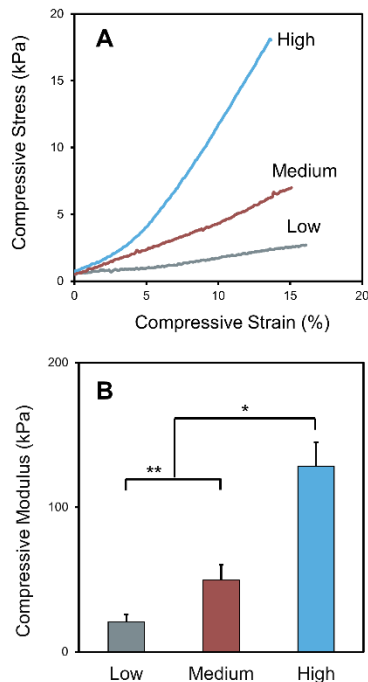


Figure 2-7. Representative stress-strain curves (A) and compressive moduli (B) of the low, medium and high regions in the GSSR5 composites. An approximately 6-fold increase in the compressive Young's modulus from low to high regions were achieved in the GSSR5 composites. (* $p < 0.01$, ** $p < 0.05$)

FTIR spectroscopy was used to investigate the secondary structure of the protein/biosilica composites. **Figure 2-8** shows the amide I bands in the FTIR spectra of the silk/R5 composites before (**Figure 2-8A**) and after (**Figure 2-8B**) silicification. The peaks at 1644 cm^{-1} , 1656 cm^{-1} and 1675 cm^{-1} indicate that the non-crystalline structures, such as random coil ($1638\text{-}1652\text{ cm}^{-1}$), α -helix ($1652\text{-}1660\text{ cm}^{-1}$) and β -turns ($1660\text{ to }1696\text{ cm}^{-1}$) [156,158] dominated in the unsilicified silk/R5 composites (**Figure 2-8A**), which simultaneously diminished in the silicified composites (**Figure 2-8B**). After silicification, the intensity of β -sheet crystalline peak at 1621 cm^{-1} increased in the composites, indicating an increase of the β -sheet content after silicification (**Figure 2-8A, B**). The content of β -sheet increased

after silicification (from $36\pm 3\%$ to $48\pm 4\%$) while the content of non-crystalline structures decreased (α -helix: from $12\pm 2\%$ to $10\pm 1\%$; random coil: from $22\pm 2\%$ to $18\pm 2\%$) (**Figure 2-8C**). Recent work has characterized the secondary structure of the R5 peptide during silicification. The R5 peptide was characterized as a disparate random coil ensemble in solution, which remain unchanged in the presence of silicic acid solution [162]. The increase of beta sheet content in the GSSR5 composites after silicification was due to the formation of crystalline structure in silk protein [163].

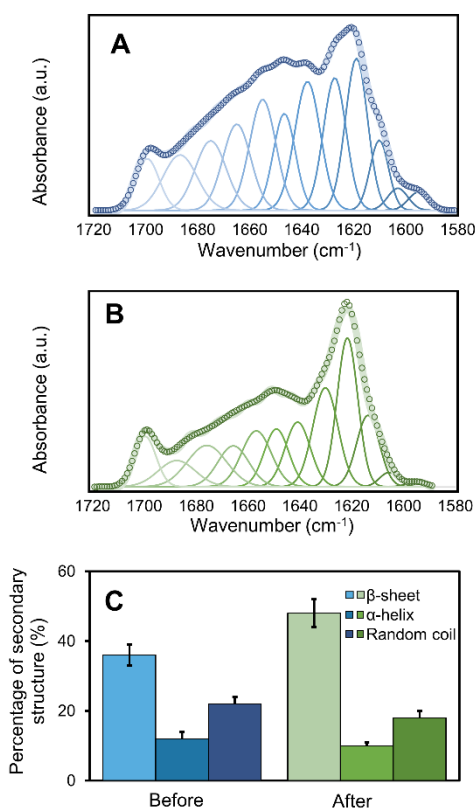


Figure 2-8. Representative Fourier self-deconvolution of amide I spectra for the silk/R5 composite before (A) and after (B) silicification. Percentage of the secondary structural elements in the composites (C). Key: open circles, measured data; wide solid line, summation of Gaussian peaks; thin solid lines, individual amorphous Gaussian peaks. The assignment of amide I bands was taken from the literature [156,158]. The content of

non-crystalline structures including random coil and α -helix simultaneously diminished after silicification (α -helix: from $12\pm 2\%$ to $10\pm 1\%$; random coil: from $22\pm 2\%$ to $18\pm 2\%$), while the percentage of β -sheet crystalline structure increased after silicification (from $36\pm 3\%$ to $48\pm 4\%$).

The secondary structure of the R5 peptides was characterized as disparate random coil ensembles in solution, which remain unchanged during silicification in silicic acid solution, as suggested by circular dichroism spectra and *de novo* structure predictions [162]. Our recent work has demonstrated that the secondary structure of R5 remained unchanged in the silk-R5 conjugates after silicification, as identified by computational simulations [131].

In addition, we characterized the swelling ratio and water uptake percentage of the gradient composites (**Figure 2-9, 2-10**). The hydration properties of silk composites are valuable impactors on bone tissue formation. The swelling ratios of the low, medium and high regions in the GSSR5 composites are 11.0 ± 1.6 , 8.2 ± 0.5 , 5.4 ± 1.3 , respectively, while the water uptake percentage of the low, medium and high regions are $95.7\pm 0.02\%$, $91.9\pm 0.04\%$, $92.4\pm 0.05\%$, respectively. The silk scaffolds with a corresponding decrease in pore sizes showed decreased swelling ratio. Water uptake of the aqueous-derived scaffolds in distilled water remained constant, regardless of the concentration of silk fibroin and pore sizes in the scaffolds.

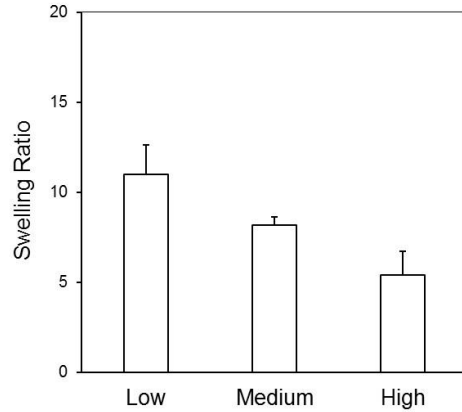


Figure 2-9. Characterization of swelling ratio in the gradient composites.

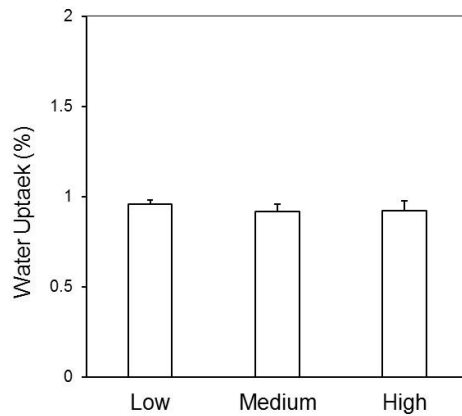


Figure 2-10. Characterization of water uptake percentage in the gradient composites.

Our recent work has characterized the hydration properties of silk-based scaffolds for bone tissue engineering and their effects on bone formation [160,164–166]. Silk based scaffold materials offered beneficial hydrophilicity for cell adhesion and survival, while also maintained appropriate swelling ratio to avoid scaffold deformation [160,164–166]. There was no significant difference in cell proliferation in silk scaffolds with different pore sizes and the corresponding swelling ratios [160]. Furthermore, quantification of bone

differentiation parameters showed that silk scaffolds with different pore sizes and the corresponding swelling ratios resulted in comparable calcium deposition and bone volume [164]. In summary, silk based materials offered beneficial hydrophilicity for cell adhesion and survival, while also maintaining appropriate swelling ratios to avoid scaffold deformation, as demonstrated in our previous work [77, 85-87].

2.5 Conclusions

3D GSSR5 composites were developed through integration of enzymatically triggered protein gelation and R5-induced gradient silicification. This composite system offers continuous transitions in terms of composition, structure and mechanical properties. Highly tunable silk elastomers were created with gradient inclusion of mineralization domains. The spatial distribution of functional peptides coupled into the hydrogel lead to patterning gradients of mineralization domains with varied sizes and density, which in turn impact the physical gradient of the system, such as mechanical stiffness, porosity and topology. These features will ultimately interact with the cellular response to the composites and can be optimized to achieve proper physical and biochemical properties in order to support cell proliferation, distribution and differentiation, thus enhance the osteochondral regeneration in these 3D systems. This novel biomaterial design offers a promising strategy to meet a broad range of needs in regenerative medicine involving osteochondral tissue engineering, as well as graded tissue interfaces.

3. Chapter 3. Directing *in vitro* cell differentiation towards osteochondral lineages in the gradient systems for osteochondral tissue engineering

3.1 Abstract

The composite system exhibited continuous transitions in terms of composition, structure and mechanical properties, as well as cytocompatibility and biodegradability. The gradient silicified silk/R5 composites promoted and regulated osteogenic and chondrogenic differentiation of human mesenchymal stem cells in an osteoinductive and chondro-inductive environment *in vitro*, respectively. The cells differentiated along the composites in a manner consistent with the cellularity trends in osteochondral tissues. Moreover, these continuous gradient structures endowed the composites with gradient ECM deposition. This novel biomimetic gradient biomaterial design offers a useful approach to meet a broad range of needs in regenerative medicine.

3.2 Introduction

Gradient silk protein-based composites coupled with the silica selective peptide R5 were generated with versatile and tunable spatial gradients of mineralization domains in 3D biomaterial substrates. The resulting composite system offered gradient chemical, mechanical and structural properties that mimic the intricate features of osteochondral interface tissues. These functional protein/mineral systems can be used to direct localized *in vitro* stem cell differentiation towards osteogenic and chondrogenic lineage for osteochondral tissue engineering.

3.3 Materials and Methods

3.3.1 hMSC culture in the gradient systems

Human mesenchymal stem cells (hMSCs) were isolated from fresh bone marrow aspirate (Lonza, NJ, USA) from a healthy, non-smoking, young male as previously described [167]. hMSCs were cultured in expansion medium containing Dulbecco's modified eagle medium (DMEM) supplemented with 10% fetal bovine serum (FBS), 1% non-essential amino acids, 1% antibiotic/antimycotic (100U mL⁻¹ penicillin, 100 µg mL⁻¹ streptomycin, 0.25µg mL⁻¹ fungizone) and 1 ng/ml fibroblast growth factor-basic (bFGF). For cell seeding, gradient silicified silk/R5 hydrogels were frozen at -20°C, lyophilized and autoclaved for sterilization. Cells at passage 2–3 were seeded at 1 million per GSSR5 composite (50 µl volume), and allowed to attach for 1 hours prior to flooding the composites with growth media. The growth medium contained DMEM supplemented with 10% FBS, 1% non-essential amino acids and 1% antibiotic/antimycotic. All cell cultures were incubated at 37°C supplemented with 5% CO₂. After 24 hours, the cultures were switched to osteogenic differentiation medium consisting of DMEM with 10% FBS, 1% antibiotics-antimycotic, 1% non-essential amino acids, 10 mM β-glycerol-2-phosphate (Sigma-Aldrich), 100 nM dexamethasone (Sigma-Aldrich), and 0.05 mM L-ascorbic acid (Sigma-Aldrich). For chondrogenic differentiation, the cultures were maintained in chondrogenic differentiation medium at 37°C supplemented with 5% CO₂. The medium was changed every 2-3 days. Unsilicified plain silk hydrogel scaffolds served as controls.

hMSC proliferation in the composites was monitored by Alamar blue dye reduction assay following the manufacturer's protocol. Viable cells in the composites after 19-day culture were observed using a live/dead assay kit. The actin expression of hMSCs in three-

dimensional (3D) cell culture was visualized by fluorescence F-actin staining following the manufacturer's instructions.

3.3.2 Histology

The samples were harvested after 6 weeks of culture in osteogenic media and fixed in 4% phosphate-buffered saline (PBS)-buffered paraformaldehyde at 4°C overnight. The samples were then dehydrated through graded ethanol (70%, 90%, 95% and 100%), embedded in paraffin and sectioned at 8 µm thickness. Hematoxylin and eosin (H&E) staining was performed based on standard histochemical techniques. Calcium deposition was analyzed using the von Kossa stain method [168]. Sirius red staining was performed using the Picro-Sirius red stain kit (Abcam, UK) according to the manufacturer's instructions for the assessment of collagen fibers. The proteoglycan expression of hMSCs in three-dimensional (3D) cell culture was visualized by Alcian blue staining following the manufacturer's instructions. Samples were imaged using a BZ-X700 series microscope (Keyence, IL, USA).

3.3.3 Immunohistochemistry

Samples were harvested after 6 weeks of culture in osteogenic media and fixed in 4% PBS-buffered paraformaldehyde overnight. The samples were dehydrated through graded ethanol (70%, 80%, 90%, 95% and 100%), embedded in paraffin and sectioned (8 µm). Immunostaining of collagen type I were performed based on standard immunohistochemical techniques. Briefly, tissue sections were rehydrated and treated with 5% BSA for 1 h. The samples were treated with anti-collagen I or collagen II antibodies (Abcam, UK) for overnight at 4°C and then washed with PBS. The samples were stained with secondary antibodies (Abcam, UK) for 1 h at room temperature and

washed with PBS. Images were taken on a BZX-700 microscope (Keyence Corporation, IL).

3.3.4 Gene expression.

Samples were collected at desired time points, rinsed in PBS and stored in TRIzol reagent at -80°C until analysis. Total RNA was isolated using the PureLink® RNA Mini Kit. The RNA was reverse-transcribed to synthesize cDNA using the High Capacity cDNA Reverse Transcription Kit according to manufacturer's instructions. Real-time PCR amplification was performed on 1 µg cDNA using TaqMan® Universal PCR Master Mix with an ABI Prism 7000 Sequence Detection System (Applied Biosystems, USA). Primer sequences from TaqMan® Gene Expression Assays included the housekeeping gene glyceraldehyde 3-phosphate dehydrogenase (GAPDH, Hs99999905_m1), osteogenic genes Runt-related transcription factor 2 (Runx2, Hs00231692_m1), collagen type I (Col1, Hs00164004_m1), alkaline phosphatase (ALP, Hs01029144_m1), and bone sialoprotein (BSP, Hs00173720_m1). Gene expression was normalized to GAPDH using the comparative Ct ($2^{-\Delta\Delta Ct}$) method.

3.3.5 Statistical analysis

Paired or unpaired Student t-tests, as appropriate, were used to determine statistical differences between groups. One-way ANOVA was used when comparing features between groups. In all cases, n > 3 were used for data sets (p < 0.05 or 0.01). GraphPad software (GraphPad Prism software, CA) was utilized.

3.4 Results and Discussion

3.4.1 Cytocompatibility evaluation of the GSSR5 composites.

The lyophilized GSSR5 composites with gradient matrix pore structure were seeded with hMSCs to guide cell growth and proliferation and to evaluate the cytocompatibility of the

composites in comparison with uniform silk/R5 composites and unsilicified plain silk controls. After a 19-day culture, hMSCs exhibited favorable metabolic activity, spread out their actin filaments and aligned with the pores of the composites with uniform distribution (Figure 3-1A, D).

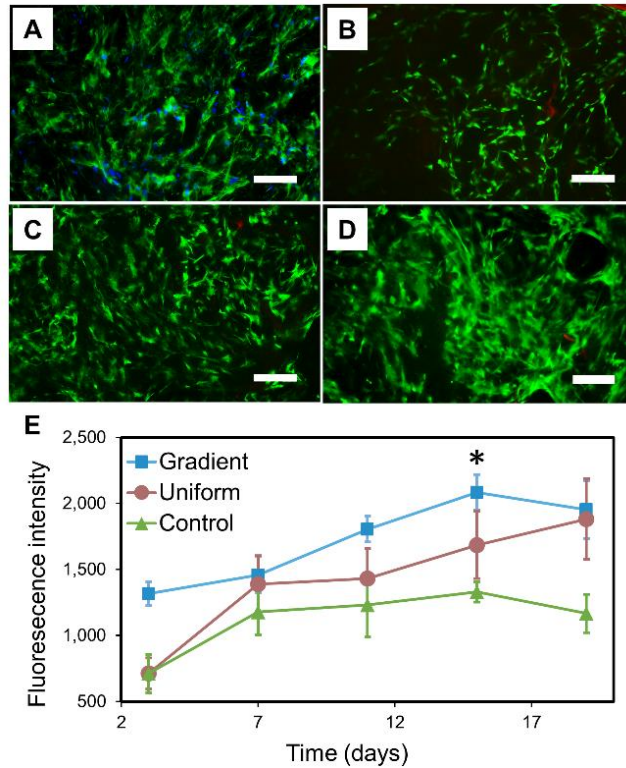


Figure 3-1. Fluorescence staining of actin (green) and nuclei (blue) of hMSCs in the GSSR5 composites in growth medium at day 19 (A). hMSCs spread out actin filaments, aligned with the pores and evenly distributed in the GSSR5 composites after 19-day culture. Live/dead staining of hMSCs cultured in the GSSR5 composites in growth medium at day 3 (B), day 11 (C) and day 19 (D). Strong green fluorescence with minimal visible red fluorescence demonstrated the cytocompatibility of the material. Alamar blue assay (E) showed the proliferation of hMSCs in the gradient (square), uniform (circle) and unsilicified plain silk control (triangular) composites over a 19-day period (n>3). Uniform silicified silk/R5 composites had a silk/R5 molar ratio of 1/125. Unsilicified plain silk

composites served as controls. Scale bar, 200 μm . (*Significantly different from day 3 ($p < 0.01$))

Alamar blue assay showed comparable proliferation of hMSCs in the gradient, uniform and control groups during the culture (**Figure 3-1E**). There was a significant increase of fluorescence intensity from day 3 to day 15 indicating favorable cell proliferation in all groups during the culture period ($p < 0.01$). Strong green fluorescence with minimal visible red fluorescence (**Figure 3-1 B-D**) was detected from the live/dead staining of hMSCs in the GSSR5 composites during the culture, indicating the cytocompatibility of the material.

3.4.2 The GSSR5 composites offered tunable osteogenic differentiation and calcium deposition in 3D cell culture.

hMSCs were seeded into the lyophilized GSSR5 composites and unsilicified plain silk controls and cultured under osteogenic conditions for 6 weeks. H&E staining revealed heterogeneous cell morphologies, e.g., enlarged cuboidal cells in the regions with high peptide loading, while most cells remained undifferentiated with a more elongated shape in the regions with low peptide loading, as well as in the unsilicified plain silk controls (**Figure 3-2 A-D**).

Von Kossa staining revealed increased calcification in the GSSR5 composites with high loading of peptide, compared to the medium and low loadings and to the controls (**Figure 3-2 E-H**). Histological analysis revealed that hMSCs cultured in high regions deposited minerals more intensely which clustered in the interstitial spaces of the pores and extended to the walls of the pores, while the medium and low regions showed less mineral deposition. Unsilicified controls showed minimal staining of calcium. The area ratio of calcium staining in the low regions were significantly lower than those in the medium regions,

which were lower than those in the high regions in the gradient composites (**Figure 3-3**, $p < 0.01$).

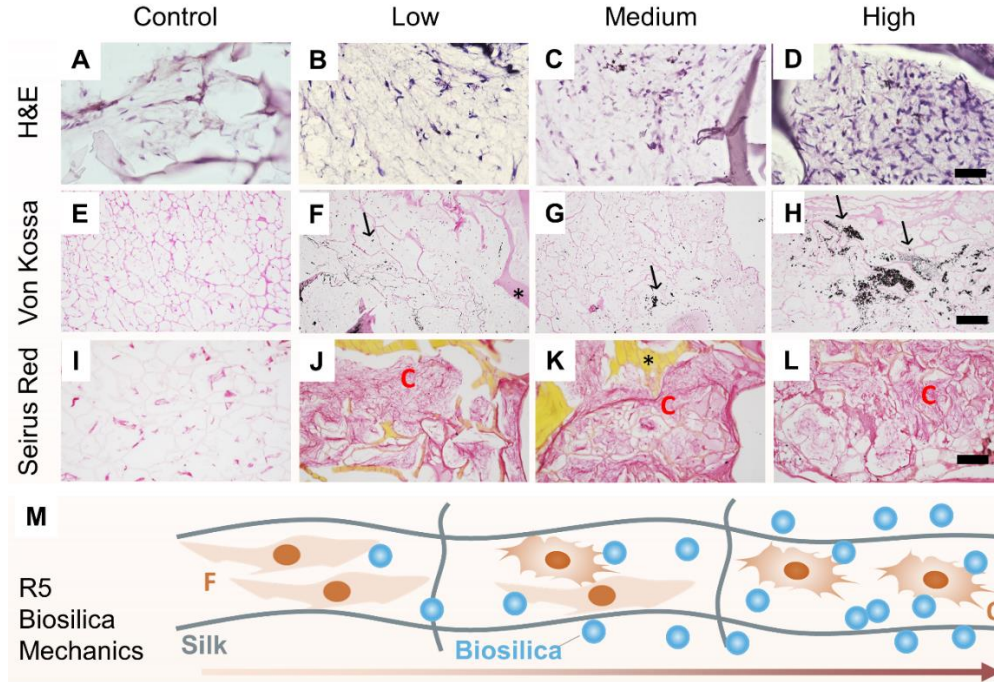


Figure 3-2. Histological sections taken from the unsilicified plain silk controls (A, E, I), and the GSSR5 composites with low (B, F, J), medium (C, G, K) and high (D, H, L) loadings of the R5 peptide after 6-week culture of hMSCs in osteogenic medium. H&E staining (A, B, C, D), von Kossa staining (E, F, G, H) and Sirius red staining (I, J, K, L). Schematic representation of cell differentiation along the GSSR5 composites (M). Scale bar, 50 μm (A-D); 200 μm (E-L). Unsilicified plain silk composites served as controls. Arrows indicate calcification; asterisks indicate composites. O, osteoblast-like cells; C, collagen-like bundles; F, fibroblast-like cells.

Sirius red staining confirmed the secretion of collagen fibers in the GSSR5 composites (**Figure 3-2 J, K, L**), whereas minimal collagen fibers were present in the controls (**Figure**

3-2I). The deposition of bone-specific ECM in the gradient composites was evidenced by immunofluorescence staining of collagen type I which is the major bone matrix component [169,170]. Regions with high loading of the peptides showed stronger expression of collagen type I compared to the medium regions, while minimum expression of collagen type I was observed in the low regions of the gradient composites as well as in the controls (**Figure 3-4**). Bone-like tissue formation was supported within the high region of the composites, while most cells remained in undifferentiated state in the low region. The cells differentiated along the composites in a manner consistent with the R5-gradient profile (**Figure 3-2M**).

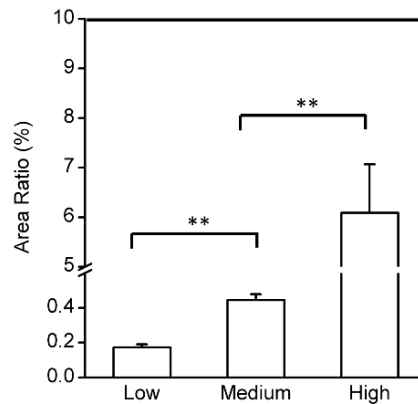


Figure 3-3. Characterization of the area ratio of calcium staining by von Kossa in the gradient composites. (**Significantly difference ($p < 0.01$))

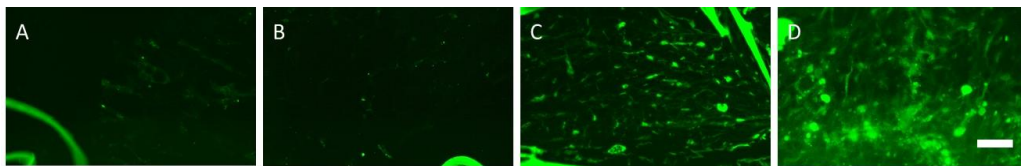


Figure 3-4. Immunostaining of collagen type I taken from the unsilicified plain silk controls (A), and the GSSR5 composites with low (B), medium (C) and high (D) loadings of the R5 peptide after 6-week culture of hMSCs in osteogenic medium. Scale bar, 50 μm .

After six weeks of culture, strong transcript levels of bone markers (Runx2, collagen type I, ALP and BSP) were observed in hMSCs cultured in the lyophilized GSSR5 composites and uniform silk/R5 composites compared to the unsilicified silk controls represented by the baseline (**Figure 3-5**). A significant increase in Runx2 transcript levels in the GSSR5 and uniform composites was observed after 6 weeks ($p < 0.05$) (**Figure 3-5A**), supporting the commitment of these composites to induce hMSC differentiation toward the osteogenic lineage.

The expression of collagen type I, the most abundant extracellular matrix protein in bone, was comparable between all four groups after 6-week culture (**Figure 3-5B**). The expression of alkaline phosphatase was up-regulated by 2-fold in regions with high loading compared with that in the controls (**Figure 3-5C**), indicating advanced osteoblast development and matrix maturation to prepare for mineralization in the high region [171]. Moreover, the expression of BSP, the late-stage osteogenic differentiation marker, was significantly improved in the GSSR5 and uniform composites than that in the controls after 6 weeks ($p < 0.05$, **Figure 3-5D**), which further supported the upregulation of osteogenesis in these composites.

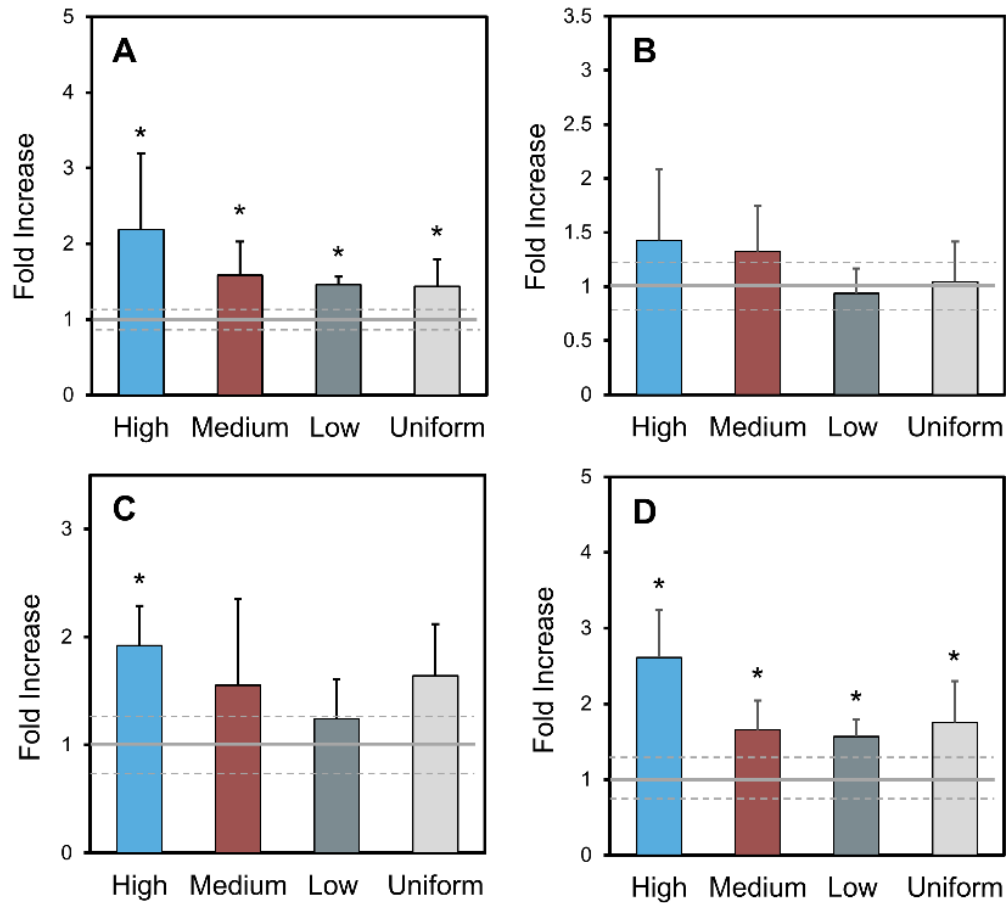


Figure 3-5. Transcript levels from hMSCs cultured in the GSSR5 composites under osteogenic conditions after 6 weeks. Expression of Runx2 (A), collagen type I (B), alkaline phosphatase (ALP, C) and bone sialoprotein (BSP, D). Data are shown relative to the expression of the respective genes in hMSCs cultured in unsilicified plain silk controls. Uniform silicified silk/R5 composites had a silk to R5 molar ratio of 1 to 125. The solid grey line represents the average of control and standard deviation is represented by dashed grey line. (*Significantly different from unsilicified silk controls ($p < 0.05$))

3.4.3 The GSSR5 composites offered tunable chondrogenic differentiation and cartilage-like ECM deposition in 3D cell culture.

After 4 weeks of hMSC culture in chondrogenic medium, round cells and positive extracellular matrix staining by Alcian blue and collagen type II staining were observed in low regions of the gradient composites, while most cells in medium and high regions appeared to be elongated shape with less ECM staining observed (**Figure 3-6**). The formation of the proteoglycan-rich matrix in the gradient composites indicated that these composites could be expected to support the formation of cartilaginous tissue during osteochondral regeneration corresponding to the distribution and structure of native hyaline cartilage.

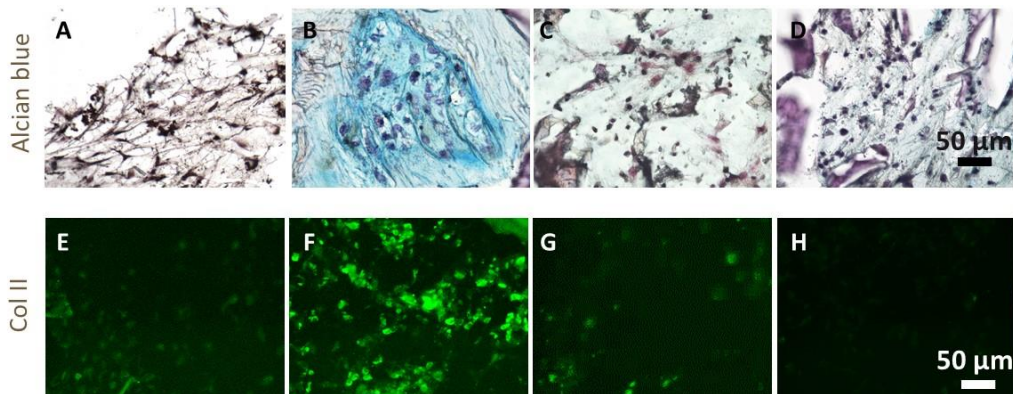


Figure 3-6. Alcian blue (A-D) and collagen type II (E-H) staining of histological sections taken from the GSSR5 composites with control (A, E), low (B, F), medium (C, G) and high (D, H) loadings of the R5 peptide after 4-week culture of hMSCs in chondrogenic medium. The formation of the proteoglycan-rich matrix in the gradient composites indicated that these composites supported the formation of cartilaginous-like tissue. Scale bar, 50 µm.

In summary, when seeded with hMSCs and cultured in osteogenic medium, the GSSR5 composites showed elevated transcript levels of the osteogenic genes, increased collagen

secretion and calcium deposition when compared with the unsilicified silk controls. Increased osteogenic gene expression corroborates the development of advanced osteoblasts, the maturation of extracellular matrix and mineral accumulation [102]. The formation of the proteoglycan-rich matrix in the gradient composites indicated that these composites supported the formation of cartilaginous-like tissue. Appropriate matrix design is crucial to successful tissue engineered interface grafts and provides a foundation to explore the mechanics and biological function. This gradient silk/silica matrix with structurally, mechanically and biologically relevant properties is considered to eventually meet the needs for tissue engineered osteochondral interface grafts, while there are clearly many steps to go before *in vivo* validation can be pursued.

The GSSR5 composites combined two key structural properties—strength of the protein templates and toughness of biosilica. Biosilica can effectively stimulate osteoblast differentiation, inhibit osteoclastic activity and enhance mineral deposition in bone tissue [172]. However, the degradability of biosilica is limited, and the materials by themselves are brittle, which make it difficult to generate useful 3D materials [173,174]. To solve these problems, several silk/R5/biosilica composites [73,113,175] have been developed for osteogenesis in the form of two-dimensional (2D) films, due to the excellent biocompatibility [141,176,177], tunable mechanical properties [161], and low inflammatory response [178,179] of silk. In these systems, the R5 peptide has been either genetically [73,113,114,175] or chemically [114] fused to the silk to control the assembly and deposition of the silica particles in the silk films for osteogenesis. The R5 peptide contains lysine residues which are crucial in mediating the polycondensation of silica nanospheres during silicification [180,131]. Previous work has demonstrated that the R5 peptides promoted the intermolecular interactions of biosilica particles and the peptide. The hydrophobic nature of the R5 peptide led to entropically favored peptide aggregates,

while the positively charged residues on the R5 peptide activated silica precipitation through an electron-donor-acceptor mechanism [128,131]. The combination of the silk and silica promoted the osteogenic differentiation of hMSCs and enhanced nodular mineral deposits on the films. Biosilica also accelerated cell proliferation, upregulating osteoprotegerin (OPG) and bone morphogenetic protein 2 (BMP2) expression in osteogenic cells on silicatein/biosilica-modified substrates [71]. However, several problems still exist, as 2D systems fail to mimic the complex cellular environments *in vivo* [142]. Moreover, constructs with uniform physical and chemical properties lack the spatially and structurally defined hierarchical architecture that exists in native tissues and fail to recreate the natural graded interface [4].

In this study, GSSR5 composites obtained continuous variation in compositional, physiological and mechanical properties and created 3D biomimetic cellular niches for osteogenic differentiation to better mimic the complex cellular environments *in vivo* with more representative response to the external stimuli in the surroundings [142,181]. More importantly, these combined gradients not only offered a favorable platform to template mineral deposition, but also provided a suitable process that reproduced the role of cells. The variation in mineralization, together with the structural and mechanical gradients, triggered the cells to promote localized mineralization within the matrix. Cells deposited minerals to the protein/biosilica matrix which further strengthened and hardened the material itself. Bone-like tissue formation was supported within the subchondral end of the composites (high region), while most cells remained in undifferentiated state in the low region. The spatial osteogenesis of hMSCs along the gradient composites was confirmed by the heterogeneous cell morphologies and varied calcification from the histology results, the gradient expression of collagen type I as well as the elevated transcript levels of selective bone markers in the GSSR5 composites.

In the protein/biosilica composites, the mineralization domains acted as special loci to support the formation and accumulation of HA crystallites with small size and low crystallinity, which are important for the biochemistry of biomineralization [101]. Biosilica bound to the mineralization domains were immobilized in the silk matrix and induced the collagen synthesis [71,95,113,182]. Collagen fibers then further promoted the mineral deposition and bound to apatite crystals resulting in intercalating mineral structure [101,183,184]. Upon the formation of the apatite nuclei, spontaneous growth of apatite occurred by the addition of calcium and phosphate ions from surrounding medium. The features above derived from the molecular-level organic-inorganic interfaces were established by the presence of the R5 peptide template, combined with the regional control of such chemistries within the gradient design.

The GSSR5 composites also transmitted favorable gradient physical stimuli including mechanics, mass and architecture to cells towards osteogenic lineage. These GSSR5 composites exhibited gradient pore microstructures, large pore size and an interconnected pore structure which affected the osteogenic differentiation through various aspects, notably surface area, matrix deposition and nutrient diffusion [164]. Enhanced osteogenesis was observed in the stiffer regions of the GSSR5 composites. This mechanical stimulus, via matrix stiffness, could affect cellular distribution, metabolic activity and the ultimate mechanics of the tissue itself [185,186]. The stem cells differentiating towards osteogenic lineage adhered better to rigid substrates and tended to form mineralized nodules on rough surfaces [164]. More information is needed to establish whether differential cell behaviors were due to the biomimetic cues (the R5 peptide, biosilica), the mechanical transitions or the architectures of the composites.

The soft tissue-bone tissue interface is characterized by an elevated level of heterogeneous structural architecture to facilitate joint function [187–189]. This gradient protein/biosilica

system holds benefits in supporting cell growth and differentiation, mimicking the native matrix heterogeneity and exhibiting tunable mechanics, which make it a promising strategy design for interfacial tissue repair. However, limitations in soft tissue-bone repair would need to be addressed before the gradient composites can be used *in vivo*. For example, tendon-bone interface repair exhibits significant clinical challenges in promoting the biological fixation of the engineered grafts with the implant sites and facilitating the functional integration of tendon with bone after injury. Such fixation requires the engineered graft to be pre-incorporated into the strategic design of the replacement grafts in order to restore the function of the tissue interfaces [189–191].

In summary, such composite materials can be used to study the growth of natural tissues and the processes of regeneration, but also to act as tissue engineering constructs *in vitro* and *in vivo*, such as for osteochondral plugs. Silk-based materials offered beneficial hydrophilicity for cell adhesion and survival, while also maintaining appropriate swelling ratios to avoid scaffold deformation, as demonstrated in previous work [160,164–166]. The biocompatibility of the silk-based materials has been demonstrated *in vivo* previously. Silk hydrogels enzymatically crosslinked by HRP and H₂O₂ were implanted subcutaneously in a mouse model and showed progressive cell infiltration and degradation [161]. Also, the system can be easily scaled up to match the dimension of critical osteochondral defects. To this end, further optimization would be useful, such as to extend the range of mechanics through increasing the silk concentration and molecular weight within the composites. The highest mechanics obtained in the GSSR5 composites may not reach that of the native bone, as the stiffness of fresh cancellous human bone is around 700 MPa [192]. However, the scaffold could be supported by the surrounding bone and invaded by the formation of new bone during degradation.

More importantly, the incorporation of biosilicification domains into the biocompatible silk substrates under mild (peptide-mediated) conditions provides other potential applications. Surface modifications of the inert biosilica particles would allow for encapsulation of biomolecules, e.g., enzymes, and drugs which are sensitive to heat or caustic chemicals [151]. The incorporation of biosilicification domains into the silk substrates also provides opportunities to encapsulate various functional peptides and molecules. For example, a variety of polycationic peptides e.g. silaffin that are able to precipitate silica nanospheres individually can be encapsulated in the silk substrates, leading to advanced functional materials with different mineral morphology and organization [39,88]. Depending on the peptide used for biomineralization and the external physical/chemical stimuli, different silica structures can be generated including sphere-like (with R5), fibrous structures (with p-(lys)1642) and platelike (with p-(lys)189) *in vitro* [193]. This novel gradient biomaterial design offers a useful approach to meet a broad range of needs in regenerative medicine involving interfacial tissue engineering.

3.4.4 Conclusions

3D GSSR5 composites were developed through integration of enzymatically triggered protein gelation and R5-induced gradient silicification. This composite system offers continuous transitions in terms of composition, structure and mechanical properties as well as cytocompatibility and biodegradability. The GSSR5 composites were competent to promote and regulate the osteogenic and chondrogenic differentiation of human mesenchymal stem cells *in vitro* respectively. The cells differentiated along the composites in a manner consistent with the trends in osteochondral tissues. This novel biomaterial design offers a promising strategy to meet a broad range of needs in regenerative medicine involving osteochondral tissue engineering, as well as graded tissue interfaces. Furthermore, this strategy offered a platform to create clinically relevant tissue engineered

composites through encapsulating other functional molecules and proteins and to screen for optimal doses and combinations in a 3D environment.

4. Chapter 4. Coding cell micropatterns through peptide inkjet printing for arbitrary biomineralized architectures

4.1 Abstract

Well-designed micropatterns present in native tissues and organs involve changes in extracellular matrix compositions, cell types and mechanical properties to reflect complex biological functions. However, the design and fabrication of these micropatterns *in vitro* to meet task-specific biomedical applications remains a challenge. We present a *de novo* design strategy to code and synthesize functional micropatterns to engineer cell alignment through the integration of aqueous-peptide inkjet printing and site-specific biomineralization. The inkjet printing provides direct writing of macroscopic biosilica selective peptide-R5 patterns with micrometer-scale resolution on the surface of a biopolymer (silk) hydrogel. This is combined with *in situ* biomineralization of the R5 peptide for site-specific growth of silica nanoparticles on the micropatterns, avoiding the use of harsh chemicals or complex processing. These well-designed protein/mineral systems were used to align human mesenchymal stem cells and bovine serum albumin. This combination of peptide printing and site-specific biomineralization provides a new route for developing cost-effective micropatterns, with implications for broader materials designs.

4.2 Introduction

Micropatterns are characteristic and intriguing features widely found in native tissues and organs, such as diatoms, plant cell walls, arthropod exoskeletons and bones, among many other systems [28,29]. These bio-micropatterns enhance mechanical performance (such as strength and toughness) of tissues and organs, and also support biological functions, including structural support, defense and prey capture, yet formed from a limited set of components (e.g., proteins, polysaccharides, minerals) [30,31]. For example, the highly

ordered periodic hexagonal or plywood-like micropatterns found in diatoms and arthropod exoskeletons enhances toughness thousands of times greater than the pristine minerals, and the iridescence derived from these features (known as structural color) provides adaptive biological functions such as mating, signaling or camouflage [28,32–34]. Axially aligned cell micropatterns in human muscle tissues provide structural anisotropy to maintain contraction and tension resistance for tendons to facilitate mechanical functions, motility and survival [35]. The spatial oriented micropatterns of collagen as parallel fiber bundles in tendons, concentric waves in bone and oriented fibrils in cartilage, are always accompanied with mechanical benefits and support cellular functions to these tissues and organs [36–38].

A variety of biomineralization strategies have been applied to mimic the components, structure and function of natural micropatterned tissues, including photolithography, microcontact printing and laser patterning, among others [31,35,39–41]. The resultant micropatterns suggest promising applications in regenerative medicine, microelectronics, drug screening, and optical and biomedical sensors [42,79]. In particular, silica-based micropatterns play a critical role in many biomedical fields, including tissue engineering, controlled drug delivery, cell transplantation, optics, electronics as well as *in vitro* tissue models, due to the outstanding biocompatibility, high versatility and osteoinductive properties of silica [39,42–45]. However, most of these silica patterns are created in harsh conditions, such as extremely high temperature and/or pressures, strongly acidic solutions, or complicated and energy-intensive processing techniques [194]. Moreover, the silica patterns generated by these methods usually exhibit weak substrate bonding to rigid substrates, thus can be damaged easily due to the inherent brittleness of silica [42]. These features reduce the broader utility of these systems due to costs or material weak points,

and certainly limit direct processing and integration with biological components such as cell or bioactive therapeutics.

In contrast, organisms such as diatoms, which are known for their complex and intricate silica architectures, construct silica micro-/nano- patterns with precise control through bottom-up growth under physiological and ambient conditions without additional chemical treatments or post-processing steps [65]. For instance, biosilica morphogenesis in the diatom cell wall consists of a matrix of organic macromolecules, *i.e.*, native silaffin-1A (natSil-1A) protein for silica formation and native silaffin-2 (natSil-2) protein for biosilica template organization. During *in vivo* silicification, natSil-1A triggers and mediates the formation of the silica particles, while natSil-2 moderates the activities of natSil-1A to form organized patterns through molecular self-assembly and phase-separation processes [65,94].

Inspired by the route that nature uses to synthesize micropatterns, in the present study, we present a *de novo* strategy to code and synthesize bio-micropatterns for engineering cell alignment. A series of previous studies have confirmed that micropatterns play a dominant role in controlling cell-to-cell interactions, the microenvironment of individual cells and in turn the decisions related to cell differentiation [79,195,196]. Here, the core methodology for the design is the synergistic integration of aqueous-peptide inkjet printing and site-specific biomineralization. The inkjet printing allows for non-contact, maskless, direct arbitrary coding micropatterns with versatility and repeatability, and more importantly, can be scaled-up to accelerate material assembly processes [197,198]. Piezo-electric driven actuator dispenses droplets at different volume in a drop-on-demand (DOD) inkjet printer, which can accept a wider range of ink and cause less damage to bioactive substances as compared to thermal actuation [197,199,200]. When in combination with functional inks and/or active substrates, this technique can be utilized in biofabrication for applications in

biosensors, therapeutics, and regenerative medicine[200–202]. Nature typically constructs patterns during growth phases, which is usually a slow process that takes place over months to years or even hundreds of years. This low production efficiency cannot match the requirements of commercial production. In contrast, site-specific biomineralization (*in situ* biosilicification) can form well-organized silica structures on the micropatterns while avoiding the use of harsh chemicals and energy-intensive processing. Furthermore, the silk fibroin (hereinafter referred to as silk) protein-based substrates offer biocompatibility, degradability and tunable mechanical properties to meet different requirements related to biomaterials, tissue engineering and regenerative medicine depending on the specific goal of a project [123,203]. Through these synergistic approaches, we obtained macroscopic silica patterns with micrometer resolution. The dimensions of these micropatterns can be initiated at small scale, while also scalable to sub-meters to match the dimension of human tissues (e.g., centimeter to meter scale) [198]. Finally, *in vitro* cell culture experiments confirmed that human mesenchymal stem cells (hMSCs) successfully aligned with the printed silica patterns on the silk hydrogels. Fluorescence microscopy showed that bovine serum albumin (BSA) was aligned to the R5/biosilica micropatterns. This combination of peptide printing and site-specific biomineralization provides a new route for developing cost-effective micropatterns, with implications for broader materials designs.

4.3 Materials and Methods

4.3.1 Materials

All chemical reagents used for making the micropatterned hydrogels were purchased from Sigma-Aldrich (St. Louis, MO) unless otherwise specified. All materials and reagents used for cell culture and analysis were purchased from Thermo Fisher Scientific (Waltham, MA) unless otherwise specified.

4.3.2 Preparation of aqueous silk fibroin solution

Silk fibroin solutions (referred to silk in the paper) were prepared using our previously established procedures [152]. Briefly, ten grams of silk cocoons were cut into pieces and boiled in 4 L of 0.02 M sodium carbonate solution for 30 min to remove the coating of sericin protein. Degummed fibers were rinsed with deionized water three times and dried in air overnight. Five grams of dried fibers were dissolved in 20 ml of 9.3 M lithium bromide solution at 60°C for 4 h. The silk solution was then dialyzed against deionized water using a dialysis cassette (Pierce 3.5 kDa MWCO; Fisher Scientific, PA) for 2 days. The solubilized silk solution was then centrifuged twice at 9000 RPM, 4°C for 20 min to remove insoluble particulates. Protein concentration was determined by drying a known mass of the silk solution at 60°C for 12 h and measuring the mass of the remaining solid.

4.3.3 Inkjet printing of the R5 peptide on the silk protein substrate

The biosilica selective peptide R5 (H-SSKKSGSYSGSKGSKRRIL-OH) with a purity of 95% was synthesized by GenScript (Piscataway, NJ). Lyophilized horseradish peroxidase (HRP, type VI) powder and the R5 peptide powder were dissolved in deionized water to form a stock solution of 1000 U/mL and 100 mg/mL, respectively. To initiate the silk gelation, 6 μ L of 1kU/ml HRP and 5 μ L of 1% H₂O₂ solution were mixed with 1 mL of 6 wt% silk solution in a pre-made polydimethylsiloxane (PDMS) mold (size L×W×T: 60×24×0.6 mm), and left at 37°C for 8 minutes before printing the R5 peptide [139]. The printing was conducted at ambient conditions by a Dimatix Material Printer DMP-2830 equipped with Dimatix Materials Cartridges (DMS-11610 21 μ m nozzle diameter, Fujifilm, Santa Clara, CA). A custom designed jetting waveform was created, and the R5 peptide solution was jetted at two firing voltages 40V and 25V to achieve different drop volume. Gap spacing between lines were 20 μ m, 50 μ m, 100 μ m or 200 μ m. Drop spacing was 20 μ m. The distance between the print head and the substrate was 300 μ m. After printing, the

silk hydrogel was left in a humidified chamber at room temperature for 2 hours to allow sufficient bonding between the silk hydrogel and the R5 peptide.

4.3.4 *In vitro* silicification.

Biosilica deposition was introduced into the patterned hydrogels post printing. Pre-hydrolyzed tetraethoxysilane (TEOS) solution was prepared by mixing 223 μl of TEOS solution with 776 μl of 50% ethanol/water solution, 10 μl of 1 M hydrogen chloride (HCl) and left at room temperature for 15 min. The patterned hydrogel was then covered by 1 ml silicifying medium consisting of 30 μl prehydrolyzed TEOS solution and 970 μl buffer solution (65 μl 1 M bis-tris propane, 35 μl 1 M citric acid solution and 870 μl deionized water) and allowed for silicification at room temperature for 12 hours, respectively. After silicification, the patterned hydrogels were rinsed with DI water to remove excess reagents and stored at 4°C for further characterization.

4.3.5 Morphology and structural characterization

The morphologies of the micropatterns were characterized by scanning electron microscopy (SEM, Ultra 55 field emission scanning electron microscopy, Carl Zeiss, AG) at an acceleration voltage of 5 kV. To prevent electrical charging, all specimens were coated with a 5-nm-thick Au layer before observation. The samples used for morphology characterization were treated by critical point drying (Tousimis 931 GL, MD). The structures of the biosilica nanoparticles were characterized by Atomic Force Microscopy (AFM) on a MFP-3D-BIO AFM instrument (Asylum Research, CA) in tapping mode. NP-O10 SiN probes were used ($k = 0.12 \text{ N/m}$, Bruker Corporation, MA). Fourier transform infrared (FTIR) spectroscopy mapping was performed using a Bruker LUMOS FTIR microscope system (Bruker, MA), equipped with a liquid nitrogen cooled mercury cadmium telluride (MCT) detector. The images of samples were obtained in ATR mode

with an individual pixel size about $57 \times 40 \mu\text{m}$ over a field of view of $1032 \times 397 \mu\text{m}$. For FTIR mapping, spectra were collected in the mid-infrared (MIR) range of $800\text{--}3600 \text{ cm}^{-1}$ at a resolution of 4 cm^{-1} with 26 co-added scans. All the data collection and processing were performed using OPUS 6.5 (Bruker, MA) at Harvard University Center for Nanoscale Systems.

4.3.6 Fluorescence microscopy of the fluorescent-labeled peptide

micropatterns

The fluorescein isothiocyanate (FITC)-labeled R5 peptide (FITC-SSKKSGSYSGSKGSKRRIL-OH, GenScript, NJ) was added into the R5 peptide solution in a molar ratio of 1/400. The resultant peptide mixture was used to create the ink for printing, following the same silicification process as described earlier. The FITC-labeled micropatterns on the silk hydrogels were imaged using the BZ-X700 series microscope (Keyence, IL, USA).

4.3.7 hMSC culture

Human mesenchymal stem cells (hMSCs) were isolated from fresh bone marrow aspirate (Lonza, NJ) as previously described[193] and used in the cell alignment study. hMSCs were cultured in expansion medium containing Dulbecco's modified eagle medium (DMEM) supplemented with 10% fetal bovine serum (FBS), 1% non-essential amino acids, 1% antibiotic/antimycotic (100 U ml^{-1} penicillin, $100 \mu\text{g ml}^{-1}$ streptomycin, $0.25 \mu\text{g ml}^{-1}$ fungizone) and 1 ng/ml fibroblast growth factor-basic (bFGF). Patterned hydrogels were sterilized in 70% ethanol for 5 hours prior to cell seeding. Cells at passage 2-3 were seeded onto the patterned and unpatterned control hydrogels from suspension in culture medium at a concentration of $2 \times 10^4 \text{ cells/cm}^2$. Cultures were maintained in growth media containing DMEM supplemented with 10% FBS, 1% non-essential amino acids and 1%

antibiotic/antimycotic. All cell cultures were incubated at 37°C supplemented with 5% CO₂. The actin expression of hMSCs in three-dimensional (3D) cell culture was visualized by fluorescence F-actin staining and counterstained by DAPI following the manufacturer's instructions. Unpatterned plain silk HRP hydrogels served as controls.

4.3.8 Microscopy and analysis

Cell samples were rinsed in PBS and fixed in 4% paraformaldehyde (PFA) for 2 hours. For SEM analysis, samples were serially dehydrated in ethanol, critical point dried under CO₂, Au sputter-coated, and imaged. For confocal microscopy, stained cells were imaged with a Leica DMRX microscope (Leica Microsystems Inc., IL). HMSC alignment was quantified using ImageJ software (NIH, Bethesda, MD) with a plug-in OrientationJ to calculate the directional coherency coefficient of F-actin filaments. The coherency coefficient ranges from 0 to 1. A coherency coefficient close to 1 represented as a slender ellipse, indicating the filaments strongly oriented in the direction of the ellipse long axis and greater cellular alignment [204].

4.3.9 Protein alignment on the micropatterned hydrogels

Fluorescein isothiocyanate (FITC)-labeled bovine serum albumin was added to the R5 peptide solution in a molar ratio of 1/1000. The resultant peptide mixture was used to create the ink for printing, following the same silicification process as described earlier. FITC-labeled BSA alone served as a control. The FITC-labeled micropatterns on the silk hydrogels were imaged using the BZ-X700 series microscope (Keyence, IL, USA).

4.3.10 Statistical analysis

Statistical analysis was performed by paired or unpaired Student t-tests, as appropriate, to determine statistical differences between groups. One-way ANOVA was used when

comparing features between groups. In all cases, $n = 6$ were used for data sets ($p < 0.05$ or 0.01). GraphPad software (GraphPad Prism software, CA) was utilized.

4.4 Results and discussion

4.4.1 *De novo* design strategy to code mineral micropatterns

Figure 4-1a summarizes the bottom-up route to form biosilica micropatterns on protein substrates. The starting steps were to prepare the silk hydrogel substrates and the aqueous peptide ink. The enzymatically crosslinked silk hydrogels were used as protein substrates due to their biocompatibility, degradability and tunable mechanical properties (**Figure 4-1b**).

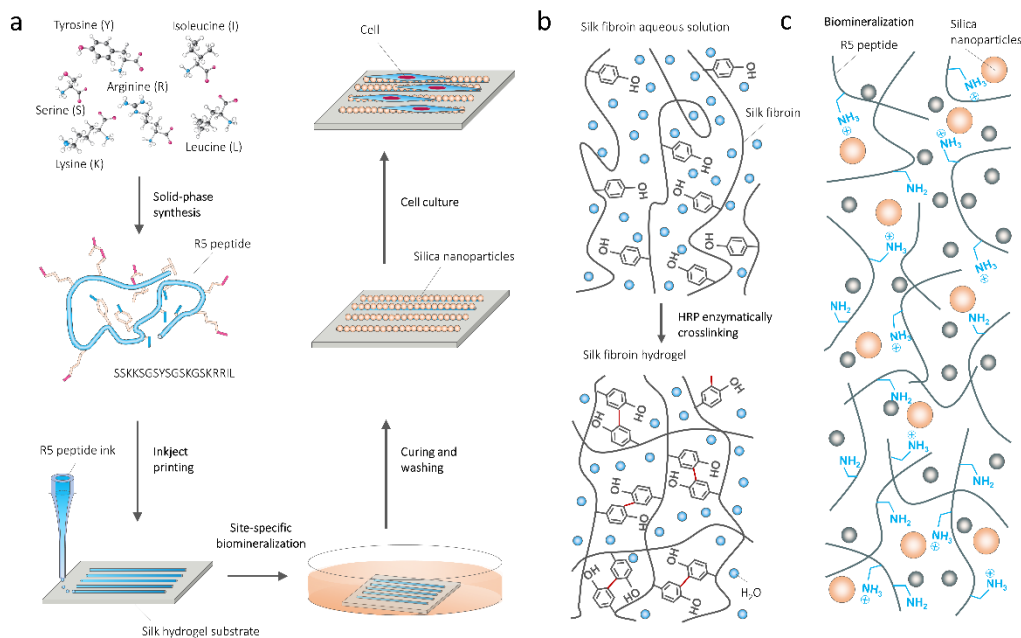


Figure 4-1. Design strategy and processing diagram of coding micropatterns. (a) *De novo* design to create silica bio-micropatterns on protein substrates by *in situ* mineralization of silica-binding peptides and inkjet printing. (b) Silk fibroin hydrogelation mechanism. (c) Biomineralization of biosilica particles catalyzed by the biosilica selective peptide R5.

The biosilica selective peptide-R5, a bioinspired analog derived from the silaffin peptides that are used for silica synthesis in *Cylindrotheca fusiformis*, was selected for the peptide ink since it can directly serve as a trapping agent to trigger the site-specific *in vitro* silicification (**Figure 4-1c**). Our previous studies indicated that enzymatic cross-linking between the silk and R5 molecular chains allowed for tight bonding between the substrate and printed peptide patterns [203].

A freshly printed 1.2 cm-wide peptide logo with micrometer resolution was visually discernable from the transparent underlying silk hydrogel (**Figure 4-2a**). The logo was well bonded with the hydrogels and deformed adaptively with deformation of the hydrogel. Through inkjet printing of FITC-labeled R5 peptide, well-defined peptide patterns on the substrates were evidenced by fluorescence images (**Figure 4-2b**). At the second stage, these all-protein micropatterns were flooded with a silicifying medium consisting of 3 vol% prehydrolyzed TEOS solution in buffer to induce biosilica deposition (*in vitro* silicification) on the micropattern surfaces.

As a result, macroscopic peptide-biosilica patterns with 1.2 cm width were recognized from the transparent silk hydrogel (**Figure 4-2c**). The whole free-standing protein system can be removed from the container and used for further post-processing (**Figure 4-2d**). Our previous studies revealed that the positively charged amino acids dominated the silicification process, while the silk is negative charged³¹. As a result, the silica nanoparticles grew selectively on the R5 peptide patterned surface, represented by the schematic drawing and confirmed by optical imaging and scanning electron microscopy (SEM) (**Figure 4-2e**).

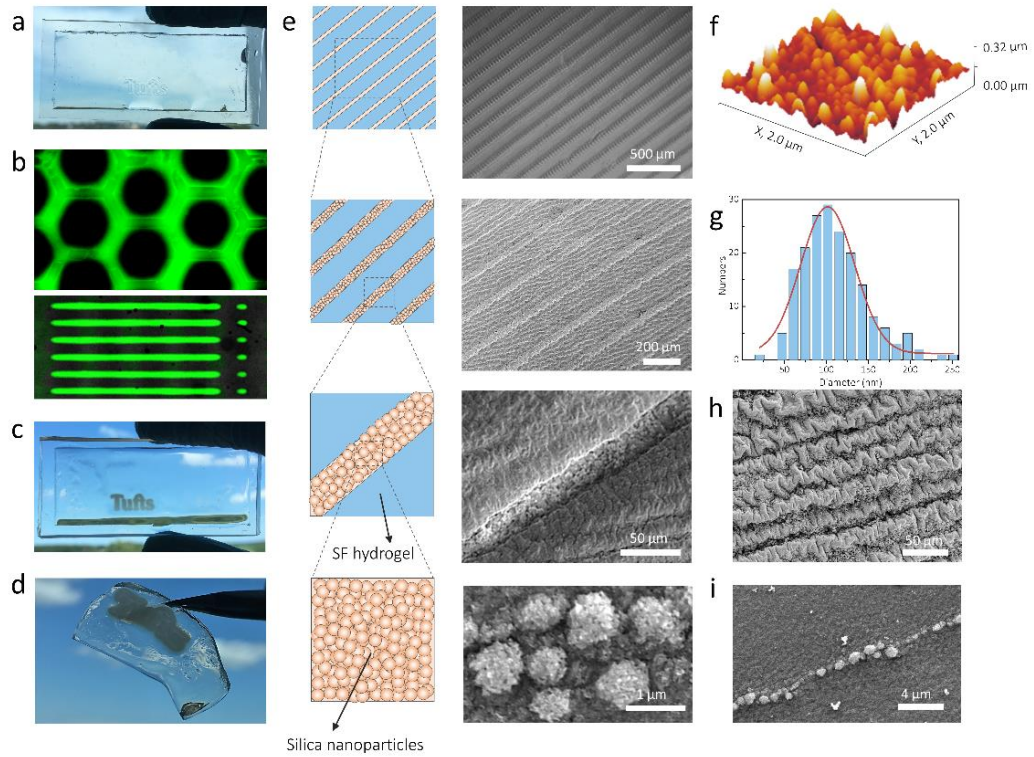


Figure 4-2. Arrays of biosynthesized silica micropatterns on the hydrogel substrates. (a) Visual image shows freshly printed peptide logo with 1.2 cm width on the transparent silk hydrogel. (b) Fluorescence images of FITC-labeled R5 patterns on the silk hydrogels. (c) Visual image shows mineralized peptide logo with 1.2 cm width on the transparent silk hydrogel. (d) The whole free-standing protein system can be easily removed from the container used for gelation. (e) Schematic representation (left) and SEM images (right) show the linear array of mineralized micropatterns printed with different gap spacing between lines on the silk hydrogels. (f) AFM topography image of the silica particles on the mineralized micropatterns scanned over a $2\ \mu\text{m} \times 2\ \mu\text{m}$ area. (g) The corresponding graph of the nanoparticle diameter distribution appears a sharp Gaussian distribution with a center value of $\sim 100\ \text{nm}$, in a range of 50-200 nm. (h, i) SEM images show the spatial resolution of the gap spacing between two lines decreased to $20\ \mu\text{m}$ and the linewidth reached $1\ \mu\text{m}$.

The silica nanoparticles covered the printed R5 peptide lines with individual diameters of 50-200 nm measured from atomic force microscopy (AFM) topography images (**Figure 4-2f, g**). The diameter of these nanoparticles appeared as a sharp Gaussian distribution with a center value of ~100 nm. In contrast, no silica nanoparticles were observed on the silk hydrogel alone surfaces.

We further reduced both the pattern linewidth and the gap between each line by adjusting the drop volume and line spacing during printing to investigate the spatial resolution of the method, with a gap distance between two lines of 20 μm and 1 μm linewidth reached (**Figure 4-2h, i**). Careful examination of the silica nanoparticles on the micropatterns found that the silica nanoparticles remained bound to the pattern surface and even conformed to the wrinkled patterns that were caused by post-processing (ethanol treatment or freeze-drying). Energy dispersive spectrometer (EDS) mapping of Si and corresponding SEM image confirmed the presence of Si on the biosilica micropatterns (**Figure 4-3**).

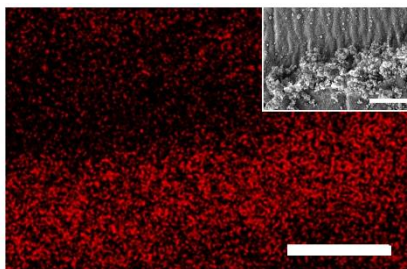


Figure 4-3. EDS map of Si and corresponding SEM image (inserted) confirmed the presence of Si on biosilica micropatterns. Scale bar, 5 μm .

4.4.2 Fourier transform infrared (FTIR) mapping elucidated the structural details of the mineral micropatterns

FTIR spectrometry coupled with microscope detection, supports mapping of spatial and spectral information of the samples simultaneously, enabling chemical visualization of the micro-scale patterns [205–207]. Previous studies demonstrated that FTIR mapping can provide useful information on the composition and conformations of proteins at defined locations with a spatial resolution of ~5-50 μm [205–207]. In this study, a $1032 \times 397 \mu\text{m}$ rectangle micropattern was mapped with the pixel size (spatial resolution) of $57 \times 40 \mu\text{m}$ (**Figure 4-4a**). To chemically image a particular component, the non-overlapping characteristic FTIR absorption for each element was required. Here, Si-O stretching bond ($1300\text{-}1000 \text{ cm}^{-1}$) and amide I band ($1600\text{-}1700 \text{ cm}^{-1}$) were chosen as representative peaks of silica micropattern and silk, respectively. To eliminate thickness inhomogeneities in the samples, the absorbance intensity ratios $A_{\text{Silica}}/A_{\text{Silk}}$ (using A_{1060}/A_{1625}) were integrated for all pixel spectra to obtain chemical images of the micropatterns. Accordingly, in the resulting contour map (**Figure 4-4b**), the red/green and blue represent the strong and weak absorption of silica nanoparticles. It can be found that the strong (red/green) and weak (blue) silica absorption alternate, and the red/green lines in **Figure 4-4b** overlapped with the visual patterns in **Figure 4-4a**, confirming that the silica nanoparticles grew selectively only on the printed patterns.

In addition, FTIR mapping can be used to monitor the secondary structure of the silk in a specific position. **Figure 4-4c** shows the single pixel spectra extracted from the white dashed line range in the FTIR images. The blue and red/green FTIR spectra corresponded to the spectra obtained from the blue (silk substrate) and red/green (silica micropattern) regions, respectively (**Figure 4-4b**). Compared to the spectra in the blue region, the spectra

in the red/green region present significantly weaker absorption in the amide I and II bands, agreeing with the trend observed in the contour map.

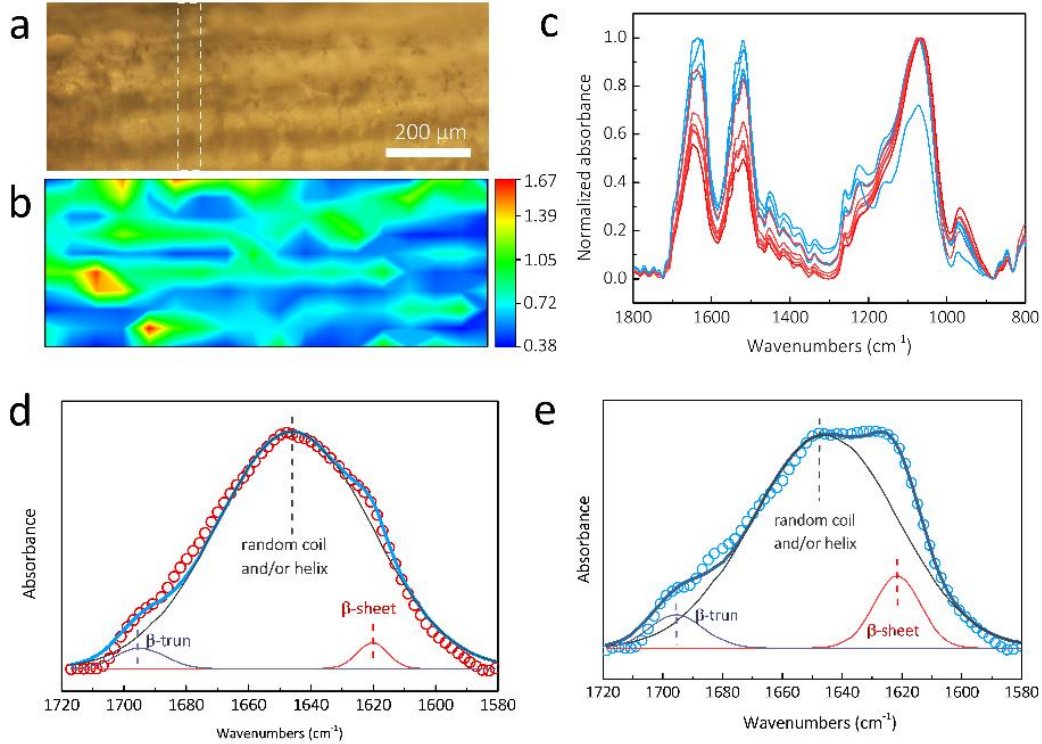


Figure 4-4. FTIR mapping showed the structural details of the biosilica micropatterns on the silk hydrogels. (a) Microscopic image of a $1032 \times 397 \mu\text{m}$ rectangle micropattern. (b) The contour map with the red/green and blue represent the strong and weak absorption of silica nanoparticles. (c) The single pixel spectra extracted from the white dashed line range in FTIR images. Compared to the blue spectra from the blue region of the silk substrate, the red/green spectra from the red/green region of silica micropattern present significant weaker absorption in amide I and II bands. (d) The red/green spectra dominate a sharp peak at 1647 cm^{-1} , which contributed to the random coil and/or helix structure. (e) The blue spectra show the strongest absorption at 1624 cm^{-1} and a shoulder at 1695 cm^{-1} , which were assigned to β -sheets and β -turns, respectively. FTIR, Fourier transform infrared spectroscopy.

More dramatically, the red/green and blue spectra feature distinct maximum absorbance in the amide I band, a useful band to estimate the secondary structure of the silk protein. The red/green spectra dominated a sharp peak at 1647 cm^{-1} , which contributed to the random coil and/or helix structure (**Figure 4-4d**). In comparison, the blue spectra showed the strongest absorption at 1624 cm^{-1} and a shoulder at 1695 cm^{-1} , which were assigned to β -sheets and β -turns of the hairpin-folded antiparallel β -sheet structure of silk, respectively (**Figure 4-4e**).

The deconvolution of the amide I band provided an estimation of β -sheet (crystalline) content in the blue region (silk substrates) at $11\pm 3\%$, while that of the red/green part (micropatterns) was $3\pm 2\%$. These results revealed that the micropatterns had a lower content of β -sheet. Our recent studies on the secondary structure of the R5 peptide before and after silicification characterized the R5 peptide as a random coil structure [203]. Thus, amide I absorption in the micropatterns was mainly contributed by the R5 peptide instead of the silk amide I band at the blue regions. In addition, the β -sheet content of the silk substrate was significantly lower than that of the silk hydrogel obtained with ethanol treatment ($25\pm 3\%$). As a result, these HRP cross-linked hydrogels were transparent due to the limited β -sheet content, while the dityrosine bonds and limited β -sheets acted as crosslink points to form interlocking protein chains to keep the silk hydrogels stable in water.

4.4.3 Cell alignment on mineral micropatterns

To test whether the patterned cues could be used for cell alignment, hMSCs were cultured on the micropatterned hydrogels with line spacings of $100\text{ }\mu\text{m}$, in the range of the micropatterns in human tissues and organs [31]. hMSCs were chosen because of their

utility as self-renewal and multipotential cells to differentiate to various lineages, including adipocytes, chondrocytes and osteoblasts [208–212].

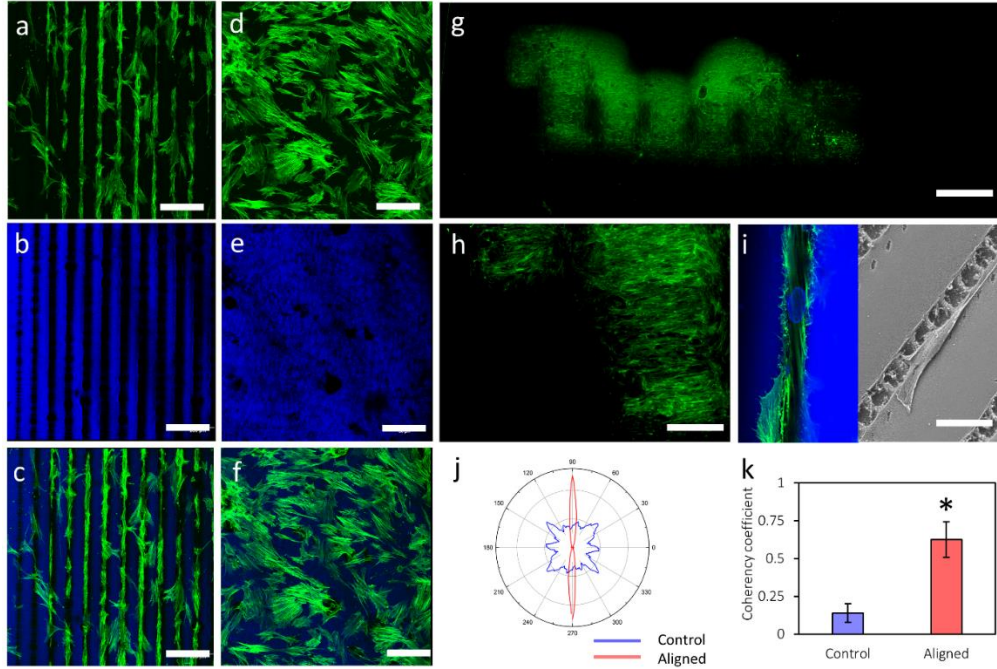


Figure 4-5. hMSC alignment on the biosilica micropatterned and control hydrogels. (a, b, c) hMSCs aligned to the biosilica micropatterns on the silk hydrogels; (d, e, f) hMSCs on the unpatterned control silk hydrogels demonstrated typical morphology. Confocal micrographs of hMSCs on the silk hydrogels stained for F-actin (green, a, d), counterstained for nuclei and silk (blue, b, e) and overlay images (c, f). (g) Fluorescence images of hMSCs stained for F-actin (green) on the micropatterned “Tufts” logo. (h) Partial enlargement of Figure (g). (i) Zoomed view (left) and SEM (right) of hMSCs on the biosilica micropatterns. (j) Graphical representation of cellular alignment quantified via ImageJ software and an OrientationJ plug-in. (k) Coherency coefficients indicating cellular distribution on the micropatterned and control hydrogels. Scale bars, a-f, 200 μm ; g, 2 mm; h, 700 μm ; i, 50 μm (left), 10 μm (right).

Aligned hMSCs are important in tissue regeneration as cell micropatterns result in highly organized tissue architectures (e.g., bone, cartilage, cornea) [35,213]. However, previous topographical micropatterning strategies often showed limited guidance of hMSC orientation on rigid substrates consisting of synthetic materials in relatively short culture periods[35]. In sharp contrast, striking cell alignment extending the width of the printed micropatterns (e.g., 1 mm) on the hydrogel substrates was observed after 4-days of cell culture, as shown in confocal micrographs of hMSCs on the silk hydrogels stained for F-actin (green) and counterstained for nuclei and silk (blue, **Figure 4-5a, b, c**) [214]. In comparison, cells randomly distributed on the unpatterned control hydrogels demonstrated typical cell morphology which remained the same over the culture period (**Figure 4-5d, e, f**).

Furthermore, after 14 days of culture on the micropatterned “Tufts” logo, fluorescence images of hMSCs stained for F-actin (green) showed that cells had fully covered the logo, aligned to the biosilica micropatterns on the logo, and formed a “Tufts” logo by themselves (**Figure 4-5g**). The fluorescent intensity of F-actin stained hMSCs on the micropatterns was about two-fold stronger than that of the surrounding silk control surface (**Figure 4-5h**), further evidence for specific cell attachment and alignment to the biosilica micropatterns.

Interestingly, the hMSCs appeared to favor the silica particles and showed specific attachment to the silica patterns. Confocal micrographs of the stained hMSCs showed that cell nuclei also aligned to the biosilica micropatterns (**Figure 4-5i**). SEM images provided further evidence that a single hMSC attached to and spread its actin filaments on the silica particles (**Figure 4-5i**, right). As a result, the F-actin of hMSCs aligned parallel with line spacing of 100 μm , following the printed micropatterns (**Figure 4-5c**). Quantification of cell alignment was performed on the confocal micrographs of the F-actin stained hMSCs

on the patterned and control silk hydrogels using ImageJ software equipped with a OrientationJ plug-in. Graphical representation of the cellular distribution showed that the hMSC filaments strongly oriented in the direction of the ellipse long axis, indicating significantly greater cellular alignment compared to controls (**Figure 4-5j**). The calculated coherency coefficient (a measure of how well the cells were aligned in the predominant direction) of the hMSCs on the micropatterns was 0.62, four times greater than that of the unpatterned controls (0.14, **Figure 4-5k**). These quantitative analyses further confirmed that cell orientation followed the peptide-silica micropatterns.

4.4.4 Protein alignment on mineral micropatterns

The efficacy of this design to micropattern protein on the silk hydrogels was demonstrated by fluorescence microscopy (**Figure 4-6**). Printing FITC-labeled BSA and R5 peptide followed by silicification resulted in FITC-BSA immobilized and aligned exclusively along the biosilica micropatterns (**Figure 4-6a**). Fluorescence microscopy confirmed that after 6 days of incubation in PBS, the FITC-BSA was mainly limited to the biosilica regions, with FITC-BSA stripes distinctive along the biosilica micropatterns (**Figure 4-6b**). Printing fluorescent-labeled BSA alone, followed by silicification, also resulted in FITC-BSA stripes (**Figure 4-6c**). However, after 6 days of incubation in PBS, the area covered by FITC-BSA extended over the hydrogel surface, with adjacent lines merged together (**Figure 4-6d**). The stability of the FITC-BSA/R5/silica micropatterns revealed spatial control of protein alignment using this design, probably due to BSA immobilization with the silica particles induced by the presence of the R5 peptide.

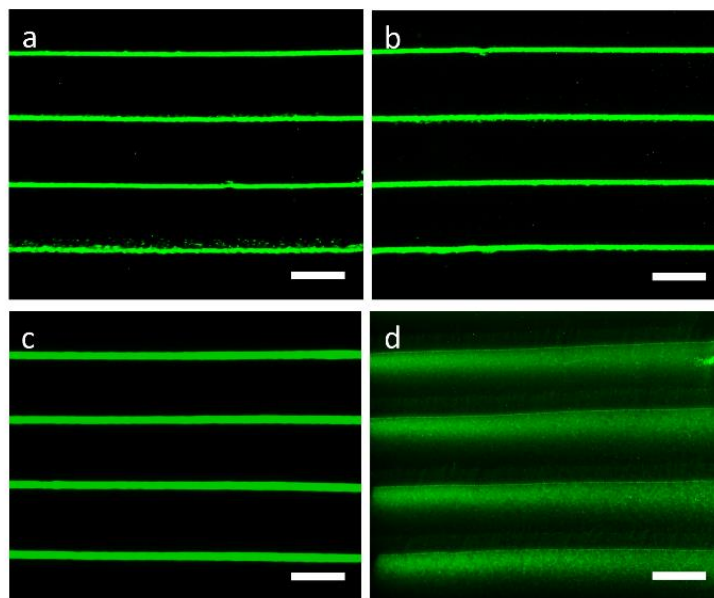


Figure 4-6. BSA alignment on the biosilica micropatterns. (a, b) Fluorescence microscopy images of micropatterns containing FITC-labeled BSA and R5 peptide followed by silicification; (c, d) fluorescence microscopy images of micropatterns containing FITC-labeled BSA alone followed by silicification. Fluorescence microscopy images of micropatterns in PBS at day 1 (a, c), day 6 (b, d). The distinctive FITC-BSA stripes in the FITC-BSA/R5/silica micropatterns reveal the spatial control of protein alignment using this design, in comparison to the extended distribution of the control FITC-BSA micropatterns. Scale bars: a, b, c, d, 400 μm .

4.5 Conclusion

A *de novo* strategy to design and synthesize bio-micropatterns for engineering cell alignment through the integration of aqueous-peptide inkjet printing and site-specific biomineralization was demonstrated. The resulting micropattern systems supported the alignment of hMSCs along and in micropattern directions and spaces. Aligned

micropattern cues are crucial for cell proliferation, migration and differentiation, and also result in the secretion and deposition of anisotropic extracellular matrix (ECM) specific to tissue types [31]. For example, the pattern cues in cartilage play an important role in building mechanical strength and tissue functions, where interterritorial fibers are aligned perpendicular to the joint surface in the middle zone, while being parallel in the superficial zone [215]. Given the highly ordered mineral and collagen orientation in bone and cartilage, this directed mineral micropattern is crucial in improving bone and cartilage formation *in vivo*. Thus, this study emphasized the role of mineral micropatterns in osteochondral tissue engineering as cells reciprocally interact with ECM to adapt to structures and topography in the local environment [216].

In addition, the micropatterns generated by inkjet printing of biosilicification domains on the biocompatible protein substrates under mild (peptide-mediated) conditions provide other potential applications. Inkjet printing of functional inks onto protein substrates offers opportunities to micropattern a variety of other substances, such as peptides, growth factors and biomacromolecules. Although inkjet printing has been used as a typical bioprinting approach to pattern protein and cells [201,217], this work further extends its application by introducing immobilization and alignment of functional substances in well organized silica particles on protein substrates. Surface modifications of the inert biosilica particles allow for controllable encapsulation and sustained release of a library of bioactive molecules and substances (e.g., proteins, enzymes, and drugs), which are sensitive to heat or caustic chemicals [218]. The micropatterned silk protein substrates offer biocompatibility, degradability and tunable mechanical properties to provide well organized three-dimensional extracellular microenvironments and extrinsic factor reservoirs for applications in tissue engineering and regenerative medicine [219–221]. For example, micropatterning of nerve growth factor (NGF) has potential for aligning Schwann cells in

neurons with applications towards nerve tissue regeneration [222]. A variety of polycationic peptides, e.g., silaffin and long chain polyamines which are able to precipitate silica nanospheres individually, can be printed on the silk substrates leading to functional material designs with different mineral morphologies [193]. Overall, this *de novo* design strategy for creating bio-micropatterns meets a broad range of needs in biomaterials and regenerative medicine involving interfacial tissue engineering, cell transplatation, cell-based sensors, and drug screening platforms [195,223], as well as providing a system with which to improve the understanding of fundamental of cellular functions [224].

5. Chapter 5. Overview and Future directions

5.1 Conclusions

In conclusion, this dissertation explored the feasibility of using silk as a template to combine selective mineralization domains with affinity to minerals to mimic the hierarchical architecture in biological systems from the molecular level to microscale and ultimately macroscale level. This bioinspired multiscale design of mineral assembly on polymeric templates offers a useful approach to develop complex heterogeneous organic/inorganic composites for a wide range of applications in tissue engineering and regenerative medicine, especially osteochondral tissue engineering.

5.2 Future directions and associated projects

5.2.1 Multiscale design and synthesis of biomimetic gradient protein/biosilica composites for osteochondral regeneration

The **goal** is to develop silk-based mineralized elastomers with spatial gradients of mineralization domains and transitional chemical, structural and mechanical properties to enhance osteochondral regeneration *in vivo*. We propose to: develop silk-based composites with the desirable features: structural (gradient pore size and porosity), biomechanical (controllable silk polymorphism and mineralization degree) and compositional (tunable silk and mineral contents) (Aim 1); investigate the effects of gradient systems on osteochondral coculture in vitro (Aim 2); evaluate the survival and function of the engineered gradient grafts in animal models for osteochondral tissue reconstruction (Aim 3). It is **hypothesized** that the gradient composite system will direct cells to form highly specialized osteochondral interface tissues with a capacity to survive and function in a rat model. The mechanics of the engineered grafts can be tuned through varying silk concentration and molecular weight as well as mineralization degree within the composites.

Other functional peptides and substances can be incorporated in this system to screen for optimal doses and combinations for osteochondral tissue development in a 3D environment.

Approaches

Osteochondral coculture. hMSCs will be seeded into the composites in osteochondral coculture medium *in vitro* over six weeks, followed by various assessments for outcomes: cell survival, proliferation and differentiation over time as a function of structure, orientation, and biomechanics. Procedures reported for human bone and cartilage tissue engineering will be used. Unsilicified plain silk scaffolds serve as controls.

Surgical implantation and histological evaluations. To better understand the immune response and implant integration, engineered scaffolds will be implanted subcutaneously in a rat model. The implantation of osteochondral grafts will be done with four experimental groups: (i) no treatment, (ii) scaffolds alone (without added cells), (iii) cell-seeded scaffolds (without culture), and (iv) tissue engineered grafts. Gradient composites will be explanted and examined histologically at different time points after implantation for osteochondral regeneration. Cell infiltration and degradation will be evaluated.

Biochemical analysis. DNA content will be quantified using the Picogreen assay. GAG content will be measured using a dimethylmethylene blue assay. Alkaline phosphatase activity will be determined at different time points and expressed as a measure of liberated p-nitrophenol concentration/ μg protein /min.

Statistical analysis. Paired or unpaired Student t-tests, as appropriate, will be used to determine statistical differences between groups. One-way ANOVA will be used when comparing features between groups. Two-way ANOVA will be used for comparing features between groups over time. Turkey's test will be used to determine which of the

means significantly differs for multiple comparisons. ANOVA will be performed when appropriate with P values less than 0.05. In all cases, $n > 3$ will be used for data sets.

Expected Outcomes

We anticipate that the silk-based gradient mineralization system will serve as 3D substrates for the formation of bone-/cartilage-like matrices with suitable mechanical properties for osteochondral tissue engineering and integrative cartilage repair. We also anticipate the complete integration of the implanted grafts with the surrounding tissues and rapid establishment of physiological architecture after implantation. The development of silk-based elastomers retains highly versatility while allowing for incorporation of other bioactive molecules in the fields of natural tissue engineering, drug delivery and enzyme immobilization.

Potential Problems and Alternatives

If we encountered difficulties with the formation of chondrogenic tissue matrix, we could try alternative approaches such as changing cell culture timing, sequential application of osteogenic and chondrogenic factors and/or the implementation of dynamic flow. Should the plan not meet the expected chondrogenic outcomes, gradients of growth factor can be considered given additional functionalization arises to control osteogenesis or chondrogenesis.

5.2.2 Coding cell micropatterns through peptide inkjet printing for arbitrary biomineralized architectures

The **goal** is to code and synthesize multifunctional biomineralized micropatterns with a capacity to engineer the alignment of various cells types and functionality to meet tissue-specific requirements including nerve tissues. We propose to: *encapsulate a library of*

bioactive molecules and substances (e.g., nerve growth factor (NGF)) in the silica particles to allow for sustained release of functional factors from arbitrary silica micropatterns (Aim 1); direct neural cell growth on functionalized silica micropatterns for neuron growth (Aim 2); investigate the efficiency of axonal alignment on flexible and implantable protein substrates in order to efficiently repair the injured sites of the nervous systems (Aim 3). It is **hypothesized** that the multifunctional mineralized micropatterns consisting of various bioactive factors will have broadened applications in tissue engineering and regenerative medicine including nerve tissue regeneration. Micropattern different polycationic peptides with mineralization domains will lead to micropatterned silica nanospheres with different mineral morphologies for functional material design.

5.2.3 3D printing silk-based calcium phosphate scaffolds

The **goal** is to design a simple, green and versatile process to directly write the assembly of silk protein and calcium phosphate nanoparticles and build up biomimetic ceramic-hard tissue parts for bone and osteochondral tissue engineering. We propose to: 3D print silk-calcium phosphate scaffolds with gradient structure and interconnecting porous network (Aim 1); incorporate functional biomolecules and substances in this system to screen for optimal doses and combinations in 3D environment and create patient-customized tissue engineered grafts (Aim 2); evaluate the cytocompatibility and osteoconductivity of 3D printed scaffolds in vitro for treatments of osteochondral defects and osteonecrosis (Aim 3). The biocompatible 3D printed silk-based scaffold can be used to promote vascularization and osteogenesis as a potential therapy for osteochondral defects and osteonecrosis.

Abstract

Natural composites often outperform synthetic materials for their superior mechanical properties due to the heterogeneous hierarchical architectures. Here we present a simple, green and versatile process to directly write assembly of silk protein and calcium phosphate nanoparticles and build up biomimetic ceramic-hard tissue parts for bone and osteochondral tissue engineering. 3D printing allows for precise control over the filament size and arrangement and ultimately the architecture of the 3D scaffolds. The resulting scaffolds will be assessed *in vitro* in terms of their degradability, mechanics, resolution and stability before and after sintering. Direct writing of protein/mineral inks offers a novel route to design elaborate reinforcement structures with a high level of customization in arbitrary geometries. This bioinspired design offers a useful approach to develop complex heterogeneous biocompatible composites with wide applications in tissue engineering and regenerative medicine.

Introduction

During osteochondral defects, ruptured cartilage damage penetrates subchondral bone area, leading to severe pain and morbidity. Current strategies show limitations in mechanical failure, controllable degradation, risk of corrosion, lack of continuous gradient interfaces with zonal cells and ECM organization [225]. Hence, suitable integration of biocompatible composite systems with a biomimetic gradient structure, environmental cues and mechanical properties are needed for osteochondral tissue regeneration.

The osteochondral interface presents a combination of gradients in cellularity, compositional, mechanical as well as structural gradients from subchondral bone to articular cartilage surface. The zonal cartilage region is mainly composed of 20% ECM, 80% water and 2% chondrocytes, which can be further separated into four regions: superficial articular, middle, deep and calcified cartilage zones [226]. The superficial zone

is composed of flattened chondrocytes and densely packed collagen fibrils (20 nm in diameter), tangentially arranged to the articular surface. Randomly oriented proteoglycans and extracellular matrix are predominant in the middle zone with more rounded chondrocytes. In the deep zone, thicker collagen type II fibers (120 nm diameter) highly occupied in this area. The subchondral bone provides support for the upper calcified cartilage layer. It has been shown that by mimicking the zonal organization within cartilage tissue, the local cell environment will stimulate synthesis of an organized cartilage construction [227]. Therefore, 3D printing scaffolds with a structural gradient can be an appealing strategy for osteochondral tissue engineering. Moreover, bone presents a radial gradient structure from the outside to the inner center. The outside cortical bone is more compact with a porosity ranging from 5% to 10%, while the inner cancellous bone is more porous with a porosity ranging from 50% to 90% [228,229]. Thus, 3D printed scaffolds with a built-in gradient structure can be used to mimic the radial bone architecture for bone tissue engineering.

Rationale and material design

3D printing of silk-calcium phosphate scaffolds. To produce silk-calcium phosphate ink for 3D printing, calcium phosphate particles (~200 nm) were dispersed in deionized water to obtain a suspension with desired density of mineral particles. Silk solution (30%) was mixed with the calcium phosphate suspension to produce a silk-mineral paste. During the printing process, a moving nozzle (x- and y-axis) extruded silk-mineral filaments which solidified once deposited on the printer platform. Successive layers were built upon each other through changing the z-axis control of the nozzle.

Scaffold design. Silk-based scaffolds with desired structural and biomechanical anisotropy were created through introducing the micro-scale interconnected pores/channels. The

resulting scaffolds were aimed to match the biomechanical anisotropy of osteochondral interface. 3D printed silk scaffolds will obtain four distinct levels of porosity with seamless interconnectivity to mimic the structure of (1) articular cartilage, (2) hypertrophic chondrocytes, (3) mineralizing chondrocytes and (4) subchondral bone. Mechanical properties can be tuned by varying pore size, porosity and calcium phosphate components. The combination of structural and compositional gradients will be used to stimulate desirable cues and enhance osteochondral tissue regeneration. The resulting silk-based scaffolds will be assessed for topography and mechanical properties with optimal mechanical properties, physiological shape, functionality and machinability.

Expected outcomes

The 3D printed silk-based scaffolds with structural and biomechanical anisotropy could serve as promising substrates to enhance osteogenesis and angiogenesis *in vitro* and *in vivo*.

Preliminary results and discussion

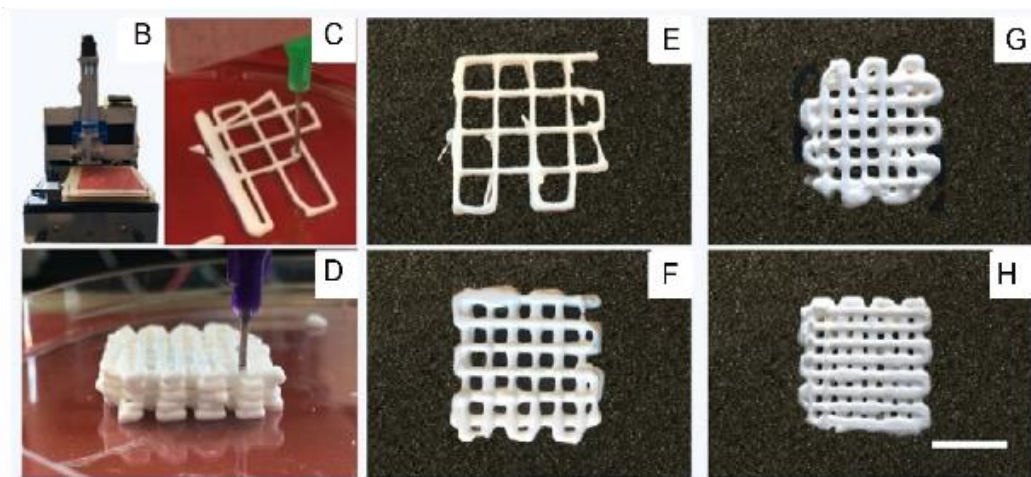
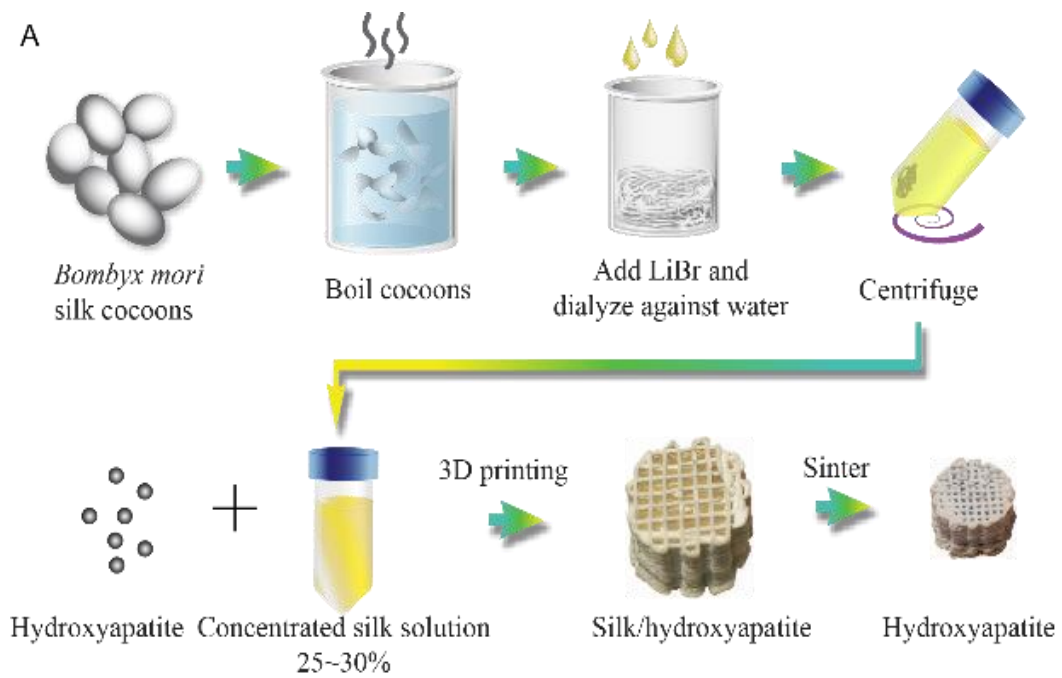


Figure 5-1. (A) Schematic of 3D printing silk-calcium phosphate scaffolds. (B) Photograph of 3D printer. (C, D) Photographs of 3D printing process of silk-mineral ink. (E, F, G, H) Photographs of 3D printed silk-calcium phosphate scaffolds with different pore sizes and patterns. Scale bar: 1 cm.

3D printed silk-mineral scaffolds with desired dimensions and patterns were achieved by adjusting the extrusion path of printing head, the size of each layer and the number of layers. Micro-sized interconnected pores/channels were uniformly distributed in the silk scaffolds to allow for cell ingrowth and vascularization (**Figure 5-1**).



Figure 5-2. Schematic representation of ink formation and extrusion.

The ink for 3D printing was formulated with the mixture of calcium phosphate powder, silk and DI water. **Figure 5-2** demonstrates the ink preparation process, during which calcium phosphate particles (~200 nm) were dispersed in deionized water to obtain a suspension with desired density of minerals. Silk solution (30%) was then mixed with the mineral suspension to produce a silk-mineral paste.

We investigated formulation of different mineral/silk/water ratio to optimize the filament extrusion process in **Figure 5-3**. The final formulation contains 50% calcium phosphate, 42% water and 8% silk protein to allow for smooth extrusion of filaments during printing.

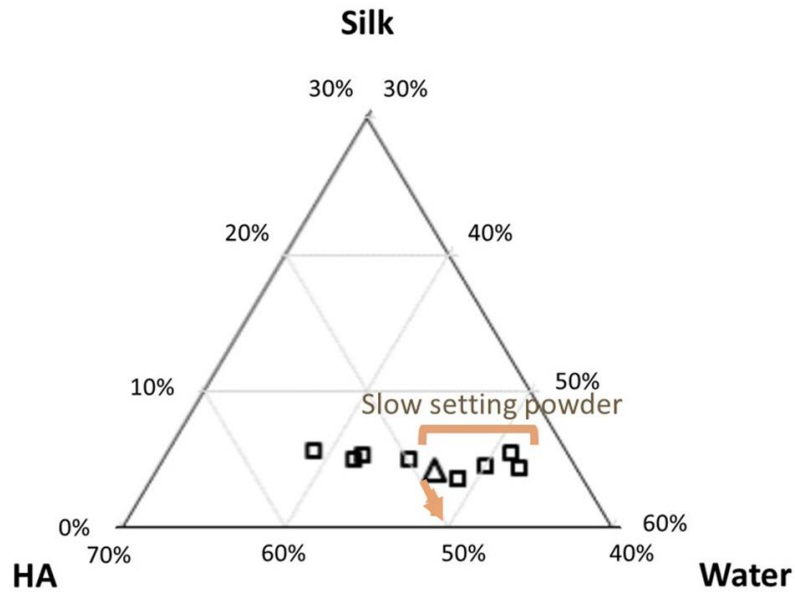


Figure 5-3. Phase diagram of ink formulation with respect to silk, calcium phosphate and water.

Based on this formulation, direct-write assembly of silk-mineral inks resulted in 3D scaffolds with an interpenetrating network of varied pore sizes. Well-organized channels with uniform width evenly distributed in the scaffolds. The pore sizes ranged from 200 nm to 1mm. **Figure 5-4** reveals the interconnected pores in the 3D printed scaffolds, and filaments with smooth surface under SEM images.

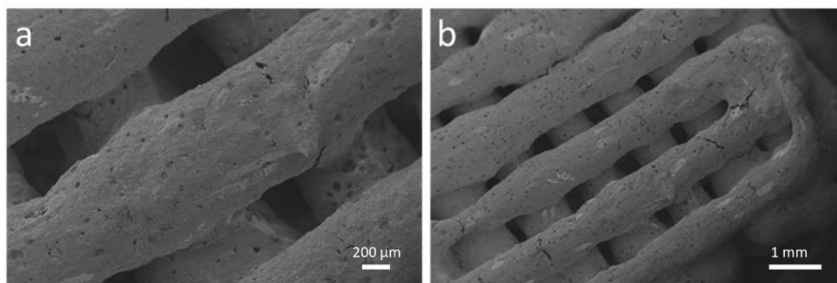


Figure 5-4. SEM images of printed silk/mineral filaments intersecting between filament layers.

Upon sintering at 1080 °C in air, the structure of the 3D printed silk/mineral scaffold was maintained (**Figure 5-5**). The silk molecules were decomposed and oxidized at high temperature, and the scaffolds exhibited a weight loss of 25% after sintering. As shown in the optical images of the scaffolds before and after sintering, the size of the scaffold decreased after sintering (20% in x dimension), which was probably due to the shrinkage of pores and voids during heating.



Figure 5-5. Optical images of the silk/calcium phosphate scaffold before and after sintering.

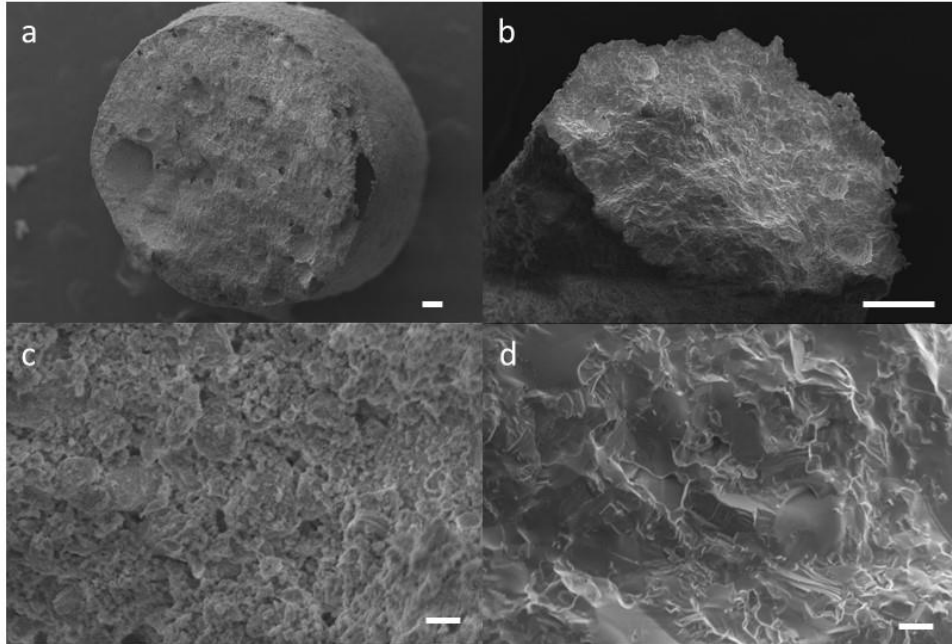


Figure 5-6. SEM images of silk/mineral scaffold (a, c) before sintering and (b, d) after sintering. (c, d), higher magnification view of the silk/mineral filament surface. Scale bars: a, b, 100 μm ; c, d, 4 μm .

The cross-sectional SEM images of the filaments within the scaffolds are shown in **Figure 5-6**. The cross-section of filaments before sintering consists bonded sub- μm size granules, implying a high degree of roughness. A few sub- μm size pores were observed within the filaments as well. After sintering, the microparticles on the surface was not observed, probably owing to the crystallization of calcium phosphate particles during heating.

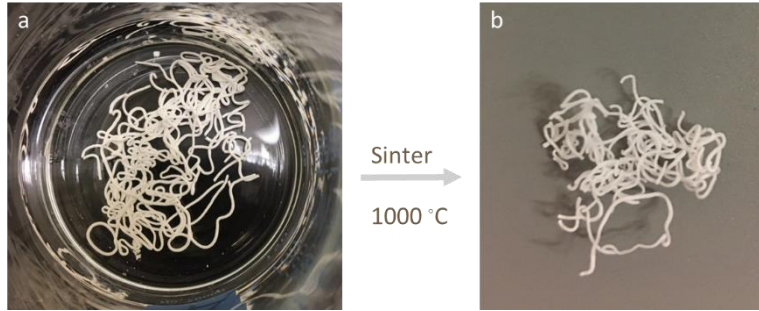


Figure 5-7. Wet spinning of silk/mineral filaments. (a) Optical image of silk/mineral fibers prepared by wet spinning in methanol bath. (b) Optical image of the fibers after sintering at 1000 °C in air.

Mineralized silk fibers were wet spun into methanol bath through extrusion based on the aforementioned silk/calcium phosphate/water ink. The fibers of around 1 mm diameter were spun in methanol. After treatments in methanol to dehydrate the fiber and induce beta sheet formation in silk, the fiber maintained its original shape. The shape of the fiber was preserved even after sintering at 1000 °C in air for four hours. This wet spinning strategy to create mineralized silk fibers can be used to create functional composites with high mechanical performance with applications in biomedicine.

Future directions

The rheological properties of the protein/mineral inks will be investigated to create an ink catalog for processing. Future work includes mechanical evaluation of 3D printed silk-calcium phosphate scaffolds. Silk nano-/micro-fibers can be incorporated into the silk-mineral paste during ink preparation to strengthen the mechanical properties of the 3D printed scaffolds. *In vitro* scaffold evaluations will be conducted to demonstrate cytocompatibility. Once the anisotropic scaffolds with networks of channels/pores are

finalized to meet the mechanical requirements of osteochondral grafts, support for osteogenesis and chondrogenesis will be assessed in the 3D printed scaffolds *in vitro*.

References:

- [1] A.G. Mikos, S.W. Herring, P. Ochareon, J. Elisseeff, H.H. Lu, R. Kandel, F.J. Schoen, M. Toner, D. Mooney, A. Atala, M.E. Van Dyke, D. Kaplan, G. Vunjak-Novakovic, Engineering complex tissues., *Tissue Eng.* 12 (2006) 3307–39. doi:10.1089/ten.2006.12.3307.
- [2] M. Singh, C. Berkland, M.S. Detamore, Strategies and applications for incorporating physical and chemical signal gradients in tissue engineering., *Tissue Eng. Part B. Rev.* 14 (2008) 341–66. doi:10.1089/ten.teb.2008.0304.
- [3] R.M. Schinagl, D. Gurskis, A.C. Chen, R.L. Sah, Depth-dependent confined compression modulus of full-thickness bovine articular cartilage., *J. Orthop. Res.* 15 (1997) 499–506. doi:10.1002/jor.1100150404.
- [4] A. Di Luca, C. Van Blitterswijk, L. Moroni, The osteochondral interface as a gradient tissue: from development to the fabrication of gradient scaffolds for regenerative medicine., *Birth Defects Res. C. Embryo Today.* 105 (2015) 34–52. doi:10.1002/bdrc.21092.
- [5] C.N. van Dijk, M.L. Reilingh, M. Zengerink, C.J.A. van Bergen, Osteochondral defects in the ankle: why painful?, *Knee Surgery, Sport. Traumatol. Arthrosc.* 18 (2010) 570–580. doi:10.1007/s00167-010-1064-x.
- [6] A. Tampieri, S. Sprio, M. Sandri, F. Valentini, Mimicking natural bio-mineralization processes: A new tool for osteochondral scaffold development, *Trends Biotechnol.* 29 (2011) 526–535. doi:10.1016/j.tibtech.2011.04.011.
- [7] K. Shimomura, Y. Moriguchi, C.D. Murawski, H. Yoshikawa, N. Nakamura, Osteochondral tissue engineering with biphasic scaffold: current strategies and

techniques., *Tissue Eng. Part B. Rev.* 20 (2014) 468–76.

doi:10.1089/ten.TEB.2013.0543.

- [8] R.M. Schek, J.M. Taboas, S.J. Segvich, S.J. Hollister, P.H. Krebsbach, Engineered osteochondral grafts using biphasic composite solid free-form fabricated scaffolds., *Tissue Eng.* 10 (n.d.) 1376–85.
doi:10.1089/ten.2004.10.1376.
- [9] J.J. Li, K. Kim, S.-I. Roohani-Esfahani, J. Guo, D.L. Kaplan, H. Zreiqat, A biphasic scaffold based on silk and bioactive ceramic with stratified properties for osteochondral tissue regeneration., *J. Mater. Chem. B. Mater. Biol. Med.* 3 (2015) 5361–5376. doi:10.1039/C5TB00353A.
- [10] H. Da, S.-J. Jia, G.-L. Meng, J.-H. Cheng, W. Zhou, Z. Xiong, Y.-J. Mu, J. Liu, The Impact of Compact Layer in Biphasic Scaffold on Osteochondral Tissue Engineering, *PLoS One.* 8 (2013) e54838. doi:10.1371/journal.pone.0054838.
- [11] W.L. Grayson, S. Bhumiratana, P.H. Grace Chao, C.T. Hung, G. Vunjak-Novakovic, Spatial regulation of human mesenchymal stem cell differentiation in engineered osteochondral constructs: effects of pre-differentiation, soluble factors and medium perfusion., *Osteoarthr. Cartil.* 18 (2010) 714–23.
doi:10.1016/j.joca.2010.01.008.
- [12] T.J. Levingstone, A. Matsiko, G.R. Dickson, F.J. O’Brien, J.P. Gleeson, A biomimetic multi-layered collagen-based scaffold for osteochondral repair., *Acta Biomater.* 10 (2014) 1996–2004. doi:10.1016/j.actbio.2014.01.005.
- [13] J.E. Jeon, C. Vaquette, T.J. Klein, D.W. Hutmacher, Perspectives in multiphasic osteochondral tissue engineering., *Anat. Rec. (Hoboken).* 297 (2014) 26–35.

doi:10.1002/ar.22795.

- [14] H.M. Aydin, A Three-Layered Osteochondral Plug: Structural, Mechanical, and in vitro Biocompatibility Analysis, *Adv. Eng. Mater.* 13 (2011) B511–B517.
doi:10.1002/adem.201180005.
- [15] P. Nooeaid, J.A. Roether, E. Weber, D.W. Schubert, A.R. Boccaccini, Technologies for Multilayered Scaffolds Suitable for Interface Tissue Engineering, *Adv. Eng. Mater.* 16 (2014) 319–327. doi:10.1002/adem.201300072.
- [16] X. Wang, E. Wenk, X. Zhang, L. Meinel, G. Vunjak-Novakovic, D.L. Kaplan, Growth factor gradients via microsphere delivery in biopolymer scaffolds for osteochondral tissue engineering., *J. Control. Release.* 134 (2009) 81–90.
doi:10.1016/j.jconrel.2008.10.021.
- [17] N. Mohan, N.H. Dormer, K.L. Caldwell, V.H. Key, C.J. Berkland, M.S. Detamore, Continuous gradients of material composition and growth factors for effective regeneration of the osteochondral interface., *Tissue Eng. Part A.* 17 (2011) 2845–55. doi:10.1089/ten.tea.2011.0135.
- [18] T.B.F. Woodfield, J. Malda, J. de Wijn, F. Péters, J. Riesle, C.A. van Blitterswijk, Design of porous scaffolds for cartilage tissue engineering using a three-dimensional fiber-deposition technique., *Biomaterials.* 25 (2004) 4149–61.
doi:10.1016/j.biomaterials.2003.10.056.
- [19] H.I. Roach, Why does bone matrix contain non-collagenous proteins? The possible roles of osteocalcin, osteonectin, osteopontin and bone sialoprotein in bone mineralisation and resorption., *Cell Biol. Int.* 18 (1994) 617–28.
doi:10.1006/cbir.1994.1088.

- [20] N.T. Khanarian, N.M. Haney, R.A. Burga, H.H. Lu, A functional agarose-hydroxyapatite scaffold for osteochondral interface regeneration, *Biomaterials*. 33 (2012) 5247–5258. doi:10.1016/j.biomaterials.2012.03.076.
- [21] J.M. Oliveira, M.T. Rodrigues, S.S. Silva, P.B. Malafaya, M.E. Gomes, C.A. Viegas, I.R. Dias, J.T. Azevedo, J.F. Mano, R.L. Reis, Novel hydroxyapatite/chitosan bilayered scaffold for osteochondral tissue-engineering applications: Scaffold design and its performance when seeded with goat bone marrow stromal cells, *Biomaterials*. 27 (2006) 6123–6137. doi:10.1016/j.biomaterials.2006.07.034.
- [22] S. Bhumiratana, W.L. Grayson, A. Castaneda, D.N. Rockwood, E.S. Gil, D.L. Kaplan, G. Vunjak-Novakovic, Nucleation and growth of mineralized bone matrix on silk-hydroxyapatite composite scaffolds, *Biomaterials*. 32 (2011) 2812–2820. doi:10.1016/j.biomaterials.2010.12.058.
- [23] S. V. Dorozhkin, M. Epple, Biological and Medical Significance of Calcium Phosphates, *Angew. Chemie Int. Ed.* 41 (2002) 3130–3146. doi:10.1002/1521-3773(20020902)41:17<3130::AID-ANIE3130>3.0.CO;2-1.
- [24] Q. Zhang, Dissolution and mineralization behaviors of HA coatings, *Biomaterials*. 24 (2003) 4741–4748. doi:10.1016/S0142-9612(03)00371-5.
- [25] A. Tampieri, M. Sandri, E. Landi, D. Pressato, S. Francioli, R. Quarto, I. Martin, Design of graded biomimetic osteochondral composite scaffolds, *Biomaterials*. 29 (2008) 3539–3546. doi:10.1016/j.biomaterials.2008.05.008.
- [26] E. Beniash, *Biomaterials-hierarchical nanocomposites: the example of bone*, Wiley Interdiscip. Rev. Nanomedicine Nanobiotechnology. 3 (2011) 47–69.

doi:10.1002/wnan.105.

- [27] P.J. Yang, J.S. Temenoff, Engineering orthopedic tissue interfaces., *Tissue Eng. Part B. Rev.* 15 (2009) 127–41. doi:10.1089/ten.teb.2008.0371.
- [28] C.E. Hamm, R. Merkel, O. Springer, P. Jurkojc, C. Maier, K. Prechtel, V. Smetacek, Architecture and material properties of diatom shells provide effective mechanical protection, *Nature.* 421 (2003) 841–843. doi:10.1038/nature01416.
- [29] U.G.K. Wegst, H. Bai, E. Saiz, A.P. Tomsia, R.O. Ritchie, Bioinspired structural materials, *Nat. Mater.* 14 (2014) 23–36. doi:10.1038/nmat4089.
- [30] M.A. Meyers, P.-Y. Chen, A.Y.-M. Lin, Y. Seki, Biological materials: Structure and mechanical properties, *Prog. Mater. Sci.* 53 (2008) 1–206.
doi:10.1016/j.pmatsci.2007.05.002.
- [31] M. Thery, Micropatterning as a tool to decipher cell morphogenesis and functions, *J. Cell Sci.* 123 (2010) 4201–4213. doi:10.1242/jcs.075150.
- [32] P.-Y. Chen, A.Y.-M. Lin, J. McKittrick, M.A. Meyers, Structure and mechanical properties of crab exoskeletons, *Acta Biomater.* 4 (2008) 587–596.
doi:10.1016/j.actbio.2007.12.010.
- [33] R. Gordon, D. Losic, M.A. Tiffany, S.S. Nagy, F.A.S. Sterrenburg, The Glass Menagerie: diatoms for novel applications in nanotechnology, *Trends Biotechnol.* 27 (2009) 116–127. doi:10.1016/j.tibtech.2008.11.003.
- [34] J. Noyes, M. Sumper, P. Vukusic, Light manipulation in a marine diatom, *J. Mater. Res.* 23 (2008) 3229–3235. doi:10.1557/JMR.2008.0381.

- [35] Y. Li, G. Huang, X. Zhang, L. Wang, Y. Du, T.J. Lu, F. Xu, Engineering cell alignment in vitro, *Biotechnol. Adv.* 32 (2014) 347–365.
doi:10.1016/j.biotechadv.2013.11.007.
- [36] D.H. ELLIOTT, STRUCTURE AND FUNCTION OF MAMMALIAN TENDON., *Biol. Rev. Camb. Philos. Soc.* 40 (1965) 392–421.
<http://www.ncbi.nlm.nih.gov/pubmed/14340913>.
- [37] J.S. Temenoff, A.G. Mikos, Review: tissue engineering for regeneration of articular cartilage., *Biomaterials.* 21 (2000) 431–40.
<http://www.ncbi.nlm.nih.gov/pubmed/10674807> (accessed November 7, 2016).
- [38] S. Weiner, W. Traub, Bone structure: from angstroms to microns., *FASEB J.* 6 (1992) 879–85. <http://www.ncbi.nlm.nih.gov/pubmed/1740237>.
- [39] D. Otzen, The Role of Proteins in Biosilicification, *Scientifica (Cairo)*. 2012 (2012) 1–22. doi:10.6064/2012/867562.
- [40] S. Alom Ruiz, C.S. Chen, Microcontact printing: A tool to pattern, *Soft Matter.* 3 (2007) 168–177. doi:10.1039/B613349E.
- [41] C. Tamerler, M. Sarikaya, Molecular biomimetics: nanotechnology and bionanotechnology using genetically engineered peptides, *Philos. Trans. R. Soc. A Math. Phys. Eng. Sci.* 367 (2009) 1705–1726. doi:10.1098/rsta.2009.0018.
- [42] L.L. Hench, J. Wilson, Surface-active biomaterials., *Science.* 226 (1984) 630–6.
<http://www.ncbi.nlm.nih.gov/pubmed/6093253>.
- [43] M. Cerruti, N. Sahai, Silicate Biomaterials for Orthopaedic and Dental Implants, *Rev. Mineral. Geochemistry.* 64 (2006) 283–313. doi:10.2138/rmg.2006.64.9.

- [44] T. Lebold, C. Jung, J. Michaelis, C. Bräuchle, Nanostructured Silica Materials As Drug-Delivery Systems for Doxorubicin: Single Molecule and Cellular Studies, *Nano Lett.* 9 (2009) 2877–2883. doi:10.1021/nl9011112.
- [45] H.C. Schröder, X. Wang, U. Schloßmacher, M. Wiens, W.E.G. Müller, Biogenic Inorganic Polysilicates (Biosilica): Formation and Biomedical Applications, in: 2013: pp. 197–234. doi:10.1007/978-3-642-41004-8_8.
- [46] M. Falah, G. Nierenberg, M. Soudry, M. Hayden, G. Volpin, Treatment of articular cartilage lesions of the knee., *Int. Orthop.* 34 (2010) 621–30. doi:10.1007/s00264-010-0959-y.
- [47] M. Singh, C. Berkland, M.S. Detamore, Strategies and applications for incorporating physical and chemical signal gradients in tissue engineering., *Tissue Eng. Part B. Rev.* 14 (2008) 341–66. doi:10.1089/ten.teb.2008.0304.
- [48] J.A. Buckwalter, H.J. Mankin, Articular cartilage: tissue design and chondrocyte-matrix interactions., *Instr. Course Lect.* 47 (1998) 477–86. <http://www.ncbi.nlm.nih.gov/pubmed/9571449>.
- [49] A.M. Bhosale, J.B. Richardson, Articular cartilage: structure, injuries and review of management, *Br. Med. Bull.* 87 (2008) 77–95. doi:10.1093/bmb/ldn025.
- [50] B.A. Harley, A.K. Lynn, Z. Wissner-Gross, W. Bonfield, I. V Yannas, L.J. Gibson, Design of a multiphase osteochondral scaffold III: Fabrication of layered scaffolds with continuous interfaces., *J. Biomed. Mater. Res. A.* 92 (2010) 1078–93. doi:10.1002/jbm.a.32387.
- [51] I. Zizak, P. Roschger, O. Paris, B.. Misof, A. Berzlanovich, S. Bernstorff, H.

- Amenitsch, K. Klaushofer, P. Fratzl, Characteristics of mineral particles in the human bone/cartilage interface, *J. Struct. Biol.* 141 (2003) 208–217.
doi:10.1016/S1047-8477(02)00635-4.
- [52] S. Thomopoulos, G.R. Williams, J.A. Gimbel, M. Favata, L.J. Soslowsky, Variation of biomechanical, structural, and compositional properties along the tendon to bone insertion site, *J. Orthop. Res.* 21 (2003) 413–419.
doi:10.1016/S0736-0266(03)0057-3.
- [53] S.L.-Y. Woo, S.D. Abramowitch, R. Kilger, R. Liang, Biomechanics of knee ligaments: injury, healing, and repair., *J. Biomech.* 39 (2006) 1–20.
doi:10.1016/j.jbiomech.2004.10.025.
- [54] S. Sant, M.J. Hancock, J.P. Donnelly, D. Iyer, A. Khademhosseini, BIOMIMETIC GRADIENT HYDROGELS FOR TISSUE ENGINEERING., *Can. J. Chem. Eng.* 88 (2010) 899–911. doi:10.1002/cjce.20411.
- [55] E.B. Hunziker, Articular cartilage repair: basic science and clinical progress. A review of the current status and prospects., *Osteoarthr. Cartil.* 10 (2002) 432–63.
doi:10.1053/joca.2002.0801.
- [56] W. Swieszkowski, B.H.S. Tuan, K.J. Kurzydowski, D.W. Hutmacher, Repair and regeneration of osteochondral defects in the articular joints., *Biomol. Eng.* 24 (2007) 489–95. doi:10.1016/j.bioeng.2007.07.014.
- [57] D. Schaefer, I. Martin, G. Jundt, J. Seidel, M. Heberer, A. Grodzinsky, I. Bergin, G. Vunjak-Novakovic, L.E. Freed, Tissue-engineered composites for the repair of large osteochondral defects., *Arthritis Rheum.* 46 (2002) 2524–34.
doi:10.1002/art.10493.

- [58] K.E.M. Benders, P.R. van Weeren, S.F. Badylak, D.B.F. Saris, W.J.A. Dhert, J. Malda, Extracellular matrix scaffolds for cartilage and bone regeneration., *Trends Biotechnol.* 31 (2013) 169–76. doi:10.1016/j.tibtech.2012.12.004.
- [59] S.H. Oh, T.H. Kim, J.H. Lee, Creating growth factor gradients in three dimensional porous matrix by centrifugation and surface immobilization., *Biomaterials.* 32 (2011) 8254–60. doi:10.1016/j.biomaterials.2011.07.027.
- [60] M.J. Wakelam, The fusion of myoblasts, *Biochem. J.* 228 (1985) 1–12.
- [61] J.S. Choi, S.J. Lee, G.J. Christ, A. Atala, J.J. Yoo, The influence of electrospun aligned poly(ϵ -caprolactone)/collagen nanofiber meshes on the formation of self-aligned skeletal muscle myotubes, *Biomaterials.* 29 (2008) 2899–2906. doi:10.1016/j.biomaterials.2008.03.031.
- [62] V.T. Ribeiro-Resende, B. Koenig, S. Nichterwitz, S. Oberhoffner, B. Schlosshauer, Strategies for inducing the formation of bands of Büngner in peripheral nerve regeneration, *Biomaterials.* 30 (2009) 5251–5259. doi:10.1016/j.biomaterials.2009.07.007.
- [63] G.A. Brook, D. Plate, R. Franzen, D. Martin, G. Moonen, J. Schoenen, A.B. Schmitt, J. Noth, W. Nacimiento, Spontaneous longitudinally orientated axonal regeneration is associated with the Schwann cell framework within the lesion site following spinal cord compression injury of the rat., *J. Neurosci. Res.* 53 (1998) 51–65. doi:10.1002/(SICI)1097-4547(19980701)53:1<51::AID-JNR6>3.0.CO;2-I.
- [64] V. Guénard, N. Kleitman, T.K. Morrissey, R.P. Bunge, P. Aebischer, Syngeneic Schwann cells derived from adult nerves seeded in semipermeable guidance channels enhance peripheral nerve regeneration., *J. Neurosci.* 12 (1992) 3310–20.

<http://www.ncbi.nlm.nih.gov/pubmed/1527582>.

- [65] N. Poulsen, M. Sumper, N. Kroger, Biosilica formation in diatoms: Characterization of native silaffin-2 and its role in silica morphogenesis, *Proc. Natl. Acad. Sci.* 100 (2003) 12075–12080. doi:10.1073/pnas.2035131100.
- [66] M. Sumper, A Phase Separation Model for the Nanopatterning of Diatom Biosilica, *Science* (80-.). 295 (2002) 2430–2433. doi:10.1126/science.1070026.
- [67] R. JUGDAOHSINGH, SILICON AND BONE HEALTH, *J Nutr Heal. Aging.* 11 (2007) 99–110.
- [68] S. Sripanyakorn, R. Jugdaohsingh, W. Dissayabutr, S.H.C. Anderson, R.P.H. Thompson, J.J. Powell, The comparative absorption of silicon from different foods and food supplements., *Br. J. Nutr.* 102 (2009) 825–34. doi:10.1017/S0007114509311757.
- [69] M. Bosetti, M. Cannas, The effect of bioactive glasses on bone marrow stromal cells differentiation., *Biomaterials.* 26 (2005) 3873–9. doi:10.1016/j.biomaterials.2004.09.059.
- [70] W. Tan, K. Wang, X. He, X.J. Zhao, T. Drake, L. Wang, R.P. Bagwe, Bionanotechnology based on silica nanoparticles., *Med. Res. Rev.* 24 (2004) 621–38. doi:10.1002/med.20003.
- [71] X. Wang, H.C. Schröder, M. Wiens, H. Ushijima, W.E.G. Müller, Bio-silica and bio-polyphosphate: applications in biomedicine (bone formation)., *Curr. Opin. Biotechnol.* 23 (2012) 570–8. doi:10.1016/j.copbio.2012.01.018.
- [72] A.J. Mieszawska, N. Fourligas, I. Georgakoudi, N.M. Ouhib, D.J. Belton, C.C.

- Perry, D.L. Kaplan, Osteoinductive silk-silica composite biomaterials for bone regeneration., *Biomaterials*. 31 (2010) 8902–10.
doi:10.1016/j.biomaterials.2010.07.109.
- [73] C. Wong Po Foo, S. V Patwardhan, D.J. Belton, B. Kitchel, D. Anastasiades, J. Huang, R.R. Naik, C.C. Perry, D.L. Kaplan, Novel nanocomposites from spider silk-silica fusion (chimeric) proteins., *Proc. Natl. Acad. Sci. U. S. A.* 103 (2006) 9428–33. doi:10.1073/pnas.0601096103.
- [74] S. Mann, Biomineralization and biomimetic materials chemistry, *J. Mater. Chem.* 5 (1995) 935. doi:10.1039/jm9950500935.
- [75] J.W.C. Dunlop, P. Fratzl, Biological Composites, *Annu. Rev. Mater. Res.* 40 (2010) 1–24. doi:10.1146/annurev-matsci-070909-104421.
- [76] J. Aizenberg, P. Fratzl, Biological and Biomimetic Materials, *Adv. Mater.* 21 (2009) 387–388. doi:10.1002/adma.200803699.
- [77] J.F.V. Vincent, Biomimetic materials, *J. Mater. Res.* 23 (2008) 3140–3147. doi:10.1557/JMR.2008.0380.
- [78] U.G.K. Wegst, M.F. Ashby, The mechanical efficiency of natural materials, *Philos. Mag.* 84 (2004) 2167–2186. doi:10.1080/14786430410001680935.
- [79] L. Li, C. Ortiz, Pervasive nanoscale deformation twinning as a catalyst for efficient energy dissipation in a bioceramic armour, *Nat. Mater.* 13 (2014) 501–507. doi:10.1038/nmat3920.
- [80] C. Li, D.L. Kaplan, Biomimetic composites via molecular scale self-assembly and biomineralization, *Curr. Opin. Solid State Mater. Sci.* 7 (2003) 265–271.

doi:10.1016/j.cossms.2003.09.011.

- [81] S. Mann, Molecular tectonics in biomineralization and biomimetic materials chemistry, *Nature*. 365 (1993) 499–505. doi:10.1038/365499a0.
- [82] S.R. Letellier, M.J. Lochhead, A.A. Campbell, V. Vogel, Oriented growth of calcium oxalate monohydrate crystals beneath phospholipid monolayers., *Biochim. Biophys. Acta*. 1380 (1998) 31–45.
<http://www.ncbi.nlm.nih.gov/pubmed/9545525>.
- [83] S. Mann, Molecular recognition in biomineralization, *Nature*. 332 (1988) 119–124. doi:10.1038/332119a0.
- [84] S. Mann, B.R. Heywood, S. Rajam, J.D. Birchall, Controlled crystallization of CaCO₃ under stearic acid monolayers, *Nature*. 334 (1988) 692–695.
doi:10.1038/334692a0.
- [85] J. Woodlouse, Nanoparticles biomineralization, *Online Nanotechnologies J*. 2 (2001) 1–3.
- [86] G. Xu, N. Yao, I.A. Aksay, J.T. Groves, Biomimetic Synthesis of Macroscopic-Scale Calcium Carbonate Thin Films. Evidence for a Multistep Assembly Process, *J. Am. Chem. Soc.* 120 (1998) 11977–11985. doi:10.1021/ja9819108.
- [87] N. Kröger, R. Deutzmann, M. Sumper, Silica-precipitating peptides from diatoms. The chemical structure of silaffin-A from *Cylindrotheca fusiformis*., *J. Biol. Chem.* 276 (2001) 26066–70. doi:10.1074/jbc.M102093200.
- [88] N. Kröger, R. Deutzmann, M. Sumper, Polycationic Peptides from Diatom Biosilica That Direct Silica Nanosphere Formation, *Science* (80-.). 286 (1999)

1129–1132. doi:10.1126/science.286.5442.1129.

- [89] D.H. Nam, K. Won, Y.H. Kim, B.I. Sang, A novel route for immobilization of proteins to silica particles incorporating silaffin domains., *Biotechnol. Prog.* 25 (2009) 1643–9. doi:10.1002/btpr.261.
- [90] W.E.G. Müller, X. Wang, F.-Z. Cui, K.P. Jochum, W. Tremel, J. Bill, H.C. Schröder, F. Natalio, U. Schloßmacher, M. Wiens, Sponge spicules as blueprints for the biofabrication of inorganic–organic composites and biomaterials, *Appl. Microbiol. Biotechnol.* 83 (2009) 397–413. doi:10.1007/s00253-009-2014-8.
- [91] X. Wang, M. Wiens, H.C. Schröder, S. Hu, E. Mugnaioli, U. Kolb, W. Tremel, D. Pisignano, W.E.G. Müller, Morphology of Sponge Spicules: Silicatein a Structural Protein for Bio-Silica Formation, *Adv. Eng. Mater.* 12 (2010) B422–B437. doi:10.1002/adem.200980042.
- [92] M. Dion, H. Rydberg, E. Schröder, D.C. Langreth, B.I. Lundqvist, Van der Waals density functional for general geometries, *Phys. Rev. Lett.* 92 (2004) 246401. doi:10.1103/PhysRevLett.92.246401.
- [93] H.C. Schröder, A. Boreiko, M. Korzhev, M.N. Tahir, W. Tremel, C. Eckert, H. Ushijima, I.M. Müller, W.E.G. Müller, Co-expression and Functional Interaction of Silicatein with Galectin, *J. Biol. Chem.* 281 (2006) 12001–12009. doi:10.1074/jbc.M512677200.
- [94] M. Sumper, E. Brunner, Learning from Diatoms: Nature’s Tools for the Production of Nanostructured Silica, *Adv. Funct. Mater.* 16 (2006) 17–26. doi:10.1002/adfm.200500616.

- [95] W.D. Marnier, A.S. Shaikh, S.J. Muller, J.D. Keasling, Morphology of artificial silica matrices formed via autsilification of a silaffin/protein polymer chimera., *Biomacromolecules*. 9 (2008) 1–5. doi:10.1021/bm701131x.
- [96] N. Kroger, Self-Assembly of Highly Phosphorylated Silaffins and Their Function in Biosilica Morphogenesis, *Science* (80-.). 298 (2002) 584–586. doi:10.1126/science.1076221.
- [97] S. Weiner, H.D. Wagner, THE MATERIAL BONE: Structure-Mechanical Function Relations, *Annu. Rev. Mater. Sci.* 28 (1998) 271–298. doi:10.1146/annurev.matsci.28.1.271.
- [98] T.T. Thula, D.E. Rodriguez, M.H. Lee, L. Pendi, J. Podschun, L.B. Gower, In vitro mineralization of dense collagen substrates: A biomimetic approach toward the development of bone-graft materials, *Acta Biomater.* 7 (2011) 3158–3169. doi:10.1016/j.actbio.2011.04.014.
- [99] B. Antebi, X. Cheng, J.N. Harris, L.B. Gower, X.-D. Chen, J. Ling, Biomimetic Collagen–Hydroxyapatite Composite Fabricated via a Novel Perfusion-Flow Mineralization Technique, *Tissue Eng. Part C Methods*. 19 (2013) 487–496. doi:10.1089/ten.tec.2012.0452.
- [100] D.R. Eyre, M.A. Weis, Bone Collagen: New Clues to Its Mineralization Mechanism from Recessive Osteogenesis Imperfecta, *Calcif. Tissue Int.* 93 (2013) 338–347. doi:10.1007/s00223-013-9723-9.
- [101] M.J. Glimcher, Mechanism of calcification: role of collagen fibrils and collagen-phosphoprotein complexes in vitro and in vivo., *Anat. Rec.* 224 (1989) 139–53. doi:10.1002/ar.1092240205.

- [102] B. Clarke, Normal bone anatomy and physiology., *Clin. J. Am. Soc. Nephrol.* 3 Suppl 3 (2008) S131-9. doi:10.2215/CJN.04151206.
- [103] K. Alvares, The role of acidic phosphoproteins in biomineralization, *Connect. Tissue Res.* 55 (2014) 34–40. doi:10.3109/03008207.2013.867336.
- [104] S. Weiner, Biomineralization: A structural perspective, *J. Struct. Biol.* 163 (2008) 229–234. doi:10.1016/j.jsb.2008.02.001.
- [105] H. Roach, Why does bone matrix contain non-collagenous proteins? The possible roles of osteocalcin, osteonectin, osteopontin and bone sialoprotein in bone mineralisation and resorption., *Cell Biol. Int.* 18 (1994) 617–628. doi:10.1006/cbir.1994.1088.
- [106] S. Weiner, W. Traub, Organization of hydroxyapatite crystals within collagen fibrils., *FEBS Lett.* 206 (1986) 262–6. <http://www.ncbi.nlm.nih.gov/pubmed/3019771>.
- [107] J.D. Hartgerink, Self-Assembly and Mineralization of Peptide-Amphiphile Nanofibers, *Science* (80-.). 294 (2001) 1684–1688. doi:10.1126/science.1063187.
- [108] S. Sudo, T. Fujikawa, T. Nagakura, T. Ohkubo, K. Sakaguchi, M. Tanaka, K. Nakashima, T. Takahashi, Structures of mollusc shell framework proteins, *Nature.* 387 (1997) 563–564. doi:10.1038/42391.
- [109] Y. Levi, S. Albeck, A. Brack, S. Weiner, L. Addadi, Control Over Aragonite Crystal Nucleation and Growth: An In Vitro Study of Biomineralization, *Chem. - A Eur. J.* 4 (1998) 389–396. doi:10.1002/(SICI)1521-3765(19980310)4:3<389::AID-CHEM389>3.0.CO;2-X.

- [110] L. Pereira-Mouriès, M.-J. Almeida, C. Ribeiro, J. Peduzzi, M. Barthélemy, C. Milet, E. Lopez, Soluble silk-like organic matrix in the nacreous layer of the bivalve *Pinctada maxima*, *Eur. J. Biochem.* 269 (2002) 4994–5003.
doi:10.1046/j.1432-1033.2002.03203.x.
- [111] G. Falini, S. Albeck, S. Weiner, L. Addadi, Control of Aragonite or Calcite Polymorphism by Mollusk Shell Macromolecules, *Science* (80-.). 271 (1996) 67–69. doi:10.1126/science.271.5245.67.
- [112] H. Miyatake-Onozabal, A.G.M. Barrett, A novel biomimetic synthesis of (S)-(-)-zearealenone: via macrocyclization and transannular aromatization, *Tetrahedron.* 66 (2010) 6331–6334. doi:10.1016/j.tet.2010.05.084.
- [113] A.J. Mieszawska, L.D. Nadkarni, C.C. Perry, D.L. Kaplan, Nanoscale control of silica particle formation via silk-silica fusion proteins for bone regeneration., *Chem. Mater.* 22 (2010) 5780–5785. doi:10.1021/cm101940u.
- [114] L.L.S. Canabady-Rochelle, D.J. Belton, O. Deschaume, H.A. Currie, D.L. Kaplan, C.C. Perry, Bioinspired silicification of silica-binding peptide-silk protein chimeras: comparison of chemically and genetically produced proteins., *Biomacromolecules.* 13 (2012) 683–90. doi:10.1021/bm201555c.
- [115] T.D. Sutherland, J.H. Young, S. Weisman, C.Y. Hayashi, D.J. Merritt, Insect silk: one name, many materials., *Annu. Rev. Entomol.* 55 (2010) 171–88.
doi:10.1146/annurev-ento-112408-085401.
- [116] F.G. Omenetto, D.L. Kaplan, A new route for silk, *Nat. Photonics.* 2 (2008) 641–643. doi:10.1038/nphoton.2008.207.

- [117] D.-H. Kim, J. Viventi, J.J. Amsden, J. Xiao, L. Vigeland, Y.-S. Kim, J.A. Blanco, B. Panilaitis, E.S. Frechette, D. Contreras, D.L. Kaplan, F.G. Omenetto, Y. Huang, K.-C. Hwang, M.R. Zakin, B. Litt, J.A. Rogers, Dissolvable films of silk fibroin for ultrathin conformal bio-integrated electronics, *Nat. Mater.* 9 (2010) 511–517. doi:10.1038/nmat2745.
- [118] C.-Z. Zhou, F. Confalonieri, N. Medina, Y. Zivanovic, C. Esnault, T. Yang, M. Jacquet, J. Janin, M. Duguet, R. Perasso, Z.-G. Li, Fine organization of *Bombyx mori* fibroin heavy chain gene, *Nucleic Acids Res.* 28 (2000) 2413–2419.
- [119] H. Yamada, H. Nakao, Y. Takasu, K. Tsubouchi, Preparation of undegraded native molecular fibroin solution from silkworm cocoons, *Mater. Sci. Eng. C.* 14 (2001) 41–46. doi:10.1016/S0928-4931(01)00207-7.
- [120] C.-Z. Zhou, F. Confalonieri, M. Jacquet, R. Perasso, Z.-G. Li, J. Janin, Silk fibroin: Structural implications of a remarkable amino acid sequence, *Proteins Struct. Funct. Genet.* 44 (2001) 119–122. doi:10.1002/prot.1078.
- [121] K. Yamaguchi, Y. Kikuchi, T. Takagi, A. Kikuchi, F. Oyama, K. Shimura, S. Mizuno, Primary structure of the silk fibroin light chain determined by cDNA sequencing and peptide analysis., *J. Mol. Biol.* 210 (1989) 127–39.
<http://www.ncbi.nlm.nih.gov/pubmed/2585514>.
- [122] K. Tanaka, S. Inoue, S. Mizuno, Hydrophobic interaction of P25, containing Asn-linked oligosaccharide chains, with the H-L complex of silk fibroin produced by *Bombyx mori*., *Insect Biochem. Mol. Biol.* 29 (1999) 269–76.
<http://www.ncbi.nlm.nih.gov/pubmed/10319440>.
- [123] C. Vepari, D.L. Kaplan, Silk as a biomaterial, *Prog. Polym. Sci.* 32 (2007) 991–

1007. doi:10.1016/j.progpolymsci.2007.05.013.

- [124] S.-W. Ha, H.S. Gracz, A.E. Tonelli, S.M. Hudson, Structural Study of Irregular Amino Acid Sequences in the Heavy Chain of *Bombyx mori* Silk Fibroin, *Biomacromolecules*. 6 (2005) 2563–2569. doi:10.1021/bm050294m.
- [125] T. Asakura, K. Suita, T. Kameda, S. Afonin, A.S. Ulrich, Structural role of tyrosine in *Bombyx mori* silk fibroin, studied by solid-state NMR and molecular mechanics on a model peptide prepared as silk I and II, *Magn. Reson. Chem.* 42 (2004) 258–266. doi:10.1002/mrc.1337.
- [126] T. Asakura, R. Sugino, J. Yao, H. Takashima, R. Kishore, Comparative structure analysis of tyrosine and valine residues in unprocessed silk fibroin (silk I) and in the processed silk fiber (silk II) from *Bombyx mori* using solid-state $(^{13}\text{C}, ^{15}\text{N}, \text{and } ^2\text{H})$ NMR., *Biochemistry*. 41 (2002) 4415–24.
<http://www.ncbi.nlm.nih.gov/pubmed/11914089>.
- [127] C. Wong Po Foo, S. V. Patwardhan, D.J. Belton, B. Kitchel, D. Anastasiades, J. Huang, R.R. Naik, C.C. Perry, D.L. Kaplan, Novel nanocomposites from spider silk-silica fusion (chimeric) proteins, *Proc. Natl. Acad. Sci.* 103 (2006) 9428–9433. doi:10.1073/pnas.0601096103.
- [128] R. Plowright, N. Dinjaski, S. Zhou, D.J. Belton, D.L. Kaplan, C.C. Perry, Influence of silk–silica fusion protein design on silica condensation in vitro and cellular calcification, *RSC Adv.* 6 (2016) 21776–21788.
doi:10.1039/C6RA03706B.
- [129] S.T. Krishnaji, W. Huang, O. Rabotyagova, E. Kharlampieva, I. Choi, V. V. Tsukruk, R. Naik, P. Cebe, D.L. Kaplan, Thin Film Assembly of Spider Silk-like

Block Copolymers, *Langmuir*. 27 (2011) 1000–1008. doi:10.1021/la102638j.

- [130] O.S. Rabotyagova, P. Cebe, D.L. Kaplan, Self-Assembly of Genetically Engineered Spider Silk Block Copolymers, *Biomacromolecules*. 10 (2009) 229–236. doi:10.1021/bm800930x.
- [131] N. Dinjaski, D. Ebrahimi, S. Ling, S. Shah, M.J. Buehler, D.L. Kaplan, Integrated Modeling and Experimental Approaches to Control Silica Modification of Design Silk-Based Biomaterials, *ACS Biomater. Sci. Eng.* (2016) acsbiomaterials.6b00236. doi:10.1021/acsbiomaterials.6b00236.
- [132] F.S. Emami, V. Puddu, R.J. Berry, V. Varshney, S. V. Patwardhan, C.C. Perry, H. Heinz, Prediction of Specific Biomolecule Adsorption on Silica Surfaces as a Function of pH and Particle Size, *Chem. Mater.* 26 (2014) 5725–5734. doi:10.1021/cm5026987.
- [133] S.T. Krishnaji, G. Bratzel, M.E. Kinahan, J.A. Kluge, C. Staii, J.Y. Wong, M.J. Buehler, D.L. Kaplan, Sequence-Structure-Property Relationships of Recombinant Spider Silk Proteins: Integration of Biopolymer Design, Processing, and Modeling, *Adv. Funct. Mater.* 23 (2013) 241–253. doi:10.1002/adfm.201200510.
- [134] D.J. Belton, A.J. Mieszawska, H.A. Currie, D.L. Kaplan, C.C. Perry, Silk–Silica Composites from Genetically Engineered Chimeric Proteins: Materials Properties Correlate with Silica Condensation Rate and Colloidal Stability of the Proteins in Aqueous Solution, *Langmuir*. 28 (2012) 4373–4381. doi:10.1021/la205084z.
- [135] S. Zhou, B. Varughese, B. Eichhorn, G. Jackson, K. McIlwrath, Pt-Cu Core-Shell and Alloy Nanoparticles for Heterogeneous NO_x Reduction: Anomalous Stability

and Reactivity of a Core-Shell Nanostructure, *Angew. Chemie.* 117 (2005) 4615–4619. doi:10.1002/ange.200500919.

- [136] A.J. Mieszawska, N. Furlong, I. Georgakoudi, N.M. Ouhib, D.J. Belton, C.C. Perry, D.L. Kaplan, Osteoinductive silk–silica composite biomaterials for bone regeneration, *Biomaterials.* 31 (2010) 8902–8910.
doi:10.1016/j.biomaterials.2010.07.109.
- [137] S. Gomes, I.B. Leonor, J.F. Mano, R.L. Reis, D.L. Kaplan, Natural and genetically engineered proteins for tissue engineering, *Prog. Polym. Sci.* 37 (2012) 1–17. doi:10.1016/j.progpolymsci.2011.07.003.
- [138] L.L.S. Canabady-Rochelle, D.J. Belton, O. Deschaume, H.A. Currie, D.L. Kaplan, C.C. Perry, Bioinspired Silicification of Silica-Binding Peptide-Silk Protein Chimeras: Comparison of Chemically and Genetically Produced Proteins, *Biomacromolecules.* 13 (2012) 683–690. doi:10.1021/bm201555c.
- [139] B.P. Partlow, C.W. Hanna, J. Rnjak-Kovacina, J.E. Moreau, M.B. Applegate, K.A. Burke, B. Marelli, A.N. Mitropoulos, F.G. Omenetto, D.L. Kaplan, Highly Tunable Elastomeric Silk Biomaterials, *Adv. Funct. Mater.* 24 (2014) 4615–4624. doi:10.1002/adfm.201400526.
- [140] L. Meinel, S. Hofmann, V. Karageorgiou, C. Kirker-Head, J. McCool, G. Gronowicz, L. Zichner, R. Langer, G. Vunjak-Novakovic, D.L. Kaplan, The inflammatory responses to silk films in vitro and in vivo, *Biomaterials.* 26 (2005) 147–155. doi:10.1016/j.biomaterials.2004.02.047.
- [141] G.H. Altman, F. Diaz, C. Jakuba, T. Calabro, R.L. Horan, J. Chen, H. Lu, J. Richmond, D.L. Kaplan, Silk-based biomaterials., *Biomaterials.* 24 (2003) 401–

16. <http://www.ncbi.nlm.nih.gov/pubmed/12423595> (accessed November 7, 2016).
- [142] Z. Izadifar, X. Chen, W. Kulyk, Strategic design and fabrication of engineered scaffolds for articular cartilage repair., *J. Funct. Biomater.* 3 (2012) 799–838. doi:10.3390/jfb3040799.
- [143] A. Di Luca, C. Van Blitterswijk, L. Moroni, The osteochondral interface as a gradient tissue: From development to the fabrication of gradient scaffolds for regenerative medicine, *Birth Defects Res. Part C Embryo Today Rev.* 105 (2015) 34–52. doi:10.1002/bdrc.21092.
- [144] X. Huang, X. Liu, S. Liu, A. Zhang, Q. Lu, D.L. Kaplan, H. Zhu, Biom mineralization regulation by nano-sized features in silk fibroin proteins: Synthesis of water-dispersible nano-hydroxyapatite, *J. Biomed. Mater. Res. Part B Appl. Biomater.* 102 (2014) 1720–1729. doi:10.1002/jbm.b.33157.
- [145] Z. Jiayao, Z. Guanshan, Z. Jinchi, C. Yuyin, Z. Yongqiang, Anthera ea pernyi silk sericin mediating biomimetic nucleation and growth of hydroxylapatite crystals promoting bone matrix formation, *Microsc. Res. Tech.* 80 (2017) 305–311. doi:10.1002/jemt.22793.
- [146] J. Ming, Z. Jiang, P. Wang, S. Bie, B. Zuo, Silk fibroin/sodium alginate fibrous hydrogels regulated hydroxyapatite crystal growth, *Mater. Sci. Eng. C.* 51 (2015) 287–293. doi:10.1016/j.msec.2015.03.014.
- [147] I. Gill, A. Ballesteros, Bioencapsulation within synthetic polymers (Part 1): sol-gel encapsulated biologicals., *Trends Biotechnol.* 18 (2000) 282–96. <http://www.ncbi.nlm.nih.gov/pubmed/10950510>.

- [148] I. Gill, A. Ballesteros, Encapsulation of Biologicals within Silicate, Siloxane, and Hybrid Sol–Gel Polymers: An Efficient and Generic Approach, *J. Am. Chem. Soc.* 120 (1998) 8587–8598. doi:10.1021/ja9814568.
- [149] A.C. Lawson, J.T. Czernuszka, Collagen-calcium phosphate composites, *Proc. Inst. Mech. Eng. Part H J. Eng. Med.* 212 (1998) 413–425. doi:10.1243/0954411981534187.
- [150] A.-W. Xu, Y. Ma, H. Cölfen, Biomimetic mineralization, *J. Mater. Chem.* 17 (2007) 415–449. doi:10.1039/B611918M.
- [151] H.R. Luckarift, J.C. Spain, R.R. Naik, M.O. Stone, Enzyme immobilization in a biomimetic silica support, *Nat. Biotechnol.* 22 (2004) 211–213. doi:10.1038/nbt931.
- [152] D.N. Rockwood, R.C. Preda, T. Yücel, X. Wang, M.L. Lovett, D.L. Kaplan, Materials fabrication from *Bombyx mori* silk fibroin., *Nat. Protoc.* 6 (2011) 1612–31. doi:10.1038/nprot.2011.379.
- [153] A. Krasko, B. Lorenz, R. Batel, H.C. Schröder, I.M. Müller, W.E. Müller, Expression of silicatein and collagen genes in the marine sponge *Suberites domuncula* is controlled by silicate and myotrophin., *Eur. J. Biochem.* 267 (2000) 4878–87. <http://www.ncbi.nlm.nih.gov/pubmed/10903523> (accessed November 7, 2016).
- [154] J.N. Cha, K. Shimizu, Y. Zhou, S.C. Christiansen, B.F. Chmelka, G.D. Stucky, D.E. Morse, Silicatein filaments and subunits from a marine sponge direct the polymerization of silica and silicones in vitro, *Proc. Natl. Acad. Sci.* 96 (1999) 361–365. doi:10.1073/pnas.96.2.361.

- [155] J.D.H. Strickland, *A Practical Handbook of Seawater Analysis*, 2nd ed., Fisheries Research Board of Canada, 1972.
- [156] X. Hu, D. Kaplan, P. Cebe, Determining Beta-Sheet Crystallinity in Fibrous Proteins by Thermal Analysis and Infrared Spectroscopy, *Macromolecules*. 39 (2006) 6161–6170. doi:10.1021/ma0610109.
- [157] W. Huang, S. Krishnaji, X. Hu, D. Kaplan, P. Cebe, Heat Capacity of Spider Silk-Like Block Copolymers, *Macromolecules*. 44 (2011) 5299–5309. doi:10.1021/ma200563t.
- [158] C. Jung, Insight into protein structure and protein-ligand recognition by Fourier transform infrared spectroscopy., *J. Mol. Recognit.* 13 (2000) 325–51. doi:10.1002/1099-1352(200011/12)13:6<325::AID-JMR507>3.0.CO;2-C.
- [159] M.R. DiSilvestro, J.-K.F. Suh, A cross-validation of the biphasic poroviscoelastic model of articular cartilage in unconfined compression, indentation, and confined compression, *J. Biomech.* 34 (2001) 519–525. doi:10.1016/S0021-9290(00)00224-4.
- [160] U.-J. Kim, J. Park, H. Joo Kim, M. Wada, D.L. Kaplan, Three-dimensional aqueous-derived biomaterial scaffolds from silk fibroin, *Biomaterials*. 26 (2005) 2775–2785. doi:10.1016/j.biomaterials.2004.07.044.
- [161] B.P. Partlow, C.W. Hanna, J. Rnjak-Kovacina, J.E. Moreau, M.B. Applegate, K.A. Burke, B. Marelli, A.N. Mitropoulos, F.G. Omenetto, D.L. Kaplan, Highly tunable elastomeric silk biomaterials., *Adv. Funct. Mater.* 24 (2014) 4615–4624. doi:10.1002/adfm.201400526.

- [162] L. Senior, M.P. Crump, C. Williams, P.J. Booth, S. Mann, A.W. Perriman, P. Curnow, Structure and function of the silicifying peptide R5, *J. Mater. Chem. B*. 3 (2015) 2607–2614. doi:10.1039/C4TB01679C.
- [163] S. Ling, Z. Qi, D.P. Knight, Z. Shao, X. Chen, Synchrotron FTIR Microspectroscopy of Single Natural Silk Fibers, *Biomacromolecules*. 12 (2011) 3344–3349. doi:10.1021/bm2006032.
- [164] C. Correia, S. Bhumiratana, L.-P. Yan, A.L. Oliveira, J.M. Gimble, D. Rockwood, D.L. Kaplan, R.A. Sousa, R.L. Reis, G. Vunjak-Novakovic, Development of silk-based scaffolds for tissue engineering of bone from human adipose-derived stem cells., *Acta Biomater*. 8 (2012) 2483–92. doi:10.1016/j.actbio.2012.03.019.
- [165] Y. Wang, D.D. Rudym, A. Walsh, L. Abrahamsen, H.-J. Kim, H.S. Kim, C. Kirker-Head, D.L. Kaplan, In vivo degradation of three-dimensional silk fibroin scaffolds, *Biomaterials*. 29 (2008) 3415–3428. doi:10.1016/j.biomaterials.2008.05.002.
- [166] Y. Wang, H.-J. Kim, G. Vunjak-Novakovic, D.L. Kaplan, Stem cell-based tissue engineering with silk biomaterials., *Biomaterials*. 27 (2006) 6064–82. doi:10.1016/j.biomaterials.2006.07.008.
- [167] C. Li, B. Hotz, S. Ling, J. Guo, D.S. Haas, B. Marelli, F. Omenetto, S.J. Lin, D.L. Kaplan, Regenerated silk materials for functionalized silk orthopedic devices by mimicking natural processing., *Biomaterials*. 110 (2016) 24–33. doi:10.1016/j.biomaterials.2016.09.014.
- [168] D. Sheehan, B. Hrapchak, Theory and practice of histotechnology, C. V. Mosby Co., St. Louis, MO, 1973.

- [169] S. Viguet-Carrin, P. Garnero, P.D. Delmas, The role of collagen in bone strength, *Osteoporos. Int.* 17 (2006) 319–336. doi:10.1007/s00198-005-2035-9.
- [170] H.J. Kim, U.-J. Kim, H.S. Kim, C. Li, M. Wada, G.G. Leisk, D.L. Kaplan, Bone tissue engineering with premineralized silk scaffolds, *Bone*. 42 (2008) 1226–1234. doi:10.1016/j.bone.2008.02.007.
- [171] J.B. Lian, G.S. Stein, Development of the osteoblast phenotype: molecular mechanisms mediating osteoblast growth and differentiation, *Iowa Orthop J.* 15 (1995) 118–140.
- [172] G.R. Beck, S.-W. Ha, C.E. Camalier, M. Yamaguchi, Y. Li, J.-K. Lee, M.N. Weitzmann, Bioactive silica-based nanoparticles stimulate bone-forming osteoblasts, suppress bone-resorbing osteoclasts, and enhance bone mineral density in vivo., *Nanomedicine*. 8 (2012) 793–803. doi:10.1016/j.nano.2011.11.003.
- [173] C. Ohtsuki, M. Kamitakahara, T. Miyazaki, Bioactive ceramic-based materials with designed reactivity for bone tissue regeneration., *J. R. Soc. Interface*. 6 Suppl 3 (2009) S349-60. doi:10.1098/rsif.2008.0419.focus.
- [174] R. Hill, An alternative view of the degradation of bioglass, *J. Mater. Sci. Lett.* 15 (1996) 1122–1125. doi:10.1007/BF00539955.
- [175] R. Plowright, N. Dinjaski, S. Zhou, D.J. Belton, D.L. Kaplan, C.C. Perry, Influence of silk–silica fusion protein design on silica condensation in vitro and cellular calcification, *RSC Adv.* 6 (2016) 21776–21788. doi:10.1039/C6RA03706B.

- [176] M. Santin, A. Motta, G. Freddi, M. Cannas, In vitro evaluation of the inflammatory potential of the silk fibroin., *J. Biomed. Mater. Res.* 46 (1999) 382–9. <http://www.ncbi.nlm.nih.gov/pubmed/10397996> (accessed November 7, 2016).
- [177] R. Elia, J. Guo, S. Budijono, V. Normand, D. Benczédi, F. Omenetto, D.L. Kaplan, Encapsulation of Volatile Compounds in Silk Microparticles., *J. Coatings Technol. Res.* 12 (2015) 793–799. doi:10.1007/s11998-015-9668-1.
- [178] L. Meinel, S. Hofmann, V. Karageorgiou, C. Kirker-Head, J. McCool, G. Gronowicz, L. Zichner, R. Langer, G. Vunjak-Novakovic, D.L. Kaplan, The inflammatory responses to silk films in vitro and in vivo., *Biomaterials.* 26 (2005) 147–55. doi:10.1016/j.biomaterials.2004.02.047.
- [179] B. Panilaitis, G.H. Altman, J. Chen, H.J. Jin, V. Karageorgiou, D.L. Kaplan, Macrophage responses to silk., *Biomaterials.* 24 (2003) 3079–85. <http://www.ncbi.nlm.nih.gov/pubmed/12895580> (accessed November 7, 2016).
- [180] C.C. Lechner, C.F.W. Becker, A sequence-function analysis of the silica precipitating silaffin R5 peptide, *J. Pept. Sci.* 20 (2014) 152–158. doi:10.1002/psc.2577.
- [181] T.M. O’Shea, X. Miao, Bilayered scaffolds for osteochondral tissue engineering., *Tissue Eng. Part B. Rev.* 14 (2008) 447–64. doi:10.1089/ten.teb.2008.0327.
- [182] M. Wiens, X. Wang, U. Schlossmacher, I. Lieberwirth, G. Glasser, H. Ushijima, H.C. Schröder, W.E.G. Müller, Osteogenic potential of biosilica on human osteoblast-like (SaOS-2) cells., *Calcif. Tissue Int.* 87 (2010) 513–24. doi:10.1007/s00223-010-9408-6.

- [183] C. Barragan-Adjemian, D. Nicolella, V. Dusevich, M.R. Dallas, J.D. Eick, L.F. Bonewald, Mechanism by which MLO-A5 late osteoblasts/early osteocytes mineralize in culture: similarities with mineralization of lamellar bone., *Calcif. Tissue Int.* 79 (2006) 340–53. doi:10.1007/s00223-006-0107-2.
- [184] W.J. Landis, An overview of vertebrate mineralization with emphasis on collagen-mineral interaction., *Gravit. Space Biol. Bull.* 12 (1999) 15–26.
<http://www.ncbi.nlm.nih.gov/pubmed/11541779> (accessed November 7, 2016).
- [185] P.S. Egli, E.B. Hunziker, R.K. Schenk, Quantitation of structural features characterizing weight- and less-weight-bearing regions in articular cartilage: a stereological analysis of medial femoral condyles in young adult rabbits., *Anat. Rec.* 222 (1988) 217–27. doi:10.1002/ar.1092220302.
- [186] A.C. Swann, B.B. Seedhom, The stiffness of normal articular cartilage and the predominant acting stress levels: implications for the aetiology of osteoarthritis., *Br. J. Rheumatol.* 32 (1993) 16–25.
<http://www.ncbi.nlm.nih.gov/pubmed/8422553> (accessed November 7, 2016).
- [187] M. Benjamin, E.J. Evans, L. Copp, The histology of tendon attachments to bone in man, *J. Anat.* 149 (1986) 89–100.
- [188] R.R. Cooper, S. Misol, Tendon and ligament insertion. A light and electron microscopic study., *J. Bone Joint Surg. Am.* 52 (1970) 1–20.
<http://www.ncbi.nlm.nih.gov/pubmed/4189231>.
- [189] H.H. Lu, S.D. Subramony, M.K. Boushell, X. Zhang, Tissue Engineering Strategies for the Regeneration of Orthopedic Interfaces, *Ann. Biomed. Eng.* 38 (2010) 2142–2154. doi:10.1007/s10439-010-0046-y.

- [190] K.L. Moffat, I.-N.E. Wang, S.A. Rodeo, H.H. Lu, Orthopedic Interface Tissue Engineering for the Biological Fixation of Soft Tissue Grafts, *Clin. Sports Med.* 28 (2009) 157–176. doi:10.1016/j.csm.2008.08.006.
- [191] G.H. Altman, R.L. Horan, H.H. Lu, J. Moreau, I. Martin, J.C. Richmond, D.L. Kaplan, Silk matrix for tissue engineered anterior cruciate ligaments, *Biomaterials.* 23 (2002) 4131–4141. doi:10.1016/S0142-9612(02)00156-4.
- [192] L.J. Gibson, M.F. Ashby, *Cellular Solids — Structure and Properties*, Cambridge University Press, Cambridge, 1997.
- [193] F. Rodríguez, D.D. Glawe, R.R. Naik, K.P. Hallinan, M.O. Stone, Study of the Chemical and Physical Influences upon in Vitro Peptide-Mediated Silica Formation, *Biomacromolecules.* 5 (2004) 261–265. doi:10.1021/bm034232c.
- [194] R.K. Iler, *The Chemistry of Silica: Solubility, Polymerization, Colloid and Surface Properties and Biochemistry of Silica*, 1979.
- [195] C.S. Chen, Geometric Control of Cell Life and Death, *Science* (80-.). 276 (1997) 1425–1428. doi:10.1126/science.276.5317.1425.
- [196] K. Kawaguchi, R. Kageyama, M. Sano, Topological defects control collective dynamics in neural progenitor cell cultures, *Nature.* 545 (2017) 327–331. doi:10.1038/nature22321.
- [197] S. V Murphy, A. Atala, 3D bioprinting of tissues and organs, *Nat. Biotechnol.* 32 (2014) 773–785. doi:10.1038/nbt.2958.
- [198] M. Singh, H.M. Haverinen, P. Dhagat, G.E. Jabbour, Inkjet Printing-Process and Its Applications, *Adv. Mater.* 22 (2010) 673–685. doi:10.1002/adma.200901141.

- [199] B. Derby, Bioprinting: inkjet printing proteins and hybrid cell-containing materials and structures, *J. Mater. Chem.* 18 (2008) 5717. doi:10.1039/b807560c.
- [200] H. Tao, B. Marelli, M. Yang, B. An, M.S. Onses, J.A. Rogers, D.L. Kaplan, F.G. Omenetto, Inkjet Printing of Regenerated Silk Fibroin: From Printable Forms to Printable Functions, *Adv. Mater.* 27 (2015) 4273–4279. doi:10.1002/adma.201501425.
- [201] S. Tasoglu, U. Demirci, Bioprinting for stem cell research, *Trends Biotechnol.* 31 (2013) 10–19. doi:10.1016/j.tibtech.2012.10.005.
- [202] S.-S. Yoo, S. Polio, 3D On-Demand Bioprinting for the Creation of Engineered Tissues, in: *Cell Organ Print.*, Springer Netherlands, Dordrecht, 2010: pp. 3–19. doi:10.1007/978-90-481-9145-1_1.
- [203] J. Guo, C. Li, S. Lin, W. Huang, Y. Chen, D.L. Kaplan, Multiscale design and synthesis of biomimetic gradient protein/biosilica composites for interfacial tissue engineering, *Biomaterials*. In review (2017).
- [204] E. Fonck, G.G. Feigl, J. Fasel, D. Sage, M. Unser, D.A. Rufenacht, N. Stergiopoulos, Effect of Aging on Elastin Functionality in Human Cerebral Arteries, *Stroke*. 40 (2009) 2552–2556. doi:10.1161/STROKEAHA.108.528091.
- [205] S. Ling, Z. Qi, Z. Shao, X. Chen, Determination of phase behaviour in all protein blend materials with multivariate FTIR imaging technique, *J. Mater. Chem. B* 3 (2015) 834–839. doi:10.1039/C4TB01808G.
- [206] S. Ling, Z. Qi, D.P. Knight, Z. Shao, X. Chen, FTIR imaging, a useful method for studying the compatibility of silk fibroin-based polymer blends, *Polym. Chem.* 4

(2013) 5401. doi:10.1039/c3py00508a.

- [207] S. Ling, Z. Qi, B. Watts, Z. Shao, X. Chen, Structural determination of protein-based polymer blends with a promising tool: combination of FTIR and STXM spectroscopic imaging, *Phys. Chem. Chem. Phys.* 16 (2014) 7741–7748. doi:10.1039/C4CP00556B.
- [208] J.R. Mauney, V. Volloch, D.L. Kaplan, Role of Adult Mesenchymal Stem Cells in Bone Tissue Engineering Applications: Current Status and Future Prospects, *Tissue Eng.* 11 (2005) 787–802. doi:10.1089/ten.2005.11.787.
- [209] R. Peng, X. Yao, B. Cao, J. Tang, J. Ding, The effect of culture conditions on the adipogenic and osteogenic inductions of mesenchymal stem cells on micropatterned surfaces, *Biomaterials.* 33 (2012) 6008–6019. doi:10.1016/j.biomaterials.2012.05.010.
- [210] M.F. Pittenger, A.M. Mackay, S.C. Beck, R.K. Jaiswal, R. Douglas, J.D. Mosca, M.A. Moorman, D.W. Simonetti, S. Craig, D.R. Marshak, Multilineage potential of adult human mesenchymal stem cells., *Science.* 284 (1999) 143–7. <http://www.ncbi.nlm.nih.gov/pubmed/10102814>.
- [211] D.J. Prockop, Marrow stromal cells as stem cells for nonhematopoietic tissues., *Science.* 276 (1997) 71–4. <http://www.ncbi.nlm.nih.gov/pubmed/9082988>.
- [212] Y. Jiang, B.N. Jahagirdar, R.L. Reinhardt, R.E. Schwartz, C.D. Keene, X.R. Ortiz-Gonzalez, M. Reyes, T. Lenvik, T. Lund, M. Blackstad, J. Du, S. Aldrich, A. Lisberg, W.C. Low, D.A. Largaespada, C.M. Verfaillie, Pluripotency of mesenchymal stem cells derived from adult marrow, *Nature.* 418 (2002) 41–49. doi:10.1038/nature00870.

- [213] T. Gong, J. Xie, J. Liao, T. Zhang, S. Lin, Y. Lin, Nanomaterials and bone regeneration, *Bone Res.* 3 (2015) 15029. doi:10.1038/boneres.2015.29.
- [214] H. Han, H. Ning, S. Liu, Q. Lu, Z. Fan, H. Lu, G. Lu, D.L. Kaplan, Silk Biomaterials with Vascularization Capacity, *Adv. Funct. Mater.* 26 (2016) 421–432. doi:10.1002/adfm.201504160.
- [215] A.J. Sophia Fox, A. Bedi, S.A. Rodeo, The Basic Science of Articular Cartilage: Structure, Composition, and Function, *Sport. Heal. A Multidiscip. Approach.* 1 (2009) 461–468. doi:10.1177/1941738109350438.
- [216] S. Liao, C.K. Chan, S. Ramakrishna, Stem cells and biomimetic materials strategies for tissue engineering, *Mater. Sci. Eng. C.* 28 (2008) 1189–1202. doi:10.1016/j.msec.2008.08.015.
- [217] J.A. Phillippi, E. Miller, L. Weiss, J. Huard, A. Waggoner, P. Campbell, Microenvironments Engineered by Inkjet Bioprinting Spatially Direct Adult Stem Cells Toward Muscle- and Bone-Like Subpopulations, *Stem Cells.* 26 (2008) 127–134. doi:10.1634/stemcells.2007-0520.
- [218] H.R. Luckarift, J.C. Spain, R.R. Naik, M.O. Stone, Enzyme immobilization in a biomimetic silica support, *Nat. Biotechnol.* 22 (2004) 211–213. doi:10.1038/nbt931.
- [219] S. ILKHANIZADEH, A. TEIXEIRA, O. HERMANSON, Inkjet printing of macromolecules on hydrogels to steer neural stem cell differentiation, *Biomaterials.* 28 (2007) 3936–3943. doi:10.1016/j.biomaterials.2007.05.018.
- [220] M.P. Lutolf, J.A. Hubbell, Synthetic biomaterials as instructive extracellular

- microenvironments for morphogenesis in tissue engineering, *Nat. Biotechnol.* 23 (2005) 47–55. doi:10.1038/nbt1055.
- [221] M.P. Lutolf, P.M. Gilbert, H.M. Blau, Designing materials to direct stem-cell fate, *Nature.* 462 (2009) 433–441. doi:10.1038/nature08602.
- [222] J.B. Recknor, D.S. Sakaguchi, S.K. Mallapragada, Directed growth and selective differentiation of neural progenitor cells on micropatterned polymer substrates, *Biomaterials.* 27 (2006) 4098–4108. doi:10.1016/j.biomaterials.2006.03.029.
- [223] C.J. Lee, P. Huie, T. Leng, M.C. Peterman, M.F. Marmor, M.S. Blumenkranz, S.F. Bent, H.A. Fishman, Microcontact printing on human tissue for retinal cell transplantation., *Arch. Ophthalmol. (Chicago, Ill. 1960).* 120 (2002) 1714–8. <http://www.ncbi.nlm.nih.gov/pubmed/12470147>.
- [224] R. Singhvi, A. Kumar, G.P. Lopez, G.N. Stephanopoulos, D.I. Wang, G.M. Whitesides, D.E. Ingber, Engineering cell shape and function., *Science.* 264 (1994) 696–8. <http://www.ncbi.nlm.nih.gov/pubmed/8171320>.
- [225] A.R. Armiento, M.J. Stoddart, M. Alini, D. Eglin, Biomaterials for articular cartilage tissue engineering: Learning from biology, *Acta Biomater.* 65 (2018) 1–20. doi:10.1016/j.actbio.2017.11.021.
- [226] S. Kwan Tat, J.-P. Pelletier, N. Amiable, C. Boileau, M. Lavigne, J. Martel-Pelletier, Treatment with ephrin B2 positively impacts the abnormal metabolism of human osteoarthritic chondrocytes, *Arthritis Res. Ther.* 11 (2009) R119. doi:10.1186/ar2782.
- [227] T.B.F. Woodfield, C.A. Van Blitterswijk, J. De Wijn, T.J. Sims, A.P. Hollander,

J. Riesle, Polymer Scaffolds Fabricated with Pore-Size Gradients as a Model for Studying the Zonal Organization within Tissue-Engineered Cartilage Constructs, *Tissue Eng.* 11 (2005) 1297–1311. doi:10.1089/ten.2005.11.1297.

[228] V.I. Sikavitsas, J.S. Temenoff, A.G. Mikos, Biomaterials and bone mechanotransduction., *Biomaterials.* 22 (2001) 2581–93.
<http://www.ncbi.nlm.nih.gov/pubmed/11519777>.

[229] A. Di Luca, A. Longoni, G. Criscenti, C. Mota, C. van Blitterswijk, L. Moroni, Toward mimicking the bone structure: design of novel hierarchical scaffolds with a tailored radial porosity gradient, *Biofabrication.* 8 (2016) 45007.
doi:10.1088/1758-5090/8/4/045007.